| | |
|---|---|
| **Titre:** Title: | Atomistic Control of Electronic and Magnetic Properties of Low-Dimensional Organic Materials |
| **Auteur:** Author: | Khalid Nowaz Anindya |
| **Date:** | 2024 |
| **Type:** | Mémoire ou thèse / Dissertation or Thesis |
| **Référence:** Citation: | Anindya, K. N. (2024). Atomistic Control of Electronic and Magnetic Properties of Low-Dimensional Organic Materials [Thèse de doctorat, Polytechnique Montréal]. PolyPublie. https://publications.polymtl.ca/59471/ |

**POLYTECHNIQUE MONTRÉAL**

affiliée à l'Université de Montréal

# Atomistic Control of Electronic and Magnetic Properties of Low-Dimensional Organic Materials

**KHALID NOWAZ ANINDYA**

Département de génie physique

Thèse présentée en vue de l'obtention du diplôme de *Philosophiæ Doctor*

Génie des matériaux

Octobre 2024

**POLYTECHNIQUE MONTRÉAL**

affiliée à l'Université de Montréal

Cette thèse intitulée :

**Atomistic Control of Electronic and Magnetic Properties of Low-Dimensional Organic Materials**

présentée par **Khalid Nowaz ANINDYA**

en vue de l'obtention du diplôme de *Philosophiæ Doctor*

a été dûment acceptée par le jury d'examen constitué de :

**David MÉNARD**, président

**Alain ROCHEFORT**, membre et directeur de recherche

**Julian SELF**, membre

**Olivier GRÖNING**, membre externe

# DEDICATION

*To all the kind-hearted souls whose unwavering support has been a source of strength and inspiration throughout this journey.*

# ACKNOWLEDGEMENTS

I would like to take this opportunity to express my deepest gratitude to **Prof. Alain Rochefort**, who has been far more than just a supervisor throughout this journey. His exceptional mentorship, constant encouragement, and unwavering belief in my abilities have been invaluable. Prof. Rochefort's profound knowledge and thoughtful guidance were not only a driving force behind my work but also a source of inspiration that pushed me to strive for excellence. His availability and readiness to assist, even at the busiest of times, whether through email or in person, greatly facilitated my progress and provided a sense of reassurance throughout my thesis work.

I would also like to extend my sincere appreciation to **Dr. Rémy Pawlak** and **Prof. Ernst Meyer** and their team from the University of Basel, Switzerland, whose invaluable experimental collaborations have enriched this research. Their expertise, insights, and willingness to collaborate have contributed to the success of this work. I am deeply grateful for their support and the opportunity to work alongside such talented researchers.

Finally, I extend my heartfelt appreciation to all those who have, in one way or another, inspired and supported me along this journey—loved ones, friends, and colleagues. Your presence and encouragement have meant more to me than words can express, and I am fortunate to have you by my side. Their belief in me has been an enduring source of strength, and for that, I am forever grateful.

# RÉSUMÉ

L'étude des matériaux organiques de basse dimension, en particulier ceux basés sur le graphène, offre d'excitantes perspectives pour progresser dans les domaines de l'électronique quantique, de la spintronique et de la supraconductivité. Contrairement aux systèmes inorganiques traditionnels, les matériaux organiques, y compris les aimants moléculaires et les structures à base de graphène, présentent des propriétés modulables qui peuvent être manipulées avec précision au niveau moléculaire. Cela en fait des candidats de choix pour le développement des technologies de nouvelle génération telles que les ordinateurs quantiques, les dispositifs spintroniques et les systèmes énergétiques à haute efficacité. Un thème important de cette thèse porte sur le potentiel des matériaux organiques magnétiques à surmonter les limitations de leurs homologues inorganiques. Ils offrent des avantages tels qu'une homogénéité magnétique accrue, une réduction de l'amortissement magnétique et la possibilité d'obtenir du ferromagnétisme avec uniquement des électrons de type s et p. Ces propriétés les rendent particulièrement adaptés à des applications dans des domaines où les aimants traditionnels sont moins efficaces, comme dans les dispositifs médicaux biocompatibles et l'électronique portable légère. De plus, la capacité d'atteindre le ferromagnétisme à température ambiante dans les matériaux organiques représente un jalon critique qui pourrait élargir considérablement leur applicabilité dans des dispositifs pratiques. Cependant, malgré ces attributs prometteurs, il reste des défis substantiels pour comprendre et réaliser un magnétisme robuste dans les systèmes organiques de basse dimension. Les preuves expérimentales actuelles suggèrent que le magnétisme dans les systèmes basés sur le graphène, incluant les nanorubans de graphène (GNRs), les nanoflocons de graphène et les polymères conjugués 2D, est souvent faible et principalement antiferromagnétique (AFeM). Pour la spintronique, il est crucial de réussir une transition des états de base AFeM vers des états ferromagnétiques (FeM), car les matériaux FeM possèdent le moment magnétique net nécessaire pour une détection de signal et un stockage de données efficaces. Cette thèse aborde ces défis en proposant des stratégies novatrices pour améliorer les propriétés magnétiques des GNRs et différents polymères conjugués 2D de type Kagome.

Les recherches présentées dans cette thèse emploient une combinaison d'approches théoriques et computationnelles, incluant la théorie de la fonctionnelle de la densité (DFT) et des calculs DFT+U, pour explorer comment l'ingénierie des défauts, le dopage et les modifications structurelles peuvent être utilisés pour ajuster les propriétés électroniques et magnétiques de ces matériaux. L'objectif

est de développer des matériaux spintroniques organiques robustes et modulables qui puissent fonctionner à température ambiante, les rendant ainsi viables pour des applications réelles dans l'électronique quantique et au-delà. Au Chapitre 4, l'accent est mis sur les GNRs unidimensionnels, en particulier les nanorubans de graphène de type armchair (AGNRs). Ici, l'introduction de défauts topologiques, tels que des défauts pentagonaux en bordure, montre qu'ils perturbent le réseau bipartite du graphène, conduisant à l'émergence d'états de spin très ordonnés. Ces spins localisés sont cruciaux pour stabiliser les phases ferromagnétiques, même en présence d'un substrat métallique, rendant ces matériaux plus adaptés aux applications spintroniques. Le Chapitre 5 prolonge cette exploration aux polymères 2D de type Kagome basés sur des monomères de triangulène. Grâce à un dopage stratégique avec des atomes de bore ou d'azote, nous démontrons comment ces polymères peuvent permutés d'un état antiferromagnétique à un état ferromagnétique. L'étude révèle que les polymères riches en bore présentent une haute mobilité des porteurs, les rendant idéaux pour des dispositifs logiques basés sur le spin, tandis que les polymères riches en azote montrent un comportement semi-métallique, avantageux pour des applications de stockage quantique. Au Chapitre 6, nous explorons les polymères 2D de type Kagome faits de monomères de nitrure de bore triangulaire (tBN) dopés au carbone. Nos travaux montrent que la substitution du carbone dans les monomères de tBN peut induire des états fondamentaux polarisés en spin et un ordre magnétique à longue portée, transformant ces matériaux traditionnellement isolants en semi-conducteurs où il y a coexistence de bandes de Dirac et de bandes plates près du niveau de Fermi. Ce chapitre examine également comment l'agencement des monomères dopés affecte les propriétés électroniques et magnétiques, fournissant des indices sur la manière dont ces matériaux peuvent être optimisés pour des applications spintroniques. Enfin, le Chapitre 7 explore le magnétisme dans les polymères Kagome à base d’hétérotriangulène, en se concentrant sur ceux fabriqués à partir de trioxoazatriangulène (TANGO). Le chapitre combine l'imagerie par microscopie à force atomique (AFM) et à effet tunnel (STM) à des calculs DFT+U pour explorer l'émergence d'états polarisés en spin et de moments magnétiques localisés en modifiant chimiquement les matériaux. Nos résultats montrent comment la concentration en défauts et le bris de symétrie influencent les propriétés magnétiques et électroniques, conduisant à une localisation accrue des bandes et à la perturbation des cônes de Dirac aux points K de la zone de Brillouin.

Cette thèse fait non seulement progresser la compréhension théorique des comportements magnétiques dans les matériaux organiques de basse dimension, mais elle comble également le

fossé entre la recherche théorique et les applications pratiques. En abordant des défis clés tels que l'obtention du ferromagnétisme à température ambiante et l'amélioration de la stabilité magnétique des systèmes à base de graphène, cette recherche pose les bases du développement de matériaux spintroniques organiques robustes et modulables.

# ABSTRACT

The study of low-dimensional organic materials, particularly those based on graphene, presents exciting opportunities for advancements in quantum electronics, spintronics, and superconductivity. Unlike traditional inorganic systems, these organic materials, including molecular magnets and graphene-based structures, exhibit tunable properties that can be precisely manipulated at the molecular level. This makes them prime candidates for developing next-generation technologies such as quantum computers, spintronic devices, and high-efficiency energy systems. A significant focus of this thesis is the potential of organic magnets to overcome the limitations of their inorganic counterparts. Organic magnets offer advantages such as increased magnetic homogeneity, reduced magnetic damping, and the ability to achieve ferromagnetism with only s and p electrons. These properties make them particularly suitable for applications in fields where traditional magnets are less effective, such as in biocompatible medical devices and lightweight, portable electronics. Furthermore, the ability to achieve room-temperature ferromagnetism in organic materials is a critical milestone that could dramatically expand their applicability in practical devices. However, despite these promising attributes, there remain substantial challenges in understanding and realizing robust magnetism in low-dimensional organic systems. Current experimental evidence suggests that magnetism in the graphene-based systems, which includes graphene nanoribbons (GNRs), graphene nanoflakes, and 2D conjugated polymers, is often weak and predominantly antiferromagnetic (AFeM). For spintronics, it is crucial to achieve a transition from AFeM to ferromagnetic (FeM) ground states, as FeM materials provide the net magnetic moment necessary for efficient signal detection and data storage. This thesis addresses these challenges by proposing novel strategies for enhancing the magnetic properties of GNRs, and different conjugated 2D Kagome polymers.

The research presented in this thesis employs a combination of theoretical and computational approaches, including density functional theory (DFT) and DFT+U calculations, to explore how defect engineering, doping, and structural modifications can be used to tune the electronic and magnetic properties of these materials. The goal is to develop robust, tunable organic spintronic materials that can operate at room temperature, thereby making them viable for real-world applications in quantum electronics and beyond. In Chapter 4, the focus is on one-dimensional GNRs, particularly armchair graphene nanoribbons (AGNRs). Here, the introduction of topological defects, such as pentagon edge defects, is shown to disrupt the graphene bipartite lattice, leading

to the emergence of highly ordered spin states. These localized spins are crucial for stabilizing ferromagnetic phases, even in the presence of a metallic substrate, making these materials more suitable for spintronic applications. Chapter 5 extends this exploration to two-dimensional Kagome polymers based on triangulene monomers. Through strategic doping with boron or nitrogen atoms, the chapter demonstrates how these polymers can be transitioned from an antiferromagnetic to a ferromagnetic state. The study reveals that boron-rich polymers exhibit high carrier mobilities, making them ideal for spin-based logic devices, while nitrogen-rich polymers show half-metallic behavior, advantageous for quantum storage applications. In Chapter 6, the thesis explores 2D Kagome polymers made of carbon-doped triangular boron nitride (tBN) monomers. The research shows that carbon substitution in tBN monomers can induce spin-polarized ground states and long-range magnetic order, transforming these traditionally insulating materials into semiconductors with coexisting Dirac and flat bands near the Fermi level. This chapter also examines how the arrangement of doped monomers affects the electronic and magnetic properties, providing insights into how these materials can be optimized for spintronic applications. Finally, Chapter 7 investigates magnetism in heterotriangulene-based Kagome polymers, focusing on those made from trioxoazatriangulene (TANGO) monomers. The chapter combines experimental atomic force microscopy (AFM) and scanning tunneling microscopy (STM) imaging with DFT+U calculations to explore the emergence of spin-polarized states and localized magnetic moments through chemical modification. The findings demonstrate how defect concentration and symmetry breaking impact the magnetic and electronic properties, leading to increased band localization and the disruption of Dirac cones at the K-points of the Brillouin Zone.

This thesis not only advances the theoretical understanding of magnetic behaviors in low-dimensional organic materials but also bridges the gap between theoretical research and practical applications. By addressing key challenges such as achieving room-temperature ferromagnetism and enhancing the magnetic stability of graphene-based systems, this research lays the groundwork for the development of robust, tunable organic spintronic materials.

# TABLE OF CONTENTS

# LIST OF TABLES

# LIST OF FIGURES

# LIST OF SYMBOLS AND ABBREVIATIONS

| | |
|---|---|
| 0D | Zero-dimensional |
| 1D | One-dimensional |
| 2D | Two-dimensional |
| 2D-KP | Two-Dimensional Kagome Polymer |
| AFM | Atomic Force Microscopy |
| AFeM | Antiferromagnetic |
| AGNR | Armchair Graphene Nanoribbon |
| BZ | Brillouin Zone |
| CB | Conduction Band |
| CBM | Conduction Band Minima |
| CC | Constant Current |
| CH | Constant Height |
| CNT | Carbon Nanotube |
| CTPA | Carbonyl-bridged Trioxoazatriangulene |
| CTPB | Carbonyl-bridged Triphenylborane |
| CtBN | Carbon-Doped Triangular Boron Nitride (Nitrogen Edges) |
| CtNB | Carbon-Doped Triangular Boron Nitride (Boron Edges) |
| DFT | Density Functional Theory |
| DFT+U | Density Functional Theory with Hubbard *U* Correction |
| DOS | Density of States |
| FeM | Ferromagnetic |
| GNR | Graphene Nanoribbon |
| HOMO | Highest Occupied Molecular Orbital |

| | |
|---|---|
| HT | Heterotriangulene |
| KL | Kagome Lattice |
| KP | Kagome Polymer |
| LDOS | Local Density of States |
| LHB | Lower Hubbard Band |
| LUMO | Lowest Unoccupied Molecular Orbital |
| MCNT | Magnetic Carbon Nanotube |
| MFH | Mean-field Hubbard |
| MNP | Magnetic Nanoparticle |
| MRI | Magnetic Resonance Imaging |
| MTPA | Methylene-bridged Triphenylamine |
| MTPB | Methylene-bridged Triphenylborane |
| OSS | On-surface Synthesis |
| OTPA | Oxygen-bridged Triphenylamine |
| OTPB | Oxygen-bridged Triphenylborane |
| P-(tBN-tNB) | Copolymer of tBN and tNB Monomers |
| $P^2$-tBN | Polymer of tBN Monomers (Nitrogen Edges) |
| $P^2$-tNB | Polymer of tBN Monomers (Boron Edges) |
| PAW | Projector-Augmented Wave |
| PBE | Perdew-Burke-Ernzerhof |
| PTM | Perchlorotriphenylmethyl |
| SOMO | Singly Occupied Molecular Orbital |
| SP-LDOS | Spin-polarized Local Density of States |
| STM | Scanning Tunneling Microscopy |

| | |
|---|---|
| STS | Scanning Tunneling Spectroscopy |
| SUMO | Singly Unoccupied Molecular Orbital |
| TAM | Triarylmethyl |
| TANGO | Trioxoazatriangulene |
| TB | Tight-binding |
| TOT | Trioxotriangulene |
| Tr | Triangulene |
| Tr-CC | Triangulene Polymer with Diacetylenic Linker |
| Tr3B | Boron-Rich Triangulene Polymer |
| Tr3B-CC | Boron-Rich Triangulene Polymer with Diacetylenic Linker |
| Tr3N | Nitrogen-Rich Triangulene Polymer |
| Tr3N-CC | Nitrogen-Rich Triangulene Polymer with Diacetylenic Linker |
| UC | Unit Cell |
| UE | Unpaired Electron |
| UHB | Upper Hubbard Band |
| VB | Valence Band |
| VBM | Valence Band Maxima |
| ZMB | Zero Bias Mode |
| ZMO | Zero-Mode Orbital |
| sGNR | Sawtooth Graphene Nanoribbon |
| tBN | Triangular Boron Nitride |

# LIST OF APPENDICES

# CHAPTER 1 INTRODUCTION

The exploration of low-dimensional organic materials, particularly in the context of magnetism and superconductivity, represents a significant step forward in materials science. These materials display unique quantum phenomena that are not observed in conventional systems and their reduced dimensionality enhances electron interactions and enables the emergence of exotic states like quantum spin liquids, topological superconductivity, and low-energy excitations. This area of research is not just a mere extension of existing knowledge; it is a leap into uncharted territories where the unique properties of organic materials are harnessed to revolutionize technological capabilities. The focus on low-dimensional systems, such as molecular magnets and graphene-based structures, opens up new possibilities for manipulating electronic and magnetic behaviors at a fundamental level.

Organic magnets have emerged as an alternative to their inorganic counterparts, offering a range of advantages that are reshaping the landscape of magnetic material applications. One of the key advantages of organic magnets is their increased magnetic homogeneity. Organic magnets are often composed of well-defined molecular units, allowing for more uniform magnetic interactions at the atomic level. In contrast, inorganic magnets tend to have crystal defects, grain boundaries, and structural inhomogeneities that can disrupt magnetic ordering. This homogeneity in organic magnets can result in more predictable and stable magnetic properties, which is critical for applications that require precise magnetic performance. Furthermore, they have sharp magnetization switching, which means they can change their magnetic state quickly and distinctly, a behavior comparable to inorganic materials. These properties make organic magnets suitable for a range of applications, especially in fields where the weight of the material is a critical factor, such as in mobile devices or space applications. The ability to achieve large coercivity — the ability of a magnetic material to withstand an external magnetic field without becoming demagnetized and high critical temperatures in these materials, as reported in recent research, indicates their potential for use in magnetoelectronic devices, magnetic sensors, and recording technologies [1]. Furthermore, organic magnets demonstrate exceptional light absorption capabilities, electric insulation, easy processability, biocompatibility, and tunability [2]. These attributes open up new practical opportunities, particularly in fields where traditional magnets fall short. For instance, their biocompatibility makes them ideal for medical applications, such as targeted drug delivery and

magnetic resonance imaging (MRI). Another notable advantage of organic-based magnets is their reduced magnetic damping and lower fabrication costs compared to traditional inorganic magnets [3]. This reduction in cost and complexity of production makes them more accessible for various technological applications, including consumer electronics and industrial processes. In addition, the chemical homogeneity of organic magnets is a significant advantage. They can achieve ferromagnetism in materials containing only s and p electrons, which opens up new avenues in the design of magnetic materials [4]. In brief, the development of organic magnets represents a significant advancement in materials science, offering a range of benefits over traditional inorganic magnets. Their versatility, tunability, and eco-friendly nature make them a promising material for future technological innovations and applications.

In the realm of quantum electronics, nanosized molecular magnetic materials such as single-molecule magnets and single-chain magnets are showing great promise for applications in quantum computations and memory devices [5]. Quantum electronics involves the use of quantum phenomena such as superposition and entanglement in electronic devices, stands to benefit immensely from these advancements. The potential use of nanomagnets in the construction of quantum computers, leveraging lower temperatures or quantum size effects [6], and the utilization of molecular nanomagnets in controlling decoherence and entanglement in quantum information technologies [7], point towards significant advancements in data storage, spintronics, and quantum computing [6, 8].

Superconductivity in low-dimensional organic materials, particularly in structures like twisted bilayer graphene, is another frontier being actively explored. The discovery of superconductivity in these materials has opened up new avenues for research, particularly in understanding the mechanisms that drive this phenomenon in organic systems. The implications of this research are profound, offering the potential for developing materials that conduct electricity with zero resistance at higher temperatures than traditional superconductors. A key factor in the superconducting properties of twisted bilayer graphene is the presence of flat bands, which lead to a high density of states at the Fermi level and are conducive to the formation of Cooper pairs and the onset of superconductivity. This could lead to a revolution in energy transmission and storage, significantly impacting various sectors, including renewable energy and transportation. However, achieving superconductivity in graphene requires extremely low temperatures, typically around 1.7

K, as evidenced by the lack of superconductivity at the relatively high temperature of 5 K (-268.15°C) during certain experiments [9-10].

Carbon-based organic and molecular magnets are emerging as alternatives to traditional d- and f-transition metal magnets. Their advantages include low-temperature processing, tunable physical properties, biodegradability, light weight, flexibility, and biocompatibility [11]. The synthesis of organic magnets exhibiting ferromagnetism above room temperature has rekindled interest in this field [11]. Furthermore, magnetic carbon nanotubes (MCNTs), composed of carbon nanotubes (CNTs) and magnetic nanoparticles (MNPs), are being recognized for their vast potential due to their superior physical and chemical properties [12], highlighting the role of carbon materials in the development of new organic magnetic materials [13-15].

This thesis aims to propose novel molecular concepts in organic magnetism. By manipulating electronic and magnetic properties at the molecular level, it is possible to design materials with specific functionalities tailored for next-generation technologies [16-17]. A key question driving this research is: How can magnetism in organic materials be maintained and enhanced? Understanding and optimizing this aspect is critical for realizing stable and robust organic magnetic systems. Equally important is the question: How can magnetic character be extended from lower dimensions (0D) to higher dimensions (2D) in all-organic systems to enable collective magnetism? Addressing this challenge is central to designing materials capable of supporting long-range magnetic ordering across multiple dimensions. Additionally, this thesis explores: What is the influence of a metallic substrate on the persistence of magnetic character? Investigating this factor provides crucial insights into the real-world applicability of these materials, particularly in device environments where substrate interactions play a significant role. Incorporating the latest advancements in the field, this research not only aims to deepen our understanding of these materials' fundamental properties but also strives to bridge the gap between theoretical research and practical applications. By addressing these questions, the exploration of low-dimensional organic materials is set to play a crucial role in shaping the future of technology and materials science. Leveraging the unique properties of organic magnets and carbon-based materials, this research is poised to contribute to the development of advanced materials with a wide range of applications in quantum electronics and beyond. To introduce magnetic materials, I will propose one-dimensional (1D) and two-dimensional (2D) organic carbon-based polymers designed to exhibit high spin states, potentially leveraging structures that enhance π-orbital overlap and

magnetic interactions. To probe these materials, I will analyze their spin-polarized electronic and magnetic properties from a theoretical point of view. Once the materials are characterized and their properties are understood, they can be possibly synthesized and integrated into devices.

# CHAPTER 2 LITERATURE REVIEW

## 2.1 Introduction to Graphene

Graphene, a single layer of carbon atoms tightly packed into a two-dimensional (2D) honeycomb lattice, has emerged as one of the most intriguing and extensively studied materials in the fields of physics, chemistry, materials science, and engineering. This fascination stems from graphene's unique set of properties, which include exceptional electrical conductivity, mechanical strength, thermal conductivity, and optical transparency. These characteristics not only make graphene a subject of fundamental scientific interest but also a promising material for a myriad of applications, ranging from electronics and energy storage to composite materials and biotechnology [18-19].

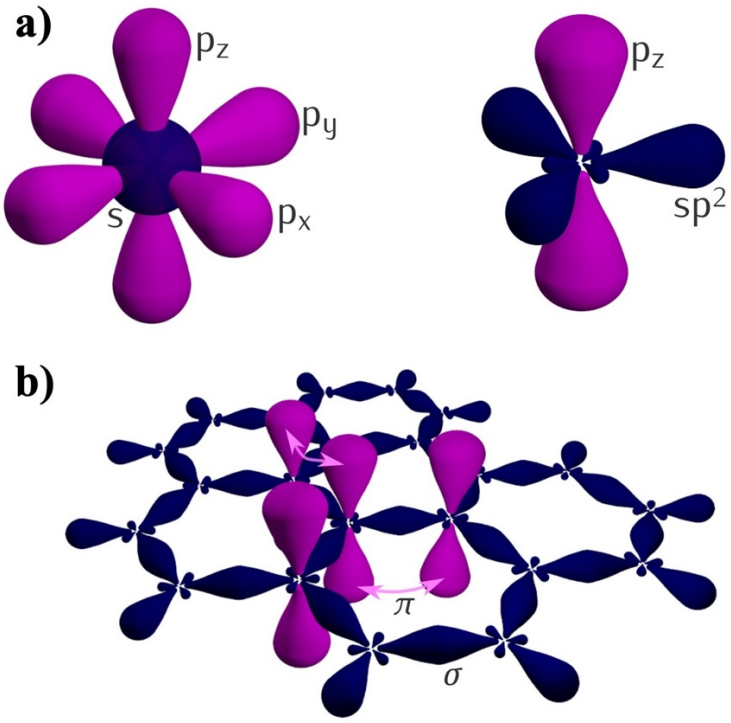


Figure 2.1 (a) Hybridization of carbon orbitals: formation of $sp^2$ hybrid orbitals with three lobes at 120° and out-of-plane $p_z$ orbital in graphene. (b) σ and π bonds in graphene: σ bonds from $sp^2$ hybrid orbital overlap and π bonds from $p_z$ orbital tunneling. Reproduced from [https://en.wikipedia.org/wiki/Graphene] with Creative Commons Attribution-Share Alike 4.0 International License.

Graphene was first isolated in 2004 by Andre Geim and Konstantin Novoselov at the University of Manchester, a breakthrough that earned them the Nobel Prize in Physics in 2010 [20]. The material's structure, resembling a honeycomb, gives rise to its extraordinary properties. Each

carbon atom in graphene is $sp^2$ hybridized, forming three σ-bonds with neighboring carbon atoms and one π-bond that extends out of the plane (see Figure 2.1). This configuration allows for the delocalization of π-electrons, which are free to move across the surface of the material, contributing to graphene's high electrical conductivity [21]. Graphene's two-dimensional structure is not just a simple, uniform array of carbon atoms; it features a complex atomic arrangement known as the A and B sublattice as shown in Figure 2.2. This dual sublattice system is intrinsic to the honeycomb lattice of graphene, where the hexagonal arrangement can be thought of as two interpenetrating triangular lattices. Each carbon atom in one sublattice (say A) is surrounded by three nearest neighbors from the other sublattice (B), and vice versa. This A-B sublattice configuration is fundamental to understanding many of graphene's electronic properties.

Graphene's band structure is a fundamental aspect that contributes to its intrinsic non-magnetic nature. It features a unique linear dispersion creating the so-called Dirac cones as shown in Figure 2.3. This zero-gap semiconductor characteristic allows electrons to behave as massless Dirac fermions, contributing to graphene's high electrical and thermal conductivity. The symmetry within the graphene lattice results in all π-electrons being paired, with their spins canceling each other out, thus contributing to its diamagnetic behavior and the absence of intrinsic magnetism [19, 22-23]. The presence of two distinct but interrelated sublattices leads to the emergence of Dirac cones in the electronic band structure of graphene at the K and K' points of the Brillouin zone (see Figure 2.3b). These points are where the conduction and valence bands meet, and electrons behave as if they are massless, traveling at the speed of light within the material. This remarkable electronic structure of graphene is characterized by its π and π* bands arising from the overlap of $p_z$ orbitals of two sub-lattices. The delocalized nature of the π-electrons across the graphene sheet enables high conductivity and the ability to sustain high current densities, a property highly valued in electronic applications [24].

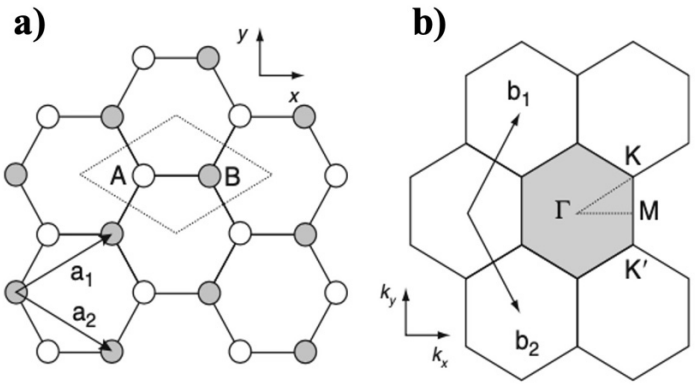


Figure 2.2 (a) Graphene lattice structure: illustration of carbon atoms in the honeycomb arrangement with lattice vectors $a_1$ and $a_2$ indicating unit cell dimensions. (b) Graphene's reciprocal lattice: representation of high symmetry points Γ, K, K', and M highlighting the Brillouin zone and corresponding reciprocal lattice vectors $b_1$ and $b_2$.

## 2.2 Why Graphene is Non-Magnetic?

Graphene's non-magnetic nature is intricately linked to its band structure and electronic configuration. The band structure of graphene reveals that it is a zero-gap semiconductor, where the conduction band and valence band meet at the Dirac points. At these points, the density of states vanishes, which is a peculiar characteristic arising from graphene's two-dimensional structure and the hexagonal arrangement of carbon atoms. This configuration results in a unique electronic structure where electrons can move through the graphene sheet with little to no resistance, behaving as massless Dirac fermions [22]. The presence of paired electrons in graphene gives stable electronic configuration that underlies its non-magnetic nature. For magnetism to arise in a material, unpaired electrons must be present, whose spins can align in the presence of an external magnetic field, giving rise to a net magnetic moment. In graphene, however, the delocalized π-electrons are all paired up, and their opposite spins negate any potential magnetic moment, rendering the material non-magnetic similar to most organic materials [24].

From a theoretical standpoint, graphene's non-magnetic nature and unique band structure provide a fascinating platform for exploring new physics in two-dimensional materials. The behavior of electrons in graphene, particularly their high mobility and the presence of Dirac cones in its band structure, challenges traditional semiconductor physics and opens up new theoretical models for understanding electron dynamics in two-dimensional systems [18, 25].

Practically, the non-magnetic nature of graphene does not diminish its utility; rather, it has motivated the exploration of methods to induce magnetism artificially. This pursuit has led to innovative approaches such as the creation of vacancies, doping with magnetic atoms, and engineering edge states in graphene nanostructures. These methods aim to disrupt the balance of the electron pairing in graphene, introducing unpaired electrons that can contribute to magnetic properties [26-27]. Graphene's non-magnetic nature is a fundamental aspect of its electronic structure; while this characteristic might seem to limit the material's applications in areas requiring magnetism, it has instead motivated creative scientific efforts to manipulate graphene's structure and composition to induce magnetic properties. As research in this area continues, the potential to integrate graphene into magnetic and spintronic devices becomes increasingly promising, highlighting the material's versatility and the innovative approaches to material science it inspires.

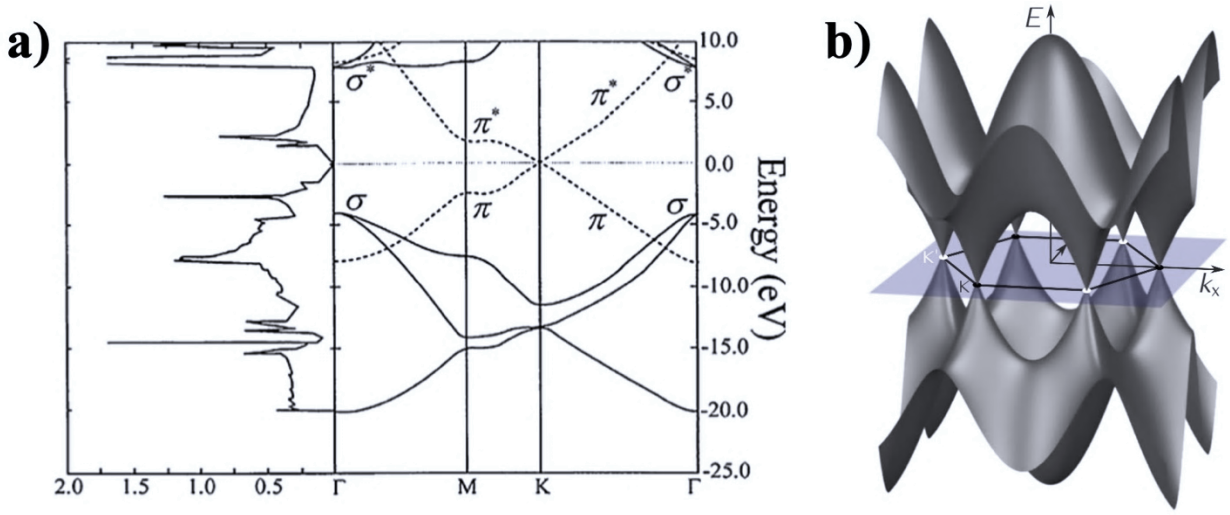


Figure 2.3 (a) Electronic band structure of graphene: energy dispersion relations along high symmetry directions Γ, M, K showing σ and π bands, with corresponding density of states (DOS) on the left. (b) 3D representation of graphene's band structure: visualization of the conical bands near the Dirac points K and K' in reciprocal space. Reproduced from [https://en.wikipedia.org/wiki/Graphene] with Creative Commons Attribution-Share Alike 4.0 International License.

## 2.3 Introducing Magnetism in Graphene

Understanding and manipulating the magnetic properties of graphene have significant implications for the development of spintronic devices, which utilize the spin of electrons for information processing. The ability to control the magnetic properties of graphene through external means such

as doping or structural modification opens up possibilities for graphene-based spintronic applications, offering an alternative to traditional electronics that rely solely on electron charge [28-29]. The exploration of magnetism in graphene also has practical implications for quantum computing and magnetic storage devices. By inducing and controlling magnetic properties in graphene, researchers can develop more efficient, faster, and smaller devices that leverage both the charge and spin of electrons, potentially revolutionizing the field of electronics and information technology [30-31].

Magnetism in materials arises from the alignment of electron spins. In graphene, when the delocalized π-electrons are disrupted, unpaired electrons with free spins can give rise to magnetic properties. The introduction of defects, impurities, or edge states in graphene can result in unpaired electrons. These electrons, with their associated spins, can align under certain conditions to produce a net magnetic moment, thus inducing magnetism in graphene. Recent theoretical studies and experimental observations have demonstrated that graphene can exhibit magnetic properties under specific conditions. These include the presence of vacancies [32], adatoms [33], or structural distortions [34] that break the symmetry of the graphene lattice and result in unpaired electrons. However, achieving ordered and stable magnetism in systems related to graphene continues to be a considerable challenge. To understand a highly ordered and stable magnetic moment into a two-dimensional (2D) graphene system, we first need to address the magnetic properties of 0D graphene nanoflakes, followed by those of 1D graphene nanoribbons. In the following section, we provide a concise overview of various methods for incorporating all-organic magnetism into different graphene-like systems starting with 0D upto 2D polymer.

### 2.3.1 Magnetism in 0D Nanoflake

The magnetic nature in graphene nanostructures or nanographenes (NGs), can vary based on the shape and orientation of their edges. There are mainly two ways to induce magnetism in nanographene: through (i) sub-lattice mismatch and (ii) topological frustration, with Clar's goblet serving as a prime example of the latter. Furthermore, organic adatoms can also significantly contribute to induce magnetism in graphene nanoflakes.

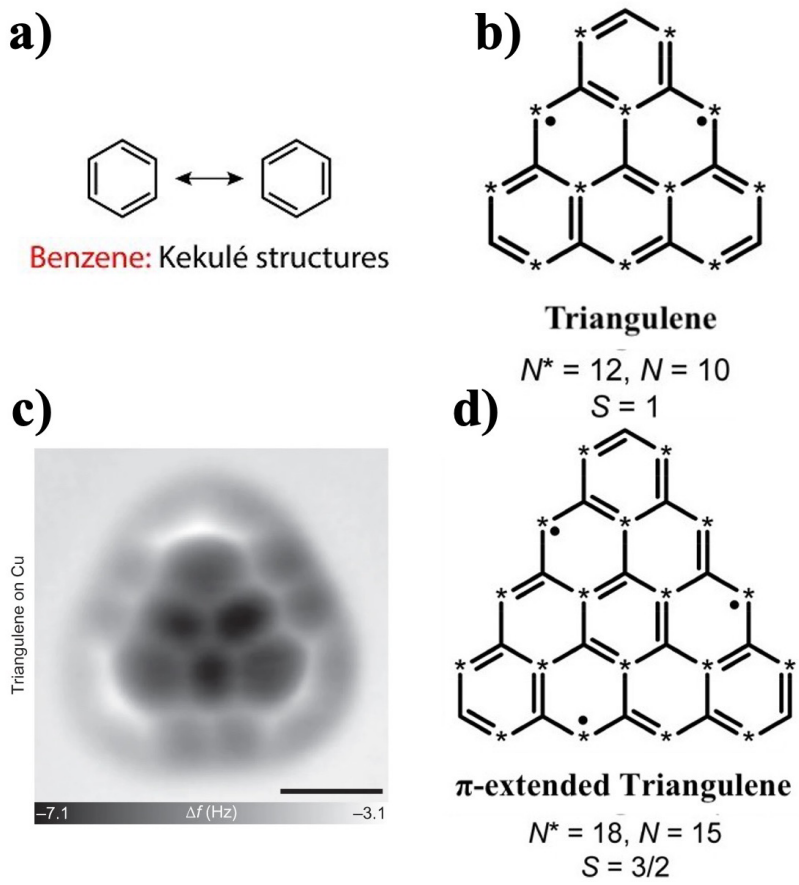


Figure 2.4 (a) Benzene Kekulé structures: depiction of resonance forms. (b) Molecular structure of triangulene: configuration with $N^*$=12 atoms in one sublattice and $N$=10 atoms in the other sublattice; with spin, $S$=1. (c) AFM image of triangulene on copper surface: visualization of molecular geometry. (d) π-extended triangulene: extended structure with different sublattices $N^*$=18 and $N$=15, $S$=3/2. Reproduced from [35,36] with permission from Springer Nature and American Chemical Society, respectively.

**(i) Sub-lattice Mismatch:**

This approach to inducing magnetism in nanographene involves creating an imbalance in the bipartite graphene lattice, which translates to a spin imbalance as per Lieb's theorem. According to Lieb's theorem, for certain types of lattice structures made up of two interpenetrating sublattices (often referred to as bipartite lattices), the number of magnetic moments (spins) in the ground state of the system is directly related to the difference in the number of sites between the two sublattices. Specifically, in the context of the Hubbard model, which is a simplified model for electrons in a lattice, Lieb's theorem predicts that the total spin $S$ of the ground state is given by: $S = \frac{1}{2}(N_A - N_B)$,

where $N_A$ and $N_B$ represent the number of sites in sublattices A and B, respectively. For example, in the triangulene structure shown in Figure 2.4b:

$N^* = 12$ (number of sites on sublattice A)

$N = 10$ (number of sites on sublattice B)

The difference $N^* - N = 12 - 10 = 2$, leading to a total spin $S = \frac{1}{2} \times 2 = 1$, as indicated in Figure 2.4b. This imbalance in the bipartite graphene lattice can be achieved through the creation of atomic defects that remove a $p_z$ orbital or in NGs with specific shapes where sublattice imbalance is structurally inherent. Such NGs, referred to as sublattice-imbalanced NGs, inherently lack a classical Kekulé structure (alternating single and double bonds, as shown in Figure 2.4a) without leaving unpaired electrons. Experimentally, the presence of spin-split states in these systems has been detected in scanning tunneling microscopy (STM) and scanning tunneling spectroscopy (STS) measurements [35-38, 40].

In a groundbreaking study, researchers have synthesized and characterized triangulene, a molecule renowned for its elusive magnetic properties and triplet ground state [35]. Triangulene is composed of six fused benzene rings, totaling 22 carbon atoms (see Figure 2.4b). Unlike typical molecules with an even number of carbons, triangulene cannot be described by conventional Kekulé-style resonant structures due to sub-lattice mismatch with two unpaired valence electrons as shown in Figure 2.4b, making it highly reactive and challenging to synthesize in its unsubstituted form. The team overcame this challenge through an innovative on-surface generation technique, employing the tip of a combined scanning tunneling and atomic force microscope (STM/AFM) to dehydrogenate precursor molecules, successfully synthesizing unsubstituted triangulene while preserving its free-molecule properties. AFM measurements revealed triangulene's planar, threefold symmetric structure (see Figure 2.4c), highlighting its unique non-Kekulé topology. This topology results in open-shell π-conjugated graphene fragments, which are responsible for the molecule's high-spin ground states. Such properties make triangulene a promising material for future organic spintronic devices. The study's combination of STM/AFM characterization and spin-polarized density functional theory (DFT) calculations not only confirmed triangulene's ferromagnetic triplet ground state but also provided valuable insights into its electronic structure. This research has marked a significant advance in the understanding of triangulene's magnetic properties and opened new avenues for the exploration of organic electronics and spintronics.

In another groundbreaking study on π-extended triangulene with 3 unpaired electrons (see Figure 2.4d) [36], the authors elucidate the molecule's unique electronic and magnetic properties through a combination of theoretical models and experimental techniques, as comprehensively depicted in Figure 2.5. This figure is pivotal in demonstrating the molecule's high-spin ground state and open-shell character. The use of nearest-neighbor tight-binding (TB) model reveals three nonbonding, half-filled zero-energy states, indicating an open-shell structure (see Figure 2.5a). A mean-field Hubbard (MFH) model further refines this understanding by introducing electron-electron interactions. The MFH model leads to spin polarization and to the opening of a Coulomb gap, which signifies the molecule's magnetic interactions (see Figure 2.5b). In the case of the triangulene or other related high-spin graphene based systems, the Coulomb gap can be understood as the energy gap arising from strong on-site Coulomb repulsion in the system's localized electronic states. This gap is conceptually similar to the Hubbard-split states, which emerge from strong electron-electron interactions in a lattice and are crucial for understanding the behavior of electrons in correlated materials. The Hubbard model, which provides the theoretical foundation for these states, predicts a splitting of energy levels into two distinct bands—the Lower Hubbard Band (LHB) and the Upper Hubbard Band (UHB)—due to the repulsive energy cost associated with electrons occupying the same site. Due to the inherent sublattice imbalance and the resulting unpaired spins in these structures, electron-electron interactions create a gap between occupied and unoccupied states. In these systems, the Coulomb gap represents the energy required to overcome the repulsion and add or remove an electron, leading to the spin-polarized states observed experimentally.

Using the MFH model, the Hubbard splitting results in three quasi-degenerate states for both the singly occupied molecular orbitals (SOMOs) and singly unoccupied molecular orbitals (SUMOs) (see Figure 2.5b). These correspond to the three zero-energy states predicted by the TB model in Figure 2.5a, indicating how the electron-electron interactions in the system lift the degeneracy of these midgap states. The energy level scheme of the spin-polarized frontier orbitals, shown in Figure 2.5c, showcases the three quasi-degenerate SOMOs with parallel spin alignment, contributing to an open-shell quartet ground state. This alignment is visualized through computed wave functions of the SOMOs, highlighting an edge-localized character predominantly on one sublattice, which underscores the molecule's magnetic properties (see Figure 2.5d). The computed spin density distribution plotted in Figure 2.5e further supports these findings, showing spin

localization at the zigzag carbon atoms of one sublattice, indicative of the molecule's magnetic anisotropy. Scanning tunneling spectroscopy (STS) experiments and simulated tunneling local density of states (TB-LDOS) maps corroborate the theoretical predictions, revealing pronounced peaks in the density of states (see Figure 2.5f) corresponding to the spin-split frontier orbitals. Distinct peaks in the DOS detected at −400 mV and +1.15 V (refer to Figure 2.5f) correspond to the negative ion resonance (NIR) and positive ion resonance (PIR), respectively. NIR appears when the energy of the tunneling electron matches the unoccupied states associated with the UHB, indicating resonant electron addition. PIR corresponds to peaks related to the occupied states in the LHB, reflecting resonant electron removal. These resonances are directly linked to the Coulomb gap and highlight the system's localized spin states in the *dI/dV* spectroscopy. Spatial mapping of the *dI/dV* signal at these bias voltages (Figure 2.5g) demonstrates a strong correlation with the TB-LDOS maps. Specifically, the maps show the singly occupied and unoccupied molecular orbitals (SOMO and SUMO) at −400 mV and +1.15 V, respectively. These results not only validate the theoretical predictions but also highlight π-extended triangulene's remarkable electronic and magnetic properties with precise experimental validations.

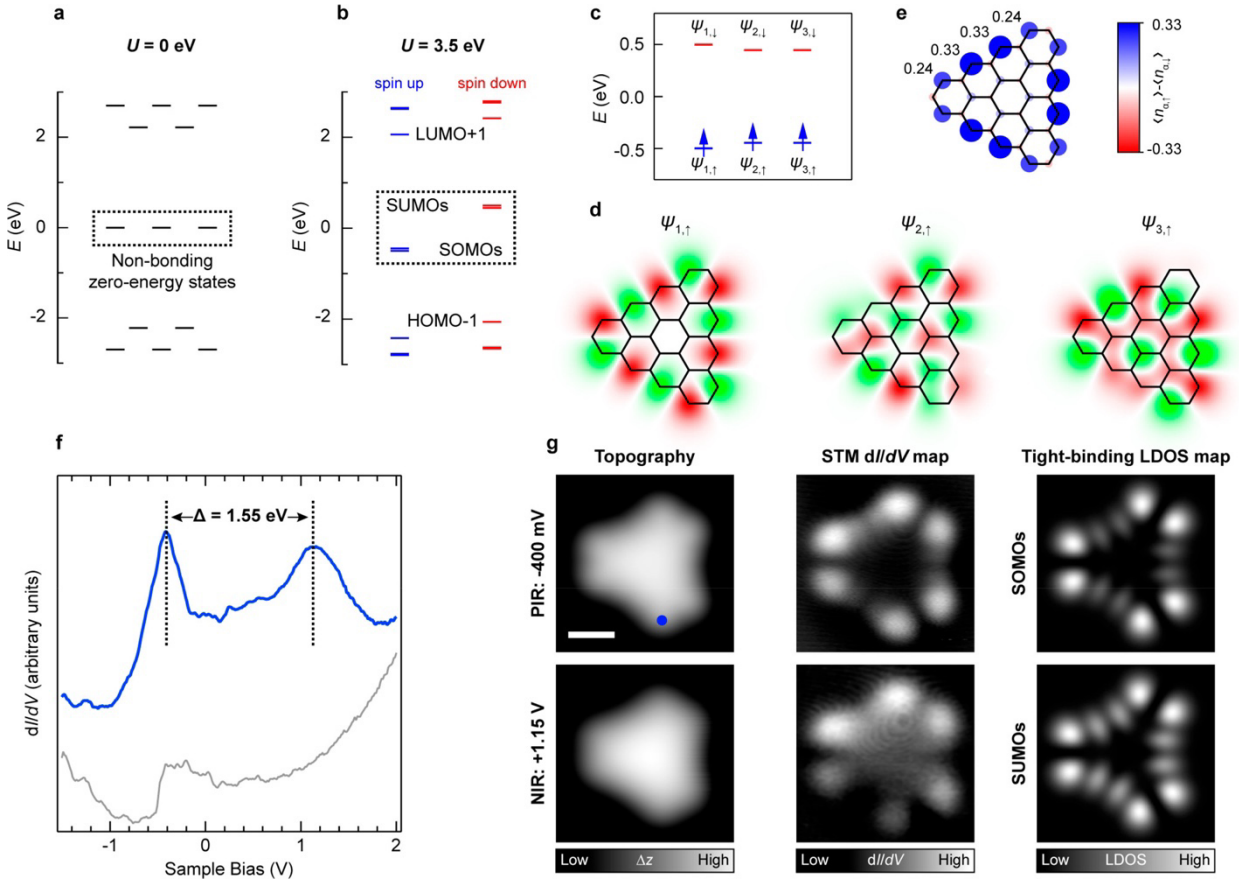


Figure 2.5 (a) Nearest-neighbor TB model of π-extended triangulene: energy spectrum showing three nonbonding zero-energy states. (b) MFH energy spectrum: gap opening due to spin polarization, with on-site Coulomb repulsion ($U$). (c) Energy level scheme: spin-polarized frontier orbitals $\psi_1$, $\psi_2$, and $\psi_3$. (d) Computed wave functions of SOMOs: green/red isosurfaces indicating opposite phases. (e) Computed spin density distribution: blue/red isosurfaces denoting spin up/spin down density, numbers indicating spin density values. (f) *dI/dV* spectrum on π-extended triangulene: blue curve at position marked in panel (g), gray curve as reference spectrum on Au(111); spectra offset for clarity. (g) Constant-current STM images (left panels) and spatial mapping of *dI/dV* signals (center panels), with simulated TB-LDOS maps of SOMOs and SUMOs (right panels); tunneling parameters: $V$=−400 mV, $I$=400 pA (PIR) and $V$=+1.15 V, $I$=420 pA (NIR); $V_{rms}$=22 mV; scale bar: 0.5 nm. Reproduced from [36] with permission from American Chemical Society.

In the exploration of molecular magnetism in NGs, the study of triangulene dimers presents a significant advancement, offering insights into the magnetic properties and coupling mechanisms between molecular species. This recent study's findings not only underscore the tunability of magnetic coupling in these novel structures but also pave the way for future research in the development of high-spin networks [37]. The study employs a combination of bond-resolved STM,

STS, and inelastic electron tunneling spectroscopy (IETS) to investigate the magnetic properties of triangulene dimers.

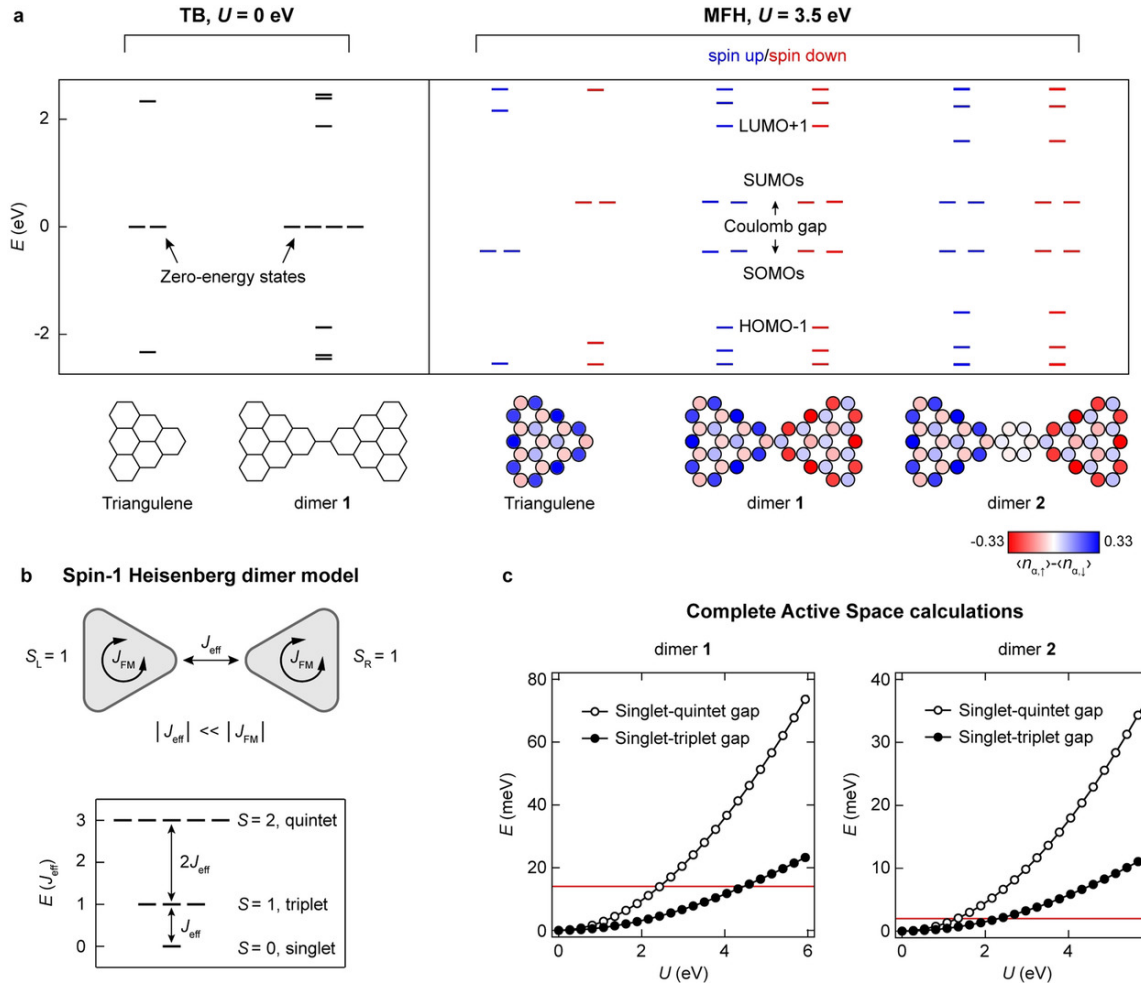


Figure 2.6 (a) Theoretical electronic and magnetic characterization: nearest-neighbor TB energy spectra of triangulene and its dimer (left), and MFH energy spectra of triangulene, dimer 1, and dimer 2, including corresponding spin polarization plots (right). *U* represents on-site Coulomb repulsion. (b) Schematic depiction: spin-1 Heisenberg dimer model for dimers 1 and 2 (top), and energy level scheme from the analytical solution of the Heisenberg dimer model for antiferromagnetic coupling between triangulene units (bottom). $S_L/S_R$ denote the total spin quantum numbers of the left/right triangulene units. (c) Energy levels of open-shell triplet and quintet states: for dimers 1 and 2 relative to their open-shell singlet ground states, calculated using the CAS(6,6) approximation and plotted as a function of *U*. Red solid lines indicate the experimental singlet–triplet gaps of 14 meV and 2 meV for dimers 1 and 2, respectively. Reproduced from [37] with permission from John Wiley and Sons.

These techniques reveal collective singlet–triplet spin excitations within the dimers, indicative of efficient magnetic coupling between the triangulene units. The experimental findings are supported

by theoretical analyses, including tight-binding and Hubbard model calculations, which provide a deeper understanding of the electronic and magnetic structures of the dimers.

Figure 2.6 serves as a cornerstone for understanding the theoretical framework underpinning the magnetic properties of triangulene dimers. It presents the electronic and magnetic structures of triangulene and its dimers, employing both nearest-neighbor tight-binding (TB) models and MFH models calculations (see Figure 2.6a). The TB model highlights the presence of non-bonding zero-energy states (ZESs) in triangulene and its dimers, which are crucial for the magnetic characteristics of these structures. The Hubbard model further refines this understanding by predicting the open-shell singlet ground state and the excited triplet and quintet states, offering a quantum mechanical perspective on the magnetic interactions at play.

The figure intricately illustrates the energy spectra and spin polarization plots for triangulene and the dimers, showcasing the alignment of theoretical predictions with the observed magnetic behaviors. Figure 2.6b, sheds light on the intricate magnetic coupling mechanisms in triangulene dimers. The effective exchange interaction, $J_{eff}$, is a quantitative measure of the magnetic coupling strength between two or more spins in a system. A high value of $J_{eff}$ indicates strong magnetic interaction between spins. In the context of magnetic materials, particularly those based on carbon such as nanographene, strong exchange interactions can lead to pronounced magnetic properties, such as high magnetic ordering temperatures and significant magnetic moments. In the case of triangulene dimers, $J_{eff}$ encapsulates the interaction between the four unpaired electrons of the two triangulene units. The sign and magnitude of $J_{eff}$ are critical in determining the magnetic ground state of the dimer—whether it will be antiferromagnetic (AFeM) or ferromagnetic (FeM), and how strongly the spins are coupled. Figure 2.6b illustrates the calculated $J_{eff}$ values for the triangulene dimers, providing a visual representation of how the magnetic coupling varies depending on the structural configuration of the dimer (e.g., directly bonded vs. phenylene-spaced linkage). Each triangulene unit shows strong FeM coupling, but in the dimer, weak $J_{eff}$ values define AFeM coupling between the units. And the phenylene spacer in between the units further weakens the $J_{eff}$. In addition, the energy diagrams show the relative energies of the singlet, triplet, and possibly quintet states, which are influenced by the $J_{eff}$ value. A negative $J_{eff}$ would indicate AFeM coupling, leading to a lower energy for the singlet state, while a positive $J_{eff}$ would suggest FeM coupling, favoring the triplet state.

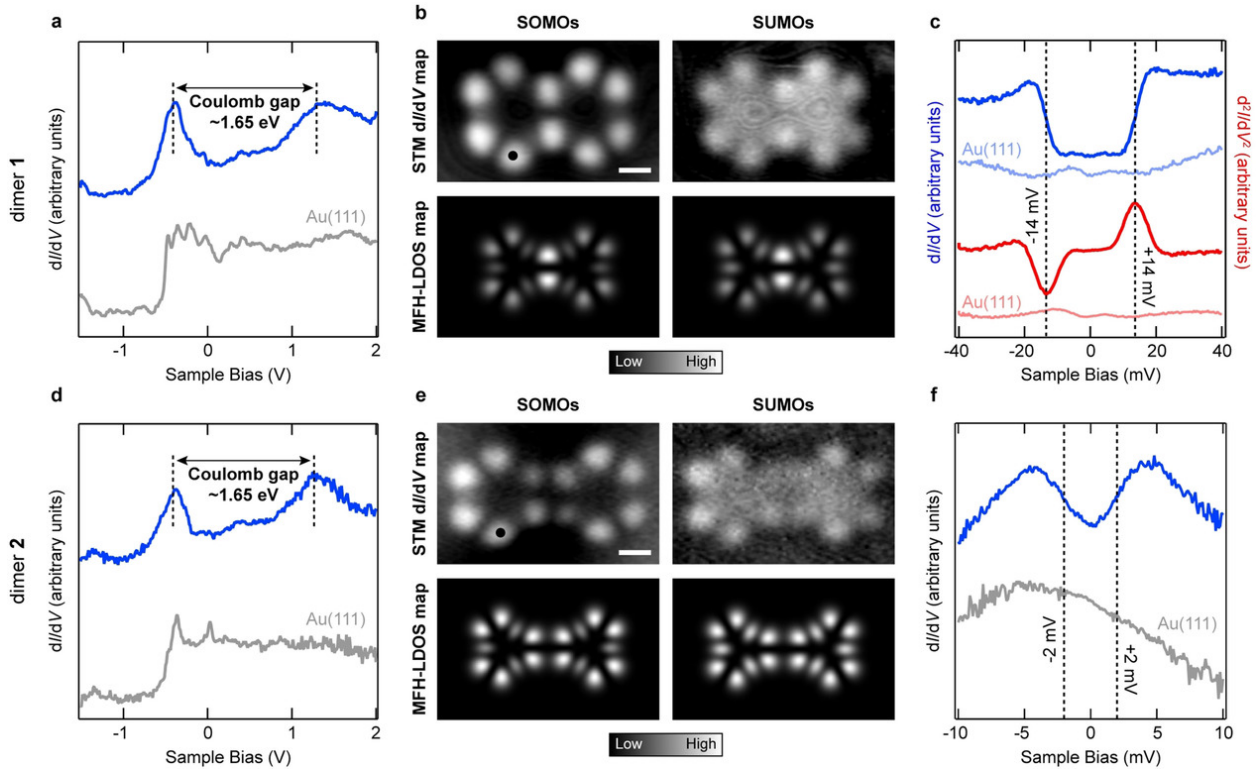


Figure 2.7 (a, d) Long-range *dI/dV* spectrum: blue curves for dimer 1 (a) and dimer 2 (d). (b, e) Experimental *dI/dV* maps (top) and MFH-LDOS maps (bottom): at SOMO and SUMO resonances for dimer 1 (b) and dimer 2 (e). Tunneling parameters: $V$ =−450 mV, $I$=350 pA (SOMOs, in b), $V$=+1.00 V, $I$=350 pA (SUMOs, in b); $V$=−400 mV, $I$=350 pA (SOMOs, in e) and $V$=+1.10 V, $I$=450 pA (SUMOs, in e); $V_{rms}$ = 22 mV. (c, f) *dI/dV* (blue curve) and IETS (red curve) spectra for dimer 1 (c), and *dI/dV* spectrum (blue curve) for dimer 2 (f) near Fermi energy. Acquisition positions marked by filled circles in panels (b) and (e). Scale bars: 0.5 nm. Reproduced from [37] with permission from John Wiley and Sons.

Figure 2.7 complements the theoretical insights from Figure 2.6 with more empirical evidence, showcasing scanning tunneling microscopy (STM) and scanning tunneling spectroscopy (STS) results that validate the predicted magnetic properties of triangulene dimers. This figure is pivotal in demonstrating the collective singlet–triplet spin excitations observed in the dimers, which are indicative of efficient magnetic coupling between the triangulene units. The STM images and STS data presented in Figure 2.7 not only confirm the structural integrity of the synthesized dimers but also provide unambiguous spectroscopic signatures of their magnetic ground states and excitations. STS measurements in Figure 2.7a and 2.7d shows the coulomb gap between spin-split singly occupied and unoccupied frontier orbitals SOMO and SUMO, respectively. While STM images in Figure 2.7b and 2.7e validates their theoretical LDOS maps of SOMO and SUMO. The differential conductance (*dI/dV*) spectroscopy performed on the triangulene dimers near the Fermi energy

showcases a pivotal experimental finding related to its magnetic properties. The spectroscopy revealed conductance steps symmetrically distributed around zero bias, with a notable increase in conductance by approximately 35% at these steps compared to the conductance at zero bias (see Figure 2.7c). This observation is a hallmark of inelastic excitation, suggesting the occurrence of a magnetic event within the molecule. Given the known magnetic states of dimer 1, specifically, its open-shell singlet ground state and the first excited open-shell triplet state—the inelastic excitations observed are attributed to singlet-to-triplet spin excitations. This aligns with the IETS spin selection rule, which permits changes in the spin state ($\Delta S$) of 0 or ±1 for magnetic excitations. From these experiments, the threshold for excitation was determined to be around 14 mV. This value, extracted from fitting the experimental IETS spectrum with a model of an antiferromagnetic spin-1 Heisenberg dimer, directly measures the effective exchange coupling ($J_{eff}$) value, or the singlet-to-triplet gap, for the dimer. This empirical derivation of the $J_{eff}$ value constitutes a significant experimental insight into the magnetic interactions within the triangulene dimer, offering a quantitative assessment of its magnetic excitation energy and reinforcing the theoretical predictions regarding its magnetic ground states. The experimental findings detailed in Figure 2.7 are instrumental in corroborating the theoretical predictions, offering a comprehensive view of the magnetic landscape of triangulene dimers. This synergy between theoretical and experimental approaches enriches our understanding of all-carbon magnetism and underscores the potential of triangulene dimers as building blocks for other magnetic graphene system.

**(ii) Topological Frustration:**

Topological frustration in nanographene, as exemplified by Clar's goblet ($C_{38}H_{18}$) (see Figure 2.8a), arises from the π-electron network's configuration, making it impossible to pair all $p_z$ orbitals to form π bonds without generating uncompensated radicals. This class of NGs, known as topologically frustrated NGs (TFNGs), can only be constructed for NGs with a total number of hexagons $h \geq 11$, and they constitute an exceedingly small fraction of the total number of NGs for a given value of $h$, with abundances below 0.1%. TFNGs are predicted to exhibit large magnetic-coupling strengths and magnetic state-dependent spatial distribution of frontier orbitals.

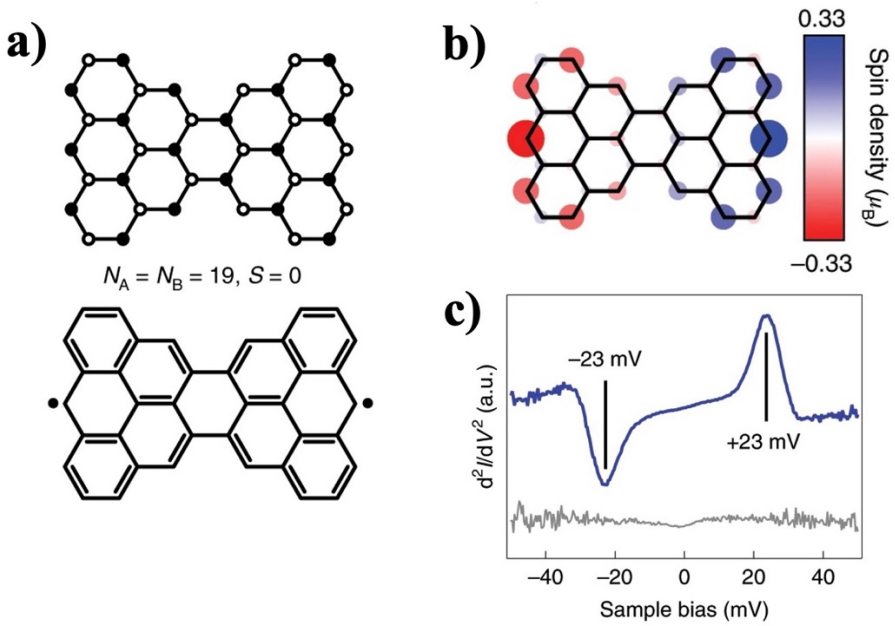


Figure 2.8 (a) Molecular structure of a Clar's goblet: top image showing equal sublattice sites $N_A$=$N_B$=19 with total spin $S$=0; the black solid circles represent the sublattice sites corresponding to $N_A$, while the open circles represent sublattice sites corresponding to $N_B$; bottom image illustrating the conjugated structure with unpaired electrons in both edge terminals. (b) Computed spin density distribution: visualization with blue/red isosurfaces representing spin up/spin down regions showing AFeM nature; **(c)** IETS spectrum: $d^2I/dV^2$ measurement displaying peaks at ±23 mV, indicating electronic transitions associated with the spin states. The blue solid line represents the measurement taken on the molecule, while the gray line corresponds to the substrate. Reproduced from [38] with permission from Springer Nature.

In a landmark paper [38], scientists have made a significant leap in the field of materials science by synthesizing and comprehensively characterizing a nanographene known as Clar's goblet ($C_{38}H_{18}$), a molecule first envisioned by Erich Clar over five decades ago [39]. Clar's Goblet is distinct as the only known planar graphene nanoflake with intrinsic topological frustration, largely due to its all-hexagon structure. Unlike other topologically frustrated systems that often involve a mix of pentagons and heptagons, leading to non-planarity or distortions, Clar's Goblet achieves frustration solely through its hexagonal arrangement. The inability to create a consistent resonance pattern (Kekulé structure) across its π-conjugated hexagonal rings results in competing sublattice interactions, even within a completely planar configuration. Clar's goblet, with its unique bow-tie shape (see Figure 2.8a), defies traditional magnetic conventions through topological frustration, which prevents the pairing of all π-electrons, thereby creating a magnetically non-trivial AFeM ground state as shown in Figure 2.8b. The researchers employed advanced techniques such as STS

and STM to analyze individual molecules deposited on a gold substrate. These techniques unveiled the nanographene's robust AFeM order, characterized by an exchange-coupling strength of 23 meV (see Figure 2.8c), significantly exceeding the Landauer limit for minimum energy dissipation at room temperature. The synthesis of Clar's goblet involves a precursor compound expected to undergo surface-catalysed oxidative ring closure to form the NG. This synthesis highlights the experimental realization and characterization of Clar's goblet, demonstrating a robust antiferromagnetic order.

**Organic Adatoms:**

Organic heteroatoms like boron, nitrogen, oxygen, and such may play a crucial role in introducing magnetism to graphene nanoflakes, enhancing their potential in spintronics and quantum device applications. The incorporation of such heteroatoms into graphene structures significantly alters their electronic and magnetic properties. This doping process introduces localized magnetic moments due to the addition or subtraction of π-electrons by them, which contributes to the overall magnetic behavior of the material. On-surface synthesis has emerged as a promising technique for creating these organic dopants induced graphene nanostructures with atomic precision, allowing for the detailed study of their π-magnetism.

In a recent study, Wang *et al.* delved into the realm of nanoscale materials by successfully synthesizing and analyzing the electronic and magnetic properties of aza-triangulene, a nitrogen-doped triangulene derivative with high spin state [40]. Despite the potential of triangulene and its derivatives in spintronics, the synthesis of stable, heteroatom-doped variants has been limited due to the molecule's high reactivity and the complexity of achieving precise doping. The researchers overcome these hurdles by employing on-surface synthesis techniques, enabling the creation of aza-triangulene with high precision and reproducibility. Figure 2.9a shows the reaction mechanisms of aza-triangulene from heterotriangulene precursor denoted as molecule 1.

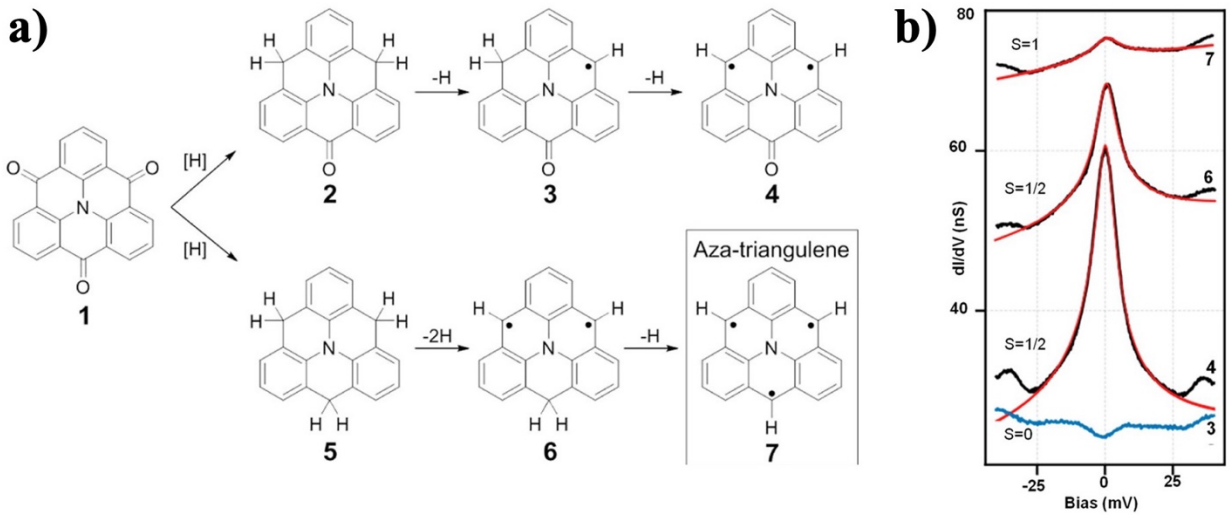


Figure 2.9 (a) Reaction pathway for the synthesis of aza-triangulene derivatives: starting from compound 1, hydrogenation and dehydrogenation steps lead to intermediates 2 through 6, culminating in the formation of aza-triangulene (7). (b) Differential conductance (*dI/dV*) spectra: showing electronic signatures of intermediates 3, 4, 6, and aza-triangulene (7) with spin states *S*=0, *S*=1/2, and *S*=1 achieved after electron transfer towards the underlying gold substrate, indicated for each species as a function of bias voltage. Reproduced from [40] with permission from American Chemical Society.

In their work, the researchers meticulously analyze the Kondo effect as manifested in aza-triangulene adsorbed on Au(111) and Ag(111) substrates, highlighting its profound implications for the molecule's magnetic state. The Kondo effect, a quantum phenomenon that arises from the interaction between a magnetic impurity and the conduction electrons in a metal, manifests as a zero-bias anomaly in electrical resistance at low temperatures. In terms of STS spectra, Kondo resonance appears as a sharp peak at the Fermi level when measuring the differential conductance (*dI/dV*) as a function of applied bias voltage. This peak is the signature of the Kondo effect and the resonance signifies the screening of the magnetic impurity by the conduction electrons of the metal substrate, leading to a many-body bound state that results in an increase in the conductance at low temperatures. The Kondo resonance is a hallmark of the complex quantum interactions between localized and itinerant electronic states in a material. The Kondo resonance observed in their STM experiments provides direct evidence of the open-shell triplet ground state of aza-triangulene (specie 7 in Figure 2.9a) on the Au(111) surface (see Figure 2.9b), which is a pivotal discovery. According to the authors, although free-standing aza-triangulene has *S*=3/2 with three unpaired electrons, it donates an electron to the Au(111) substrate which alters its electronic configuration

and leads to *S*=1 triplet ground state. As shown in Figure 2.9b, STS spectra for different intermediate species of Figure 2.9a enables the observation of Kondo resonances with different amplitudes and shapes corresponding to their various spin configurations. Moreover, the study's findings on Kondo resonance are not just confined to the demonstration of the molecule's magnetic properties but also underscore the potential tunability of these properties by substrate selection. The distinct behavior of aza-triangulene on the Ag(111) surface, where it adopts a closed-shell character, is devoid of the Kondo effect, suggesting that electron donation or acceptance by the substrate plays a crucial role in determining the molecule's magnetic state.

### 2.3.2 Magnetism in 1D Nanoribbon

Graphene nanoribbons with zigzag edges (ZGNRs) are known to host localized edge states that can exhibit magnetism due to the specific arrangement of carbon atoms, creating conditions for magnetic order at room temperature (see Figure 2.10) [41]. However, the study of magnetism in graphene nanoribbons (GNRs) with unpaired electrons, as opposed to traditional magnetism from zigzag edges, is essential for advancing our understanding and utilization of magnetic properties in low-dimensional carbon materials. The presence of unpaired electrons within GNRs introduces a new dimension to the study of magnetism, emphasizing the role of sublattice imbalance and the stability of magnetism in these structures. Unlike the fragile nature of magnetism in zigzag edges, unpaired electrons provide a robust mechanism for inducing magnetic states [42]. The stability of magnetism in sublattice imbalanced nanoribbons with unpaired electrons is crucial, as it determines the feasibility of employing these materials in practical applications. This stability is influenced by various factors, including the edge and bond topologies [43], and can be tailored through specific structural modifications [44]. Moreover, the ability to manipulate the spin states of unpaired electrons in GNRs opens up pathways for designing graphene-based electronic and spintronic devices [45], significantly broadening the scope of potential applications for graphene nanomaterials. In the following paragraph, we will discuss different methods to introduce these unpaired electrons in finite GNR systems, along with specific examples that illustrate their impact on the magnetic properties of these nanostructures.

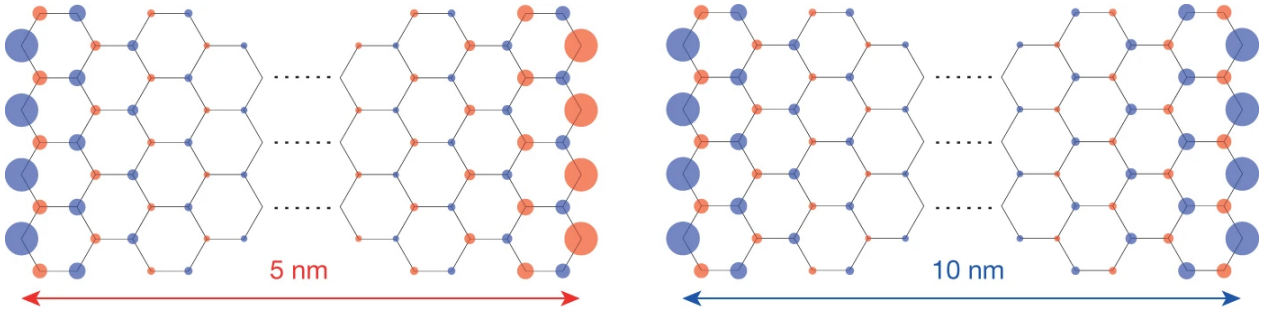


Figure 2.10 Spin density distribution in 5-nm-wide (left) and 10-nm-wide (right) zigzag graphene nanoribbons, where blue indicates up spin and red indicates down spin. The results are calculated using the mean-field Hubbard model at room temperature (300 K) with a Fermi level shift of approximately 100 meV. Reproduced from [41] with permission from Springer Nature.

In their research paper on armchair graphene nanoribbons (AGNRs), Sun *et al.* delved into the strategic manipulation of magnetic properties within GNRs by integrating sublattice imbalanced nanostructures with the modification of edge structure as shown in Figure 2.11a [46]. The core methodology revolves around the incorporation of asymmetric zigzag edge extensions, achieved through the use of specially designed precursor monomers. This innovative approach enables the induction of local magnetic moments within graphene nanomaterials, paving the way towards achieving magnetically nontrivial ground states. In the context of graphene-based systems, magnetically nontrivial ground states can include complex spin arrangements such as localized magnetic moments along edges, spin-polarized zero-energy states, or states arising from sublattice imbalance. The presence of such nontrivial magnetic configurations in graphene-based systems is typically driven by geometric features like edge shape, defects, or topological frustration. The experimental investigation conducted in the study by Sun *et al.* involved synthesizing AGNRs with precise edge modifications. Through STM, the researchers examined isolated and electronically decoupled zigzag edge extensions, uncovering Hubbard-split states that corroborate with theoretical predictions. These Hubbard-split states become especially significant in systems like the zigzag edge extensions of GNRs, where the localized nature of unpaired edge electron amplifies electron correlation effects. Moreover, theoretical simulations using MFH model revealed that the magnetic interactions between pairs of these edge extensions could manifest as ferromagnetic, antiferromagnetic, or diamagnetic, depending on their relative alignment. Figure 2.11 presents a comprehensive examination of the electronic and magnetic interactions facilitated by the introduction of zigzag edge extensions into AGNRs. This figure is pivotal as it encapsulates the

core findings regarding the manipulation of spin states through structural design within GNRs. The figure is divided into several parts, each providing unique insights into the behavior of these coupled spin states:

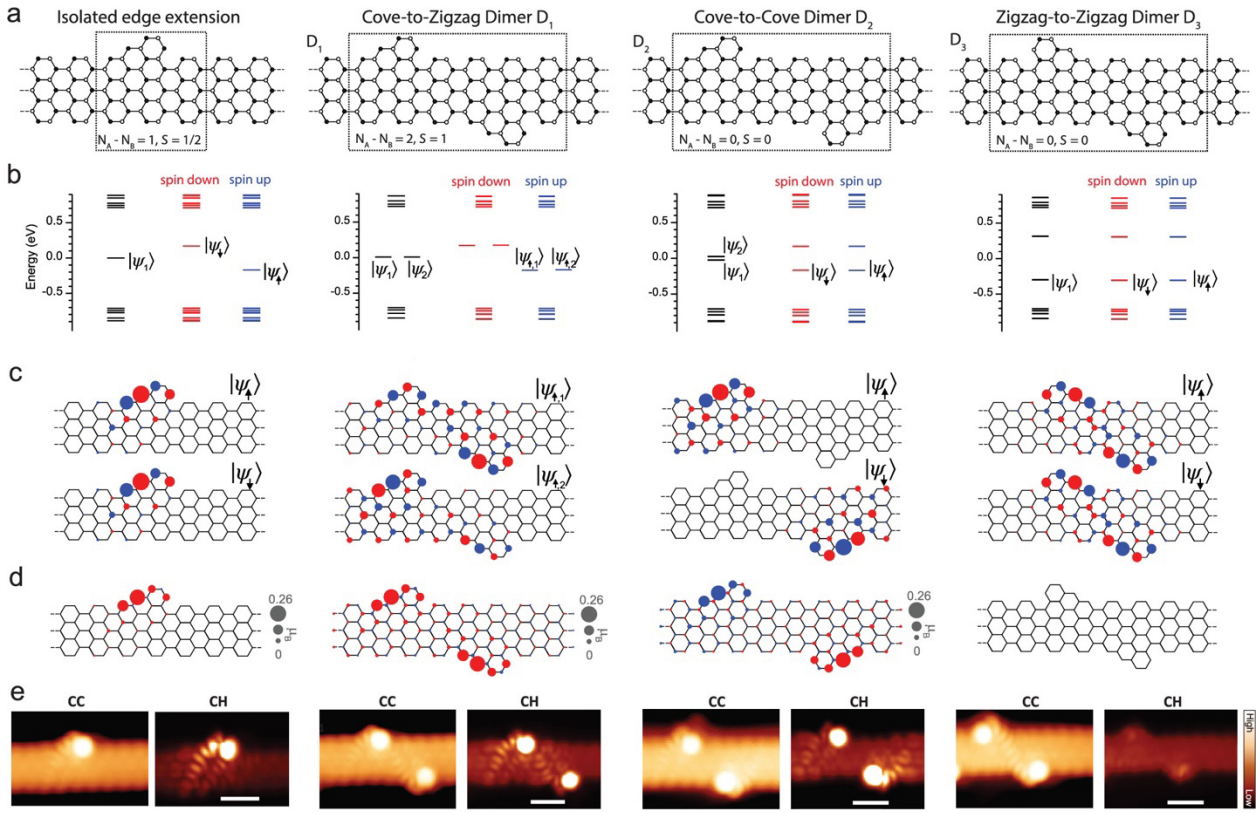


Figure 2.11 (a) Diagrammatic representations: isolated zigzag edge extension and three dimer setups within a 7AGNR, where filled and open circles represent atoms from the A and B sublattices, and *S* denotes the total spin. (b) Energy spectra: nearest-neighbor TB model (black lines, *U*=0 eV) and MFH model (red/blue lines for up/down spins, *U*=3 eV) for the corresponding configurations. (c) MFH-simulated low-energy state wave functions: red/blue markers for opposite wave function phases. (d) MFH-calculated spin density profiles: red/blue isosurfaces showing spin up/down channels and sphere sizes indicating spin density magnitudes in Bohr magnetons ($\mu_B$). (e) STM visualizations: constant current (CC) images and constant height (CH) images for the corresponding structures of (a) on Au(111). Scale bars: 1 nm. Reproduced from [46] with permission from American Chemical Society.

i) Schematic Structures: The top most part of Figure 2.11 illustrates schematic representations of an isolated edge extension and three dimer configurations embedded within a 7-atom-wide armchair GNR (7AGNR). These schematics highlight the precise architectural design employed to induce sublattice imbalances, crucial for the generation of localized magnetic moments. The

representation of filled and open circles designates the atoms belonging to different sublattices, with the total spin number (*S*) indicated for each configuration.

ii) Energy Spectra Analysis: The energy spectra, derived from both nearest-neighbor TB model (with $U$=0 eV) and MFH calculations (with $U$=3 eV), are depicted in Figure 2.11b. This analysis reveals how the introduction of Coulomb repulsion ($U$) splits the energy levels, a phenomenon crucial for understanding the emergence of magnetically nontrivial ground states. The spectra for each configuration are meticulously detailed, providing insights into the stability and nature of the magnetic states induced by the edge extensions.

iii) Wave Function and Spin Density Distribution: Further, Figure 2.11c delves into the wave functions of the low-energy states for the corresponding structures, simulated via the MFH approach. This part of the figure visually represents the spatial distribution of electronic states, crucial for understanding the magnetic coupling mechanisms. Additionally, the spin density distribution maps, illustrated through red/blue isosurfaces for spin up/down channels, offer a visual depiction of the magnetic moment localization and interaction patterns (see Figure 2.11d). These visualizations vividly highlight the varying magnetic ground states that can be engineered through structural modifications, from ferromagnetic interactions in the case of $D_1$ species to antiferromagnetic couplings observed in $D_2$ species. These interactions are contingent upon the relative arrangement and proximity of the zigzag edge extensions. Additionally, the wavefunctions illustrate that, for $D_3$ species, the electronic coupling between spin states is so robust that it results in a closed-shell configuration, effectively neutralizing the net magnetic moment.

iv) STM Imaging: Lastly, constant current (CC) and constant height (CH) STM images provide empirical evidence of the predicted electronic and magnetic properties (see Figure 2.11e). These images validate the theoretical models and calculations, showcasing the realization of different magnetic ground states and the effective decoupling of electronic states from the substrate. The STM images are crucial for correlating the observed electronic characteristics with the predicted magnetic behaviors, effectively bridging the gap between theoretical predictions and experimental observations.

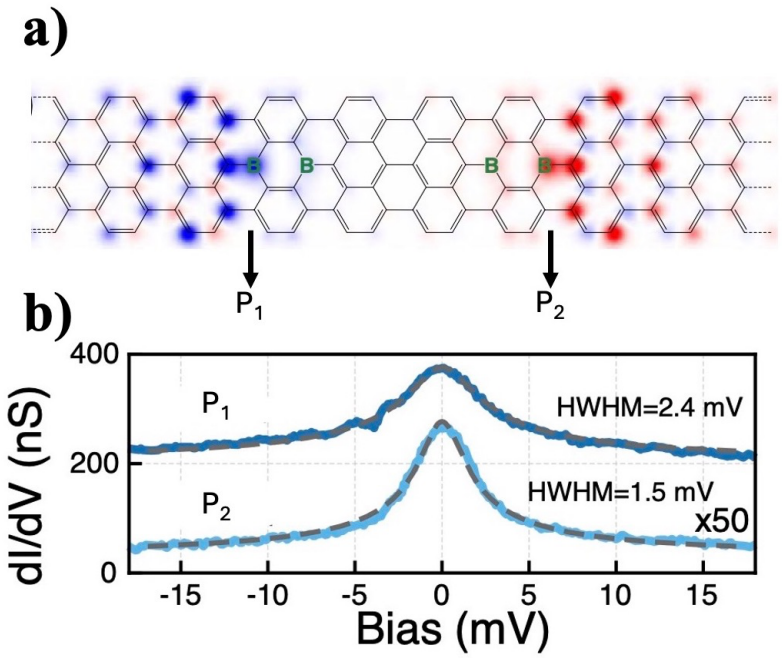


Figure 2.12 (a) Spin density distribution in a boron-doped graphene nanoribbon: visualization of antiferromagnetic coupling at positions $P_1$ and $P_2$, with red and blue indicating spin up and spin down regions. (b) Differential conductance (*dI/dV*) spectra: measured at positions $P_1$ and $P_2$ showing distinct peaks, with half-width at half-maximum (HWHM) values of 2.4 mV and 1.5 mV, respectively, highlighting variations in the electronic density of states. Reproduced from [47] with permission from American Physical Society.

Figure 2.11 conclusively exemplifies the innovative manipulation of magnetic properties through structural modification of AGNRs. By incorporating zigzag edge extensions that induce sublattice imbalances, the research facilitates the emergence of localized magnetic moments and complex magnetic states within graphene-based materials. The findings reveal that the precise control over the electronic and structural parameters of AGNRs allows for the tailoring of their magnetic behaviors, ranging from ferromagnetic to antiferromagnetic, based on the configuration and alignment of the edge extensions. The detailed energy spectra and spin density distributions of Figure 2.11 map these magnetic interactions. STM images provide empirical evidence, showcasing the realization of various magnetic ground states and illustrating the decoupling of electronic states from the substrate, bridging theoretical models with experimental observations. This breakthrough in understanding the interplay between electronic states and magnetic properties through advanced imaging and theoretical modeling not only corroborates with established theoretical predictions but also opens up new avenues for designing materials with desired magnetic properties for future technological applications.

Another research demonstrates that magnetism in AGNRs, can also be induced away from the edges through precise engineering of topological defects in the ribbon's interior [47]. By inserting a pair of substitutional boron atoms into the carbon backbone of AGNRs, the team breaks the conjugation of topological bands, creating two spin-polarized boundary states around the substitution sites (see Figure 2.12a). This innovative approach allows for magnetism to be embedded in GNRs with the help of organic dopants. The study utilizes electrical transport measurements and first-principle simulations to investigate the spin state induced by boron substitution. The findings reveal that the boron pairs introduce a spin 1 state. In the study, the boron-substituted GNRs exhibited clear signs of the Kondo effect, a testament to the induced magnetic states' interaction with the conduction electrons of the substrate similar to the aza-triangulene molecule explained previously. The appearance of the Kondo resonance in differential conductance measurements is indicative of the spin 1/2 states generated around each boron substitution site, engaging in weak interaction with the surrounding electron cloud. In addition, by adjusting the spacing between boron pairs throughout the ribbon chain, the magnetic ground state can be tuned from antiferromagnetic to paramagnetic. Figure 2.12 exhibits the spin-polarization map of boron pair doped AGNRs showing its antiferromagnetic ground state and the Kondo peaks coming from different boron pairs (denoted as $P_1$ and $P_2$ in the figure).

### 2.3.3 Magnetism in 2D Polymer

Evidence suggests that twisted bilayer graphene exhibits magnetism when twisted at the correct angle, yet this magnetic state weakens and vanishes at room temperature [48]. This magnetism arises from the moiré pattern formed by the twist between two layers, which leads to flat electronic bands near the Fermi level and enhanced electron correlations at certain "magic angles." These enhanced correlations can give rise to a variety of emergent phases, including magnetism. However, the delicate nature of these correlated states means they are highly sensitive to thermal fluctuations. As a result, the magnetic ordering is only stable at low temperatures, and thermal agitation at room temperature disrupts the magnetic interactions, causing the magnetism to disappear. Similar to the stability provided by free electron spins in 0D and 1D systems, enhancing magnetism in graphene-like materials is possible. A promising approach to achieve stable magnetism in 2D systems involves synthesizing mesoscale 2D conjugated polymers (2DCP) using magnetic NG precursors. A method to create 2DCPs using triangulene-like monomers involves the synthesis of Kagome polymers.

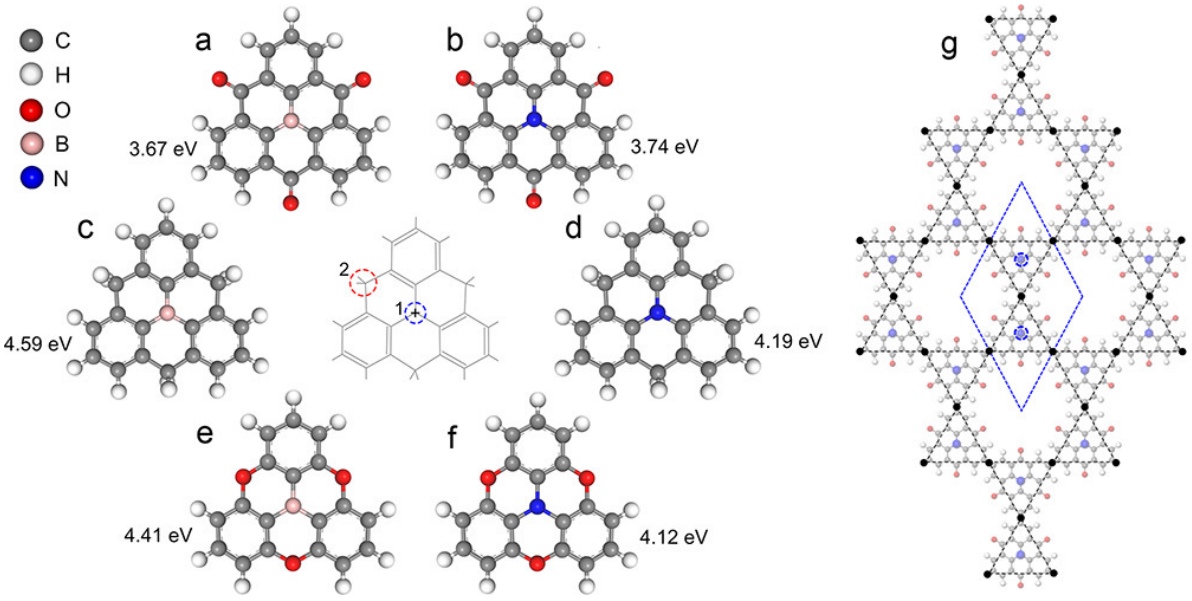


Figure 2.13 Diagram of cationic triangulene and its derivatives: the central triangulene structure is modified by replacing the central $C^+$ atom (1) with boron (B) or nitrogen (N), and $-CH_2$ bridge (2) with either a carbonyl group (C═O) or oxygen (O), forming (a) carbonyl-bridged triphenylborane (CTPB), (b) carbonyl-bridged triphenylamine (CTPA), (c) methylene-bridged triphenylborane (MTPB), (d) methylene-bridged triphenylamine (MTPA), (e) oxygen-bridged triphenylborane (OTPB), and (f) oxygen-bridged triphenylamine (OTPA). HOMO-LUMO gaps are denoted adjacent to the corresponding molecules. (g) Representation of the 2D Kagome lattice, which integrates a regular hexagonal tiling (blue lattice for the unit cell) and a regular triangular tiling (black lattice). Reproduced from [49] with permission from American Physical Society.

The 2D Kagome lattice (2DKL) is a geometric arrangement that presents a fascinating array of unique properties due to its distinct topology (see Figure 2.13g). Characterized by its trihexagonal tiling, it forms a repeating pattern that is analogous to the traditional Japanese basket-weaving technique from which it derives its name. This lattice structure has been explored in various materials, including magnetic and covalent organic frameworks [49-51], revealing an interesting set of electronic and magnetic characteristics. One of the remarkable properties of the 2DKL is its ability to host Dirac points and flat bands in its electronic structure. These features are significant for their potential in realizing high-temperature quantum Hall effect and topologically protected states, which are essential for quantum computing and spintronics applications. For instance, the magnetic properties of decorated 2D Kagome-like lattices have been studied, showing how the geometry influences ferromagnetic and antiferromagnetic ordering, which can be crucial for magnetic storage technologies [52]. Moreover, Kagome lattices have been suggested to exhibit

topologically non-trivial band structures due to their unique atomic arrangements. In practical terms, this means that materials with topologically non-trivial band structures can host exotic surface or edge states that are protected by the topology of the system's electronic band structure. A topologically non-trivial band structure refers to an electronic band structure where the bands possess nonzero topological invariants, such as the Chern number, which are linked to the global properties of the band structure rather than local symmetries. In Kagome lattices, the triangular and hexagonal arrangements of atoms create flat bands and Dirac points, where the electronic states can exhibit strong correlations and nontrivial topological characteristics. These states often lead to unusual and potentially useful electronic properties, such as conducting 1D edge states within an insulating 2D system, as seen in topological insulators. These edge states are robust against local perturbations, such as impurities or defects, due to their topological nature, meaning that they cannot be easily removed or altered. This feature opens up possibilities for utilizing these materials in electronic applications, such as interconnects in next-generation electronics, where they demonstrate low resistivity and high carrier mobility due to the presence of topological edge modes [53-54].

A theoretical study has meticulously delved into the synthesis, structure, and electronic properties of 2DKLs made of several hetero-triangulene monomers (see Figure 2.14), offering profound insights into their potential as Dirac semimetals or single-band semiconductors [49]. The theoretical study is pioneering in its approach, exploring the arrangement of these molecules in an extended 2DKL and meticulously analyzing the resultant electronic structure characterized by the anticipated half-filled Dirac cones at the *K*-points of the Brillouin zone. Furthermore, this study highlights the importance of the electronic structure analysis of these lattices, which reveals their promising characteristics as either Dirac semimetals or single-band semiconductors. In the undoped state (without any B or N dopants in the central position of the heterotriangulene monomers), the electronic structure of the 2DKL is defined by the arrangement of carbon atoms and the inherent symmetry of the lattice. This arrangement results in a unique band structure featuring Dirac cones at the *K*-points of the Brillouin zone at the Fermi level as shown in Figure 2.14(b, e, h) for polymers made of CTP, MTP and OTP monomers, respectively. Despite the central atom of the CTP, MTP and OTP monomers featuring unpaired holes (denoted as atom position 1 in the central triangulene structure in Figure 2.13), the strong interaction through the $sp^2$-hybridized carbon chains results in diamagnetic ground states with a Dirac cone in these polymers. The Kekulé

bonding in the carbon atoms enhances electronic coupling between these unpaired holes, which are separated by approximately 10Å within the Kagome polymer. These polymers behave as Dirac semimetals and suggests that the charge carriers in the material behave as massless Dirac fermions over a range of energies close to the Fermi level similar to pristine graphene. Compared to graphene, where the Dirac bands exhibit a typical linear dispersion crossing the Fermi level at 0 eV, the materials in Figure 2.14(b, e, h) show Dirac-like bands with different energy ranges. In Figure 2.14b, the Dirac bands for CTP based polymer span approximately from -1.5 eV to 1.5 eV around the *K*-point. In Figure 2.14e, the dispersion is narrower for MTP based 2DKL, with the Dirac bands extending from about -0.5 eV to 0.5 eV. In Figure 2.14h, the bands span from approximately -1.0 eV to 1.0 eV for OTP based 2DKL. These energy ranges indicate that while the materials retain Dirac-like characteristics, their band dispersions differ significantly from graphene's near-linear and symmetric band structure around the Dirac point. Along with Dirac cones, the 2DKL also exhibits flat bands near the Fermi level, where the energy levels are highly degenerate and do not disperse with changes in momentum. These flat bands result in localized electronic states that can enhance electron correlation effects, potentially leading to interesting electronic and magnetic properties. The role of dopants, therefore, can be seen as a means to modulate these inherent electronic properties of the Kagome lattice.

By introducing dopants like B or N, one can effectively tailor the band structure to introduce a bandgap, making the material behave more like a single-band semiconductor, and to modify the type and density of charge carriers. When the 2DKL is doped with boron, it leads to the lattice becoming an n-type semiconductor as shown by the band structures in Figure 2.14(a, d, g) for polymers made of CTPB, MTPB and OTPB monomers, respectively. This is achieved by completely emptying the strongly dispersed Dirac bands which increases the number of electrons in the material, making them the primary charge carriers. Conversely, doping with nitrogen results in a p-type semiconductor. This process involves filling the strongly dispersed Dirac bands with one extra electron. Filling these bands increases the number of holes in the material, making them the primary charge carriers (see the band structures in Figure 2.14(c, f, i) for polymers made of CTPA, MTPA and OTPA monomers, respectively). The localized nature of the flat bands can be seen from the charge density plots for the HOMO (LUMO) of B (N) doped polymers. A couple years following the publication of this theoretical study, a new stride in materials science was made when another research team successfully synthesized 2DKL on a mesoscopic scale [50]. They

utilized a method known as Ullmann coupling, a chemical reaction that forms covalent bonds between carbon atoms of organic molecules on metal surfaces, in this case, gold (Au(111)).

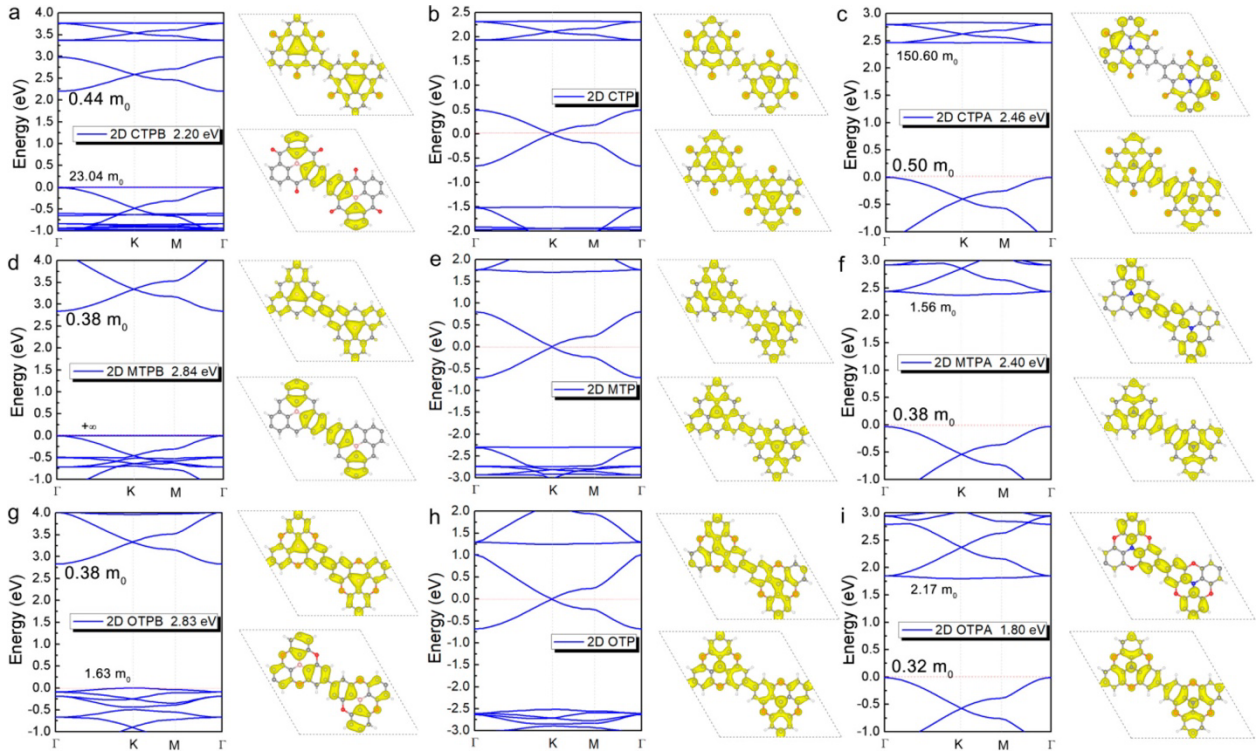


Figure 2.14 Band structures and charge density visualizations of 2D heterotriangulene-polymer derivatives: Panels (a–i) depict the energy bands and corresponding charge density distributions for conduction band minima (CBM) and valence band maxima (VBM) of various HT(B/C/N)-polymers, including 2D CTPB, CTPA, MTPB, MTPA, OTPB, and OTPA, along with 2D CTP, MTP, and OTP. These polymers are based on the monomers depicted in Figure 2.13a–f. Effective masses for the near Fermi frontier bands are noted, with band gaps labeled for semiconductor systems. All calculations are performed at the HSE06 level, with the isosurface for orbitals set to 0.0013 eÅ$^{-3}$. All structures here are non-spin-polarized. Reproduced from [49] with permission from American Physical Society.

This achievement was remarkable because it involved the previously mentioned N doped complex organic molecules CTPA and OTPA, which are challenging to synthesize due to their structural complexity and the precision required to arrange them into a Kagome pattern [50]. This advancement from theoretical modeling to practical realization represents a significant leap in the field, highlighting the potential of complex organic molecules to form novel materials with potentially valuable electronic properties, attributed to the Kagome structure's unique electronic band structure, which can host Dirac fermions and flat bands altogether. However, no magnetic properties were observed yet for this type of 2DKLs in these studies.

In another theoretical exploration by Thomas *et al.*, investigates the emergence of antiferromagnetism in π-conjugated 2DKLs. This study delves into the realm of organic conjugated polymers, shedding light on the potential magnetic properties these materials can exhibit, particularly focusing on the theoretical foundation for an antiferromagnetic Mott insulating phase [51].

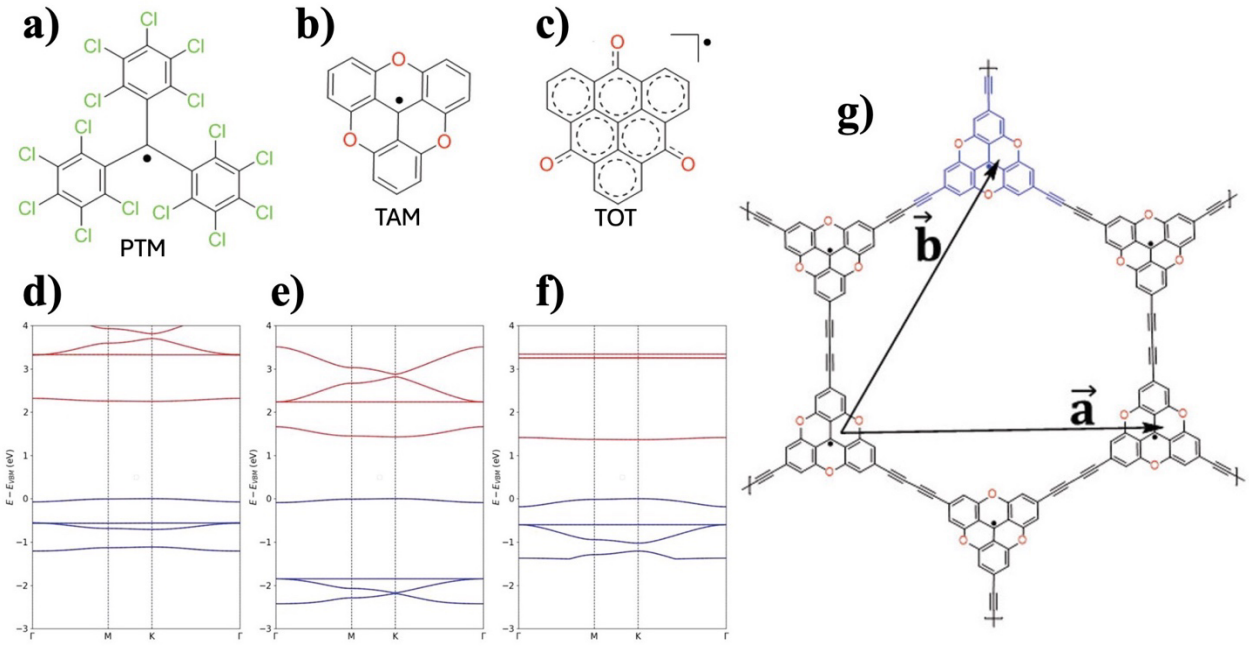


Figure 2.15 Molecular structures of radical molecules: Structure of (a) perchlorotriphenylmethyl (PTM) radical, (b) triarylmethyl (TAM) radical, (c) Structure of trioxotriangulene (TOT) radical. Band diagrams of corresponding polymers made of these radicals: Electronic band structures for the AFeM ground state of (d) PTM, (e) TAM, and (f) TOT based polymers, with valence bands in blue and conduction bands in red. In this AFeM configuration, the spin-up and spin-down bands are superimposed due to degeneracy. The energy is referenced to the Fermi level. Representation of 2DKL with diacetylenic linkers : (g) Structure of a TAM based 2D Kagome polymer where diacetylenic linkers are introduced between the TAM molecules. Reproduced from [51] with permission from John Wiley and Sons.

Unlike prior research, which has largely concentrated on the electrical or structural characteristics of organic materials, this work ventures into the unexplored territory of magnetism within organic conjugated polymers. Central to this theoretical study is the application of hybrid functional density functional theory (DFT) calculations and the Hubbard model, a well-regarded framework for analyzing electron-electron interactions within a lattice. By meticulously examining the electronic and magnetic properties of 2D π-conjugated polymers, the research highlights how the intrinsic chemical versatility of these frameworks enables the tuning of electronic bands around the Fermi

level, leading to significant implications for magnetism. The study posits that the large ratio of on-site Coulomb repulsion ($U$) to nearest-neighbor inter-site electronic coupling ($t$) in these 2DKLs propels them into a stable antiferromagnetic Mott insulating phase under certain conditions. The researchers focused on the theoretical design and analysis of three different 2DKLs where monomers were assigned to PTM, TAM (denoted as CTP in ref. 49), and TOT (denoted as OTP in ref. 49) (see Figure 2.15(a-c)), each based on distinct radical centers. While no actual synthesis was conducted, the theoretical models provided a comprehensive understanding of how these materials could potentially behave in terms of their electronic configurations and magnetic properties. They suggest although these 2DKLs could exhibit nonmagnetic semimetallic phase when the monomers are connected by direct C-C bonds, a quantum phase transition from this nonmagnetic phase to a magnetically ordered antiferromagnetic phase can occur when the monomers are connected by a longer spacer—such as diacetylenic linker (see Figure 2.15g). The complete degeneracy of the AFeM bands in these 2DKLs connected by diacetylenic linkers is depicted in Figure 2.15(d-f). Upon close examination of the electronic structure of their antiferromagnetic ground state, it becomes evident that the HOMO and LUMO exhibit an almost flat profile representing weak inter-site electronic coupling between the nearest neighbor free radicals, which satisfies the Mott insulating behavior observed in these 2DKLs.

## 2.4 Summary

Despite the significant progress in experimental and theoretical research on magnetic graphene nanoflakes and nanoribbons, our understanding of 2D magnetic graphene systems from a practical standpoint remains limited. The scant experimental evidence available points to only weak magnetism within these 2D graphene structures. Furthermore, while certain studies, such as ref. 51, have outlined methods for inducing magnetism in graphene-like 2DKLs, they predominantly focus on AFeM ground states. However, for spintronics applications, it's crucial to transition the magnetic ground state from AFeM to FeM. This shift is vital because ferromagnetic materials exhibit a net magnetic moment that enhances signal detection and manipulation, crucial for the functionality of spintronic devices. Ferromagnetic materials also maintain their magnetic alignment over a broader temperature range and under various operational conditions, enhancing the stability and scalability of spintronic devices. Ultimately, converting to a ferromagnetic ground state can lead to better efficiency in improving performance and increasing data density [52]. Nevertheless, the transition from AFeM to FeM poses a significant challenge, especially since the AFeM state in

these studies is achieved only when monomers are linked by longer chains, such as diacetylenic chains, which could lead to structural instability in practical 2DKL systems. This brings us to several pivotal questions that need addressing. First, how can we effectively tune the magnetic ground state of all organic carbon-based polymers to ensure they are both synthesizable and structurally stable? Second, is it possible to enhance the magnetism in these systems to a level where it remains robust at room temperature? These questions are not merely academic; they have profound implications for the development of advanced materials and devices. On a related note, while there have been efforts to introduce magnetism in 1D GNR chains, the magnetic coupling achieved thus far is insufficient for practical applications, neither sustaining on substrates nor at room temperature. Given the potential of 1D magnetic nanoribbons in quantum circuits, this highlights another critical area of inquiry: how can we enhance the magnetic stability of 1D GNRs? The subsequent section of this thesis aims to delve into these unresolved issues using a theoretical approach, proposing strategies to overcome the current limitations and pave the way for the development of robust, magnetically active graphene-based materials suitable for next-generation technological applications. This theoretical approach includes an in-depth study of the density of states (DOS), local DOS spectra and maps, as well as charge and spin density distributions of the studied species. Additional computational details are provided in **Chapter 3** and further elaborated upon in subsequent chapters, ensuring that the theoretical foundation is robust and well-documented throughout the thesis.

**Chapter 4** takes the questions posed in Chapter 2 further by exploring how to induce robust ferromagnetism in one-dimensional graphene nanoribbons (GNRs). It focuses on the impact of topological defects, such as pentagon edge defects within armchair graphene nanoribbons (AGNRs), on the magnetic properties of these systems. The chapter shows how these defects can disrupt the graphene bipartite lattice and lead to the emergence of highly ordered spin states. By using DFT+U calculations, the chapter demonstrates that these localized spins contribute to the stability of ferromagnetic phases, even in the presence of a metallic substrate. This provides valuable insights into strategies for enhancing the magnetic stability of GNRs.

**Chapter 5** extends this exploration to two-dimensional Kagome polymers based on triangulene monomers. It investigates the possibility of achieving ferromagnetic phases in these 2D systems through strategic doping with boron or nitrogen atoms. The chapter reveals that while all-carbon triangulene polymers typically exhibit an antiferromagnetic ground state, doping can stabilize a

ferromagnetic phase with promising electronic properties. The boron-rich polymers show high carrier mobilities, which are essential for spin-based logic devices, whereas nitrogen-rich polymers exhibit half-metallic behavior, advantageous for quantum storage applications. This chapter further elucidates the relationship between symmetry, electronic structure, and magnetism in 2D Kagome lattices, contributing to the broader goal of developing tunable, low-dimensional organic magnets.

**Chapter 6** builds on the work of Chapter 5 by focusing on carbon-doped boron nitride polymers arranged in a 2D framework. It examines how carbon substitution in triangular boron nitride (tBN) monomers can create spin-polarized ground states and long-range magnetic order in these traditionally insulating materials. The study shows that specific carbon-doped configurations introduce collective magnetism and create semiconductor properties with coexisting Dirac and flat bands near the Fermi level. This chapter also explores how varying the arrangement of doped monomers affects electronic and magnetic properties, providing a deeper understanding of how defect-engineered and doped 2D materials can be optimized for spintronic applications.

**Chapter 7** concludes this investigation by examining magnetism in heterotriangulene-based Kagome polymers, specifically those made from trioxoazatriangulene (TANGO) monomers. Through a combination of experimental AFM/STM imaging and DFT+U calculations, the chapter explores the emergence of spin-polarized states and localized magnetic moments when unpaired electrons are introduced via chemical modification. It also delves into how defect concentration and symmetry breaking impact the magnetic and electronic properties of the polymer, leading to increased band localization and disruption of Dirac cones at the *K*-points of the Brillouin Zone. By validating these theoretical predictions with experimental results, this chapter paves the way for the practical integration of organic magnets. This final chapter ties together the insights from the earlier chapters, reinforcing the thesis objective of advancing the development of robust, tunable organic spintronic materials.

# CHAPTER 3 COMPUTATIONAL DETAILS

This section provides a comprehensive yet brief overview of the computational methods and details employed in this study to investigate the electronic and magnetic properties of low-dimensional carbon-based polymers. The discussion includes the rationale behind selecting specific computational approaches, the implementation of different DFT methods, and the detailed procedure for determining the Hubbard U parameter for DFT+U simulations.

## 3.1 Computational Methods

The electronic and magnetic properties of low-dimensional organic materials were examined using Density Functional Theory (DFT) calculations. We employed both standard DFT using the Perdew-Burke-Ernzerhof (PBE) functional and more sophisticated approaches, including hybrid functionals and the DFT+U method, to enhance the description of localized electron interactions and magnetic behaviors. While hybrid functional DFT generally provides highly accurate results by better capturing exchange-correlation effects, we opted for the DFT+U method as it offers a practical compromise between computational efficiency and accuracy, particularly well-suited for systems with strong electronic correlations. Additional justifications for our preference of DFT+U over other DFT approaches are provided in Appendix B. The Quantum ESPRESSO package was utilized for all DFT computations, incorporating the Projector-Augmented Wave (PAW) method to model ion-electron interactions effectively [55-56]. For readers interested in gaining a deeper understanding of DFT, consider ref. 57 and 58.

Although Mean-Field Hubbard (MFH) models are widely used for magnetic graphene systems [36-38], we chose DFT+U and other DFT-based methods for several reasons. First, DFT+U provides a more accurate treatment of electron correlations by explicitly incorporating an on-site Coulomb interaction, which is crucial for accurately describing localized orbitals. In contrast, the MFH model relies on a mean-field approximation that tends to oversimplify interactions, neglecting important quantum mechanical effects such as fluctuations. This oversimplification often leads to inaccuracies in predicting magnetic properties, electron localization, and electronic structures. Moreover, the MFH model is subject to spin contamination, where the mean-field approximation can lead to an incorrect description of the spin state due to the inability to properly account for quantum fluctuations and correlations. This is particularly problematic for systems with complex magnetic ordering, as the spin states derived from MFH calculations may not faithfully represent

the true spin configuration of the system. On the other hand, DFT+U offers a more nuanced treatment of spin configurations, allowing for a more accurate prediction of magnetic behaviors and avoiding issues like spin contamination. Additionally, the semi-empirical nature of the MFH model represents a significant downside. The parameters in MFH are often fitted to experimental data or extracted from simpler calculations, which limits its predictive power and versatility. This semi-empirical approach makes MFH less reliable when applied to new or complex materials without established parameter sets. In contrast, DFT+U is a first-principles method, meaning it is grounded in quantum mechanical theory with fewer empirical inputs, which enhances its predictive capabilities across a broader range of systems. Our study focuses on periodic, large-scale graphene-based systems where substrate effects play a significant role. The DFT+U method allows for a more accurate modeling of these substrate interactions compared to the MFH model, which lacks the flexibility to properly account for such environmental influences. Given the complexity of our system, including the need to accurately model periodic boundary conditions and the effects of substrates, DFT+U emerged as the optimal choice, balancing accuracy with computational feasibility while avoiding the limitations inherent in the MFH model.

### 3.1.1 Simple DFT with PBE Functional

Initially, standard DFT calculations were conducted using the PBE+D2 functional. This approach is known for its general accuracy in predicting structural properties and is widely used in electronic structure calculations. Density Functional Theory (DFT) forms the basis for the electronic structure calculations performed in this study. The Kohn-Sham equations, which are central to DFT, express the complex interactions between electrons in a simplified framework as follows:

$$\widehat{\mathrm{H_{KS}}}\psi_i(\mathbf{r}) = \epsilon_{\mathrm{i}}\psi_i(\mathbf{r}) \tag{3.1}$$

where:

- $\widehat{H_{KS}}$ is the Kohn-Sham Hamiltonian, incorporating both kinetic energy and effective potential (which includes external potential, electron-electron Coulomb interaction, and exchange-correlation effects).
- $\psi_i(\mathbf{r})$ are the Kohn-Sham orbitals (or wavefunctions).
- $\epsilon_{\mathrm{i}}$ are the eigenvalues corresponding to the energy levels of the system.

The goal is to determine the ground-state electronic density $n(\mathbf{r})$, given by:

$$n(\mathbf{r}) = \sum_{\mathrm{i}}^{\mathrm{occ}} |\psi_i(\mathbf{r})|^2 \tag{3.2}$$

The sum runs over all occupied states. The density $n(\mathbf{r})$ is then used to recalculate the effective potential in the Kohn-Sham Hamiltonian iteratively until self-consistency is achieved.

The total energy of the system within DFT is expressed as:

$$\mathrm{E_{DFT}}[\rho] = \mathrm{T_s}[\rho] + \int \mathrm{v_{ext}}(\mathbf{r}) n(\mathbf{r})\ \mathrm{dr} + \frac{1}{2}\int\int \frac{n(\mathbf{r})n(\mathbf{r}')}{|\mathrm{r}-\mathrm{r}'|}\ \mathrm{d}\mathbf{r}\,\mathrm{d}\mathbf{r}' + \mathrm{E_{XC}}[\rho] \tag{3.3}$$

where:

- $T_s[\rho]$ is the kinetic energy of non-interacting electrons.
- $v_{\mathrm{ext}}(\mathbf{r})$ represents the external potential.
- The second integral accounts for the Coulomb interaction between electron densities.
- $E_{\mathrm{XC}}[\rho]$ is the exchange-correlation functional, which is crucial in determining the accuracy of the results.

Exchange-correlation effects in DFT are crucial in accurately capturing the quantum many-body interactions among electrons and these effects are included through this exchange-correlation functional, typically approximated as local or semi-local (e.g., LDA or GGA). These functionals provide a good balance between computational efficiency and accuracy for many systems, especially metals and simple semiconductors. However, these approximations struggle when dealing with strongly correlated systems, such as transition metal oxides or localized f-electron systems, where the electron-electron interaction effects are significant [59]. This is where the exchange-correlation effects in DFT fall short [60], leading to problems like underestimated band gaps or incorrect magnetic properties.

The Hubbard term, introduced in the DFT+U method, is added specifically to address these limitations. In systems where localized d or f electrons play a critical role, the standard exchange-correlation functionals fail to fully capture the on-site Coulomb interactions due to the significant overlap and strong repulsion among electrons in localized orbitals. The DFT+U method enhances the accuracy of DFT by including an explicit on-site Coulomb repulsion term, known as the

Hubbard *U* term, which corrects for the self-interaction error and improves the description of localized electronic states. In essence, DFT+U can be considered as a hybrid approach that bridges the gap between standard DFT and more advanced many-body methods, providing a mean-field correction for systems with strong electronic correlations. The Hubbard term acts as a corrective measure by penalizing the occupancy of electrons in localized states, thereby favoring the correct electronic configurations, spin alignments, and orbital occupations that might be missed by the approximate exchange-correlation functional in conventional DFT. The introduction of the *U* term effectively splits the degenerate energy levels of localized electrons, leading to a better description of the electronic and magnetic properties of correlated materials. This correction allows for the opening of band gaps in systems that are incorrectly predicted as metallic by standard DFT and provides a more realistic depiction of magnetic ordering. Consequently, DFT+U offers a better compromise between computational cost and the accuracy required for systems with partially filled d or f orbitals, where the exchange-correlation effects alone are insufficient to capture the physics accurately [59]. It is also necessary to study systems with localized p orbitals, such as those found in graphene-like systems with unpaired electrons. In these systems, localized p orbitals can give rise to significant electron-electron interactions that are not adequately described by standard DFT. The presence of unpaired electrons in localized p orbitals, often seen in defects or edge states in graphene nanostructures, can lead to magnetic behavior and complex correlation effects. The DFT+U approach helps in accurately modeling these localized p orbital interactions, thereby providing a better understanding of the magnetic and electronic properties of graphene-like systems.

### 3.1.2 DFT+U Approach

The DFT+U method was employed to address the shortcomings of standard DFT. The DFT+U approach introduces an additional Hubbard term *U* to the standard DFT functional to account for the on-site Coulomb repulsion among localized electrons.

$$\mathrm{E_{DFT+U}} = \mathrm{E_{DFT}} + \mathrm{U}\sum_{\sigma}\left(\langle n_{i\sigma}\rangle - \frac{1}{2}\langle n_{i\sigma}\rangle^2\right) \tag{3.4}$$

Here, $n_{i\sigma}$ represents the dimensionless occupation number of localized orbitals for spin $\sigma$.

This correction enhances the description of correlated electron systems by improving the localization of open-shell electronic states and, consequently, providing a more accurate

representation of magnetic properties. The importance of this approach is underscored by its ability to stabilize magnetic ground states and correctly predict band gaps [59].

### 3.1.3 Hybrid Functional DFT

Hybrid functional DFT, such as the PBE0 method [61], incorporates a portion of exact Hartree-Fock exchange energy along with the DFT exchange-correlation functional. The energy expression for a hybrid functional is:

$$E_{\text{Hybrid}} = (1 - \alpha)E_{\text{XC}}^{\text{DFT}} + \alpha E_{\text{X}}^{\text{HF}} + E_{\text{C}}^{\text{DFT}} \tag{3.5}$$

where:

- $E_{\text{XC}}^{\text{DFT}}$ is the exchange-correlation energy from a standard DFT functional.
- $E_{\text{X}}^{\text{HF}}$ is the exact exchange energy from Hartree-Fock theory.
- $\alpha$ is a mixing parameter, typically around 0.25, representing the fraction of Hartree-Fock exchange included.
- $E_{\text{C}}^{\text{DFT}}$ is the correlation energy from DFT.

While hybrid functionals offer improved accuracy over standard DFT by addressing some of the limitations related to electron delocalization and band gap underestimation, they are computationally more demanding and less practical for large systems [49, 51].

## 3.2 Implementation Details

In this thesis, spin-polarized calculations were carried out with spin alignment fixed along the z-direction for consistency. For PBE0 calculations, a default Hartree-Fock exchange parameter of 25% was employed similar to previous study [51]. The DFT+U approach was implemented to refine the description of electronic properties by incorporating the Hubbard *U* correction [59]. In this study, the choice of the DFT+U approach was favored for its balance between computational efficiency and accuracy. It provided comparable results to hybrid functionals but with lower computational cost, making it suitable for the large-scale computations required for analyzing the magnetic polymers, which will be discussed in detail in Chapter 5.

## 3.3 Hubbard U Parameter Selection

The Hubbard *U* parameter is crucial for accurately describing the localization of electrons in correlated systems. In this study, the U parameter was calculated for all symmetric carbon sites in the unit cell using the Linear-Response Method (LRM), as introduced by Cococcioni and de Gironcoli [59]. This method involves the following steps.

### 3.3.1 Linear-Response Method

The Linear-Response Method is a computational technique used within the Density Functional Theory (DFT) framework, particularly in the DFT+U approach, to determine the Hubbard *U* parameter. This parameter is crucial for accurately describing the on-site Coulomb interactions among localized electrons, typically in systems with strongly correlated d or f electrons. The method, as introduced by Cococcioni and de Gironcoli, involves perturbing the system and observing its response to calculate the *U* parameter [59]. The primary steps involved in this method are outlined below:

i) **Initial Self-Consistent Field (SCF) Calculation**: The procedure starts with a standard SCF calculation of the system within the DFT framework to obtain a reference electronic density and ground-state wavefunction. This calculation provides a baseline description of the system without any perturbation, capturing the initial electronic configuration of the localized orbitals.

ii) **Perturbation of the Localized Orbitals**: A small perturbation is applied to the potential associated with the localized orbitals, typically affecting the d or f orbitals of transition metals or rare earth atoms. The perturbation is introduced in the form of an external potential ($V_{ext}$), and is kept small to ensure that the system's response remains within the linear regime, making the linear response theory valid.

iii) **Measurement of Changes in Occupation**: After applying the perturbation, the system undergoes another SCF calculation to determine the new electronic density and occupation numbers of the localized orbitals. The change in the occupation number ($\delta n$) of the localized orbital due to the applied perturbation ($V_{ext}$) is then measured. It is crucial that the perturbation is small enough to prevent any significant electronic rearrangement, thus maintaining the assumption of linearity.

iv) **Calculation of the Linear Response Function**: The linear response function ($\chi$) is calculated as $\chi = \frac{\delta n}{\delta V_{ext}}$. This function quantifies how sensitive the occupation of the localized orbitals is to changes in the external potential, essentially describing the response of the electron density in the correlated subspace.

v) **Non-Interacting Response Function**: A similar procedure is used to determine the non-interacting response function ($\chi_0$), which is obtained by calculating the response of the system without considering explicit on-site interactions. This non-interacting response serves as a reference point for understanding the impact of electron-electron interactions.

vi) **Calculation of the Hubbard U Parameter**: The Hubbard *U* parameter is then extracted as $U = \frac{1}{\chi} - \frac{1}{\chi_0}$. This equation effectively measures the energy cost of placing two electrons on the same localized orbital, quantifying the strength of the on-site Coulomb repulsion. The difference between the two response functions captures the extent to which the localized electrons are screened by the rest of the system.

vii) **Self-Consistency and Convergence**: In practical applications, the LRM procedure may need to be repeated iteratively to ensure convergence of the U value. Once a reliable value is obtained, it can be used in subsequent DFT+U calculations to improve the description of the localized electrons.

The implementation of this method is facilitated by Quantum ESPRESSO [55], which provides routines for performing these calculations. Quantum ESPRESSO allows users to automate the application of perturbations, measure the resulting changes in orbital occupations, and ultimately calculate the response functions. This ensures that the additional Coulomb repulsion term introduced in the DFT+U calculations accurately reflects the localized nature of the electron interactions in the system.

The LRM offers several advantages, including self-consistency, accuracy, and broad applicability. It ensures that the calculated *U* parameter is consistent with the electronic structure of the material, reducing the need for empirical fitting. By directly measuring the system's response, it provides an accurate description of on-site Coulomb interactions, enhancing the predictive power of DFT+U calculations for materials with strongly correlated electrons. For example, in battery cathode materials, self-consistent *U* values obtained using the LRM provided redox potentials in much

better agreement with experimental data compared to conventional DFT calculations [59]. Additionally, studies have shown that the method improves band gap predictions and reaction energies for transition metal oxides [62]. The accuracy of the method is further demonstrated in its application to predict the Raman spectra of strongly correlated systems, showing significant improvements over standard DFT [63]. The LRM is thus an essential tool for studying strongly correlated electron systems, providing reliable and self-consistent parameters for DFT+U calculations. In summary, the LRM is a robust and accurate approach for determining the Hubbard *U* parameter in DFT+U calculations, ensuring self-consistency and improving the accuracy of electronic structure predictions. Its mathematical rigor and practical implementation make it indispensable for investigating complex materials with strongly correlated electrons.

### 3.3.2 Validation and Adjustment

The accuracy of the *U* value was validated by comparing the results obtained from DFT+U calculations with those from hybrid functional DFT (PBE0) and standard DFT methods. The *U* values were adjusted to ensure that the calculated electronic and magnetic properties align well with experimental observations and theoretical expectations. This process included:

i) Comparison of *J* Values: The spin-exchange parameter (*J*) was calculated for different polymers using simple PBE, PBE0, and DFT+U methods. Significant differences were observed between simple PBE and the other methods, particularly in band gap values and magnetic ground state predictions (explained in details in Chapter 4).

ii) Analysis of Band Gaps: The band gap values were carefully analyzed to ensure that the DFT+U method corrected for the band delocalization issues observed with simple PBE. This correction was crucial for obtaining accurate magnetic ground states and electronic properties.

### 3.3.3 Practical Considerations

The practical implementation of the Hubbard *U* parameter involved using default codes included with the Quantum ESPRESSO package, which provided a streamlined approach to calculating and applying *U* values. The choice of *U* values was based on achieving a balance between computational efficiency and accuracy in describing the electronic structure and magnetic properties of the Kagome polymers.

## 3.4 Calculation of Local Dipole Moment

### 3.4.1 Charge Density Calculation

The electronic charge density $n(\mathbf{r})$ in a material is a key quantity obtained from DFT calculations. The total charge associated with an atom within a specific region, often a sphere around the atomic nucleus, can be calculated by integrating the charge density over that region. The integration is typically performed within a sphere of radius $r_m$ centered at the atomic site.

The total charge $Q_i$ associated with the $i$-th atom is given by:

$$Q_i = \int_{|\mathbf{r}-\mathbf{R}_i|<r_m} n(\mathbf{r})d\mathbf{r} \tag{3.6}$$

where:

- $n(\mathbf{r})$ is the electronic charge density at position $\mathbf{r}$,
- $\mathbf{R}_i$ is the position of the $i$-th nucleus,
- $r_m$ is the integration radius, typically determined as a fraction of the minimum interatomic distance to avoid overlap between neighboring atoms.

In practice, this integration is often performed numerically using a weighted sum over discrete points in space:

$$Q_i = \sum_{|\mathbf{r}_k-\mathbf{R}_i|<r_m} w_k n(\mathbf{r}_k) \tag{3.7}$$

where:

- $\mathbf{r}_k$ are the discrete points within the sphere,
- $w_k$ are the weights assigned to each point based on their distance from the nucleus.

The weighting function $w_k$ can be defined as:

$$w_k = \begin{cases} 1 & \text{if } |\mathbf{r}_k - \mathbf{R}_i| \le r_m \\ 1 - \dfrac{|\mathbf{r}_k - \mathbf{R}_i| - r_m}{0.2 \times r_m} & \text{if } r_m < |\mathbf{r}_k - \mathbf{R}_i| \le 1.2 \times r_m \\ 0 & \text{if } |\mathbf{r}_k - \mathbf{R}_i| > 1.2 \times r_m \end{cases} \tag{3.8}$$

### 3.4.2 Magnetic Moment Calculation

The magnetic moment associated with an atom is derived from the spin density, which is the difference between the charge densities of spin-up ($n^{\uparrow}(\mathbf{r})$) and spin-down ($n^{\downarrow}(\mathbf{r})$) electrons. The local magnetic moment $M_i$ for the $i$-th atom is calculated as:

$$M_i = \int_{|\mathbf{r}-\mathbf{R}_i|<r_m} \left(n^{\uparrow}(\mathbf{r}) - n^{\downarrow}(\mathbf{r})\right) d\mathbf{r} \tag{3.9}$$

This integral is similarly performed as a weighted sum over the discrete points within the spherical region:

$$M_i = \sum_{|\mathbf{r}_k-\mathbf{R}_i|<r_m} w_k \left(n^{\uparrow}(\mathbf{r}_k) - n^{\downarrow}(\mathbf{r}_k)\right) \tag{3.10}$$

### 3.4.3 Practical Considerations

**(i) Choice of Integration Radius $r_m$ :**

The choice of the integration radius $r_m$ is crucial for accurately calculating the charge and magnetic moment around each atom. The radius $r_m$ is set to a value slightly smaller than the minimum interatomic distance divided by 2 × 1.2 [55]:

$$r_m = \frac{d_{\min}}{2 \times 1.2} - \epsilon \tag{3.11}$$

where:

- $d_{\min}$ is the minimum distance between any two neighboring atoms,
- $\epsilon$ is a small value to ensure that no point in space belongs to more than one atom's integration sphere.

This choice of $r_m$ ensures that the integration sphere around each atom does not overlap with the spheres of neighboring atoms, preventing double-counting of charge or spin densities. It also allows for a well-defined and localized calculation of charge and magnetic moment, leading to more accurate and physically meaningful results.

**(ii) Numerical Implementation:**

In practical DFT calculations, these integrations are carried out using a mesh of points within the spherical region, and the precision of these calculations depends on the density of this mesh.

**(iii) Physical Interpretation:**

The charge $Q_i$ and magnetic moment $M_i$ obtained from these calculations represent the localized quantities within the integration sphere. These quantities provide insight into the electronic structure and magnetic properties at the atomic level, contributing to the overall understanding of the material's behavior.

The calculation of charge and magnetic moments in Quantum ESPRESSO involves numerical integration over a defined spherical region around each atom. The results depend on the careful selection of the integration radius and the accurate summation of contributions from discrete points within this region. This method, though specific to the code's implementation, provides a valuable means of analyzing electronic and magnetic properties in complex materials.

## 3.5 Calculation of STM Images

Calculating STM images from Quantum ESPRESSO involves a series of steps rooted in DFT and the Tersoff-Hamann method. The process begins with performing DFT calculations using Quantum ESPRESSO, where the Kohn-Sham equations are solved to obtain the electronic structure of the system. The wavefunctions $\psi_i(\mathbf{r})$ and eigenvalues $_i$ from these calculations are crucial for subsequent steps.

### 3.5.1 Tersoff-Hamann Method for LDOS

The Tersoff-Hamann method is employed to relate the LDOS to the tunneling current in STM. According to this method, the tunneling current $I$ is proportional to the LDOS integrated over an energy window near the Fermi level:

$$I \propto \int_{E_F}^{E_F+eV} \mathrm{LDOS}(\mathbf{r}, E)\ dE \tag{3.12}$$

Here, $E_F$ is the Fermi level, and $V$ is the bias voltage. The LDOS is obtained using the Kohn-Sham states and is given by:

$$\mathrm{LDOS}(\mathbf{r}, E) = \sum_i |\psi_i(\mathbf{r})|^2 \delta(E - \epsilon_i) \tag{3.13}$$

### 3.5.2 Simulation of the STM Images

Once the LDOS is calculated, two types of STM images can commonly be generated:

**(i) Constant-Current STM**: The tip height $z(\mathbf{r})$ is adjusted to keep the tunneling current constant. The current is related to the integrated LDOS, and the image reflects the variation in tip height required to maintain the constant current.

**(ii) Constant-Height STM**: The tip remains at a fixed height, and the image reflects variations in the tunneling current as the tip scans across the surface.

Finally, the simulated STM images are visualized using our own plotting tools.

## 3.6 Summary

In summary, the computational details provided herein highlight the preference for the DFT+U approach over simple DFT and hybrid functional DFT in studying the electronic and magnetic properties of carbon based low-dimensional polymers. While simple DFT with the PBE functional was used as a baseline, it was insufficient in accurately describing the electronic and magnetic properties of the polymers due to its underestimation of electron-electron interactions. Hybrid functional DFT, although more accurate, was computationally expensive and less practical for large systems. The DFT+U method effectively addresses the limitations of simple DFT by improving the localization of electronic states and accurately predicting magnetic properties while maintaining computational efficiency. The detailed procedure for determining the Hubbard U parameter ensures that the calculations are both accurate and reliable, providing a solid foundation for the investigation of the electronic and magnetic properties of the studied polymers. These computational details form the basis for understanding the electronic and magnetic behaviors of the Kagome polymers and support the analysis of their potential applications in advanced material science.

# CHAPTER 4 ARTICLE 1- SPIN-POLARIZED TOPOLOGICAL PHASES IN GRAPHENE NANORIBBONS WITH NON-BENZENOID DEFECTS

Khalid N. Anindya and Alain Rochefort

Published in The Journal of Physical Chemistry C, 127(46), pp.22856-22864, November 10, 2023

*Chapter 4 delves into the exploration of magnetic phases in one-dimensional graphene nanoribbons (GNRs) and their potential for spintronics applications, addressing the central challenge of inducing robust ferromagnetism in these systems. Building on the broader thesis objective of transitioning from antiferromagnetic to ferromagnetic phases, we focus on the impact of pentagon edge defects within armchair graphene nanoribbons (AGNRs) and demonstrate how these non-benzenoid topological defects disrupt the graphene bipartite lattice, leading to the emergence of highly ordered spin states. Through DFT calculations, we reveal how these defects generate localized spins while largely preserving the underlying topological phases. Furthermore, we investigate the role of boron dopants in enhancing magnetic stability, a critical factor for achieving room-temperature ferromagnetism suitable for practical applications. Recognizing the importance of real-world conditions, we also examine the influence of a metallic substrate on these modified nanoribbons, showing that while substrate screening effects are significant, the magnetic character persists, offering valuable insights into the coexistence of robust magnetism and topological phases. This chapter therefore addresses key unresolved questions regarding the magnetic stability of GNRs, presenting strategies to enhance their suitability for next-generation spintronic devices. By introducing defect-engineered and dopant-stabilized approaches, this work advances the understanding of how localized spins can be manipulated to create stable ferromagnetic phases within low-dimensional graphene nanoribbons, paving the way for their integration into future technological applications.*



**Abstract :**

We have used density functional theory calculations to demonstrate that the presence of unsaturated pentagon edge defects within an armchair graphene nanoribbon can generate highly ordered and

robust spin states in this otherwise diamagnetic system. Such pentagon defects create disruption of the bipartite AB lattice of graphene in which the local defect state interferes quite weakly with the delocalized π-electrons of the backbone that form topological phases. The incorporation of boron pairs among such nanoribbons changes the stability of the magnetic phases and provides supplemental magnetic robustness due to an additional local rupture potential introduced by the dopants. Although the presence of a metallic substrate influences the electronic and magnetic properties of most nanoribbons, the magnetic character of the modified nanoribbons is not completely screened by the metal. This work provides new molecular concepts in organic magnetism, where topological and robust magnetic phases may coexist.

## 4.1 Introduction

In recent years, we have observed a great interest for graphene-based topological insulators owing to their extraordinarily robust surface states alongside the traditional insulator-like energy gap [64,65]. In addition, potentially straightforward tunable topological phases in one-dimensional graphene nanoribbons (GNRs) have been investigated, at both the theoretical [66] and experimental [67] level. On the other hand, magnetism in graphene-based materials is another fascinating domain because of their protracted spin-coherence time, which originates from the low spin-orbit coupling and nuclear spins in graphene [68,69]. Although bottom-up synthesis has the potential to control the edge and width of GNRs [70,71], inducing stable magnetism in graphene systems still remains quite challenging [72]. GNRs with zigzag edges (ZGNR) are likely to possess localized edge states with ordered spins [73−75], although such magnetism is very fragile in nature. In certain conditions, magnetic edge states in ZGNRs might not be as stable as previously thought, which can affect the reliability of the results derived from such systems [76]. In addition, ZGNRs exhibit stability problems, particularly when subjected to ambient conditions, necessitating protective measures before their utilization or transfer [77]. Furthermore, the presence of edge vacancies in ZGNRs has a more profound effect on their properties compared to armchair edge GNRs (AGNR), potentially complicating their behavior in certain applications [78]. On the other hand, AGNRs with edge defects can offer a controlled environment for studying edge magnetism and understanding electron−electron interactions, emphasizing their potential in advancing graphene-based materials research [79,80]. However, introducing a magnetic moment in GNRs with armchair edges requires further treatment to achieve sublattice imbalance in the graphene bipartite lattice system [46]. According to Lieb's theorem, this may introduce high-spin states on the

imbalanced lattice site [81]. An alternative strategy to generate high-spin sites in graphene systems is by introducing non-benzenoid topological defects, which can be used to tune the magnetic [82], electronic [83,84], and chemical [85] properties of graphene-based materials. It is imperative to mention here that various defects, including pentagonal structures, can emerge in graphene during synthesis. The edge shapes of GNRs are diverse, and their properties can be significantly influenced by these defects [86]. Experiments have observed pentagonal defects in graphene nanoribbons, emphasizing their potential in influencing electronic properties [33]. A theoretical study has predicted that edge modification of AGNRs with pentagon edges can lead to zero-energy flat bands and can stabilize spin-polarized edge states [87]. Nonetheless, considerably less work has been done to exploit the magnetic behavior in topological GNRs with non-benzenoid defects.

In this work, we first considered the presence of pentagon defects within a simple AGNR to describe their influence on the existing topological phases. Because the presence of pentagon defects breaks the periodicity of the bipartite AB lattice of graphene, it is interesting to explore their influence on well-known and characterized topological trivial phases. The introduction of dopants such as boron (B) may create nontrivial states in AGNR [66], and it can also contribute to modifying the magnetic properties of AGNR [33,88]. We show that doping with B-pairs not only modified the magnetic order in AGNR containing pentagon defects but also improved the stability of the different magnetic phases. Considering that GNRs are generally produced through on-surface synthesis (OSS) bottom-up process [89−92], the metallic substrate used may change the intrinsic electronic and magnetic properties of GNRs. For example, no magnetic behavior was experimentally observed for numerous GNRs containing defects or dopants but where DFT calculations on the freestanding species clearly demonstrate the existence of magnetism [93−95]. Hence, we have considered the influence of a gold substrate on the persistence and magnitude of magnetic characteristics of the GNRs studied.

## 4.2 Computational Methods

To study the localized spin contribution toward the electronic and magnetic properties of the freestanding and Au(111) adsorbed GNRs, we have employed the DFT+U method within the PBE functional limit [96] with the help of the Quantum ESPRESSO package [55,97]. This method was validated in our previous study for the related systems to achieve accurate results close to the experimental findings [98]. Furthermore, our DFT+U method yields a bandgap value for a finite

GNR that is comparable to the traditionally more accurate hybrid PBE0 functional (refer to Table S2 and the Supporting Information (Appendix A)). However, the latter is computationally challenging to use in the presence of a metal surface. Moreover, the DFT+U approach is widely acknowledged as a robust and insightful first-principles technique, especially pertinent to the exploration of strongly correlated electron materials [99]. For gold adsorbed species, we used PBE functional in conjunction with van der Waals corrections derived by Grimme [100], vastly known as the PBE+D2 approach. Ion−electron interactions have been considered using the projector-augmented plane wave (PAW) method [101]. For geometrical optimization, the energy and force convergence thresholds were $10^{-6}$ Ry and $10^{-4}$ Ry/Å, respectively, with a k-point mesh of 9×1×1. In addition, a k-point grid of 24×1×1 was used for band structure and properties calculations where the energy cutoff value of 50 Ry was employed. A vacuum region of 20 Å was used along both z- and y-directions to minimize the interactions between periodic images along that direction. Although for gold adsorbed cases, instead of a vacuum along the y-direction, an extended substrate has been considered along that direction and three layers of gold atoms are introduced along the z-direction to reproduce the 3D nature of Au(111). The Hubbard U parameters were quantified for the C2p orbitals throughout the symmetric atomic sites in the unit cell of the GNRs with the help of the linear-response method [59], and the spin alignment is considered only along the z-axis for the simplicity of this present study. AFM images are obtained using the probe particle model [102], considering the Bader charges derived from our DFT+U calculations.

## 4.3 Results and Discussion

### 4.3.1 Stability of Magnetic Phases in P-GNRs

Figure 4.1a shows the optimized geometry of the 7-AGNR model with pentagon-edge defects, which we simply denote P-GNR. We have identified pentagonal edge carbon atoms as in sublattice A and B as illustrated in Figure S1a in Appendix A. We would like to note here that the synthesis of the corresponding monomers of such pentagon-induced 7-AGNRs can effectively utilize methyl-induced anthracene precursors, a methodology that mirrors successful approaches used in the creation of magnetic sawtooth GNRs [94]. The synthesis trajectory is envisioned to evolve from monomers or oligomers to polymers, characterized by a pentagon edge with $CH_2$. Anticipating a subsequent dehydrogenation step, we expect the emergence of CH entities with unpaired radicals. This expectation is grounded in empirical evidence, as similar results have been documented for

aza-triangulene [103]. This topological non-benzenoid defect in all-benzenoid 7-AGNR systems transmutes the bond formation to establish a non-Kekulé graphene system with an unpaired electron ($S = 1/2$) at each pentagon edge [82]. The separation between the nearest imbalanced spin sites is ∼15.4 Å for the freestanding P-GNR (Figure S1b in Appendix A), and this structure exhibits an antiferromagnetic (AFeM) ground state (see Figure 4.1d). However, when P-GNR is adsorbed on Au(111), a very notable change can be observed in terms of spin ordering; spins flip to become parallel into a triplet configuration and exhibit a ferromagnetic (FeM) behavior (see Figure 4.1e). We believe that the p-type doping nature of the Au(111) substrate provokes the weakening of the spin superexchange interaction between pentagon sites. This leads to exceeding the exchange coupling energy between electrons, and the spins of those last become aligned in the same z-direction.

Except for the pentagon defects, Figure 4.1b shows that the distribution of B-doped pairs among the 7-AGNR backbone is very similar to the system studied experimentally by Kawai *et al* [95]. In contrast to P-GNR, a substitutional doping with B-pairs (P-BGNR) leads to a system that exhibits a FeM ground state in both freestanding and gold adsorbed cases (see Figure 4.1f,g). Although incorporating B-pairs in the GNR does not contribute to modifying the total spin of the system per se, it introduces a point potential at the dopant sites [104]. Such variation of the potential may enhance the net magnetic moment of the system by saturating the $2p_z$ orbitals of C sites in the surroundings of B-pairs. Thus, we observe a higher local spin density throughout the backbone of P-BGNR with respect to P-GNR (see Figure 4.1d,f). The separation between the high-spin-density sites in freestanding P-BGNR is ∼15.6 Å (see Figure S1c in Appendix A), an increase of 0.2 Å compared to P-GNR. This increase may also contribute to the magnitude of the final magnetic moment. On the other hand, owing to the p-doping nature of a gold substrate, its presence contributes to decreasing the local electron spin density among the P-BGNR backbone as observed in Figure 4.1g. A similar phenomenon was previously observed in B-doped GNRs but where the weak magnetic behavior due to point potential of the B-doping sites was totally swapped by the presence of the Au substrate [33,88]. In contrast, we deliberately observed a prominent magnetic moment along the pentagon edges of P-GNR and P-BGNR systems even when adsorbed on an Au(111) substrate. We address the reasons behind the stability of these magnetic pentagon sites in the following sections.

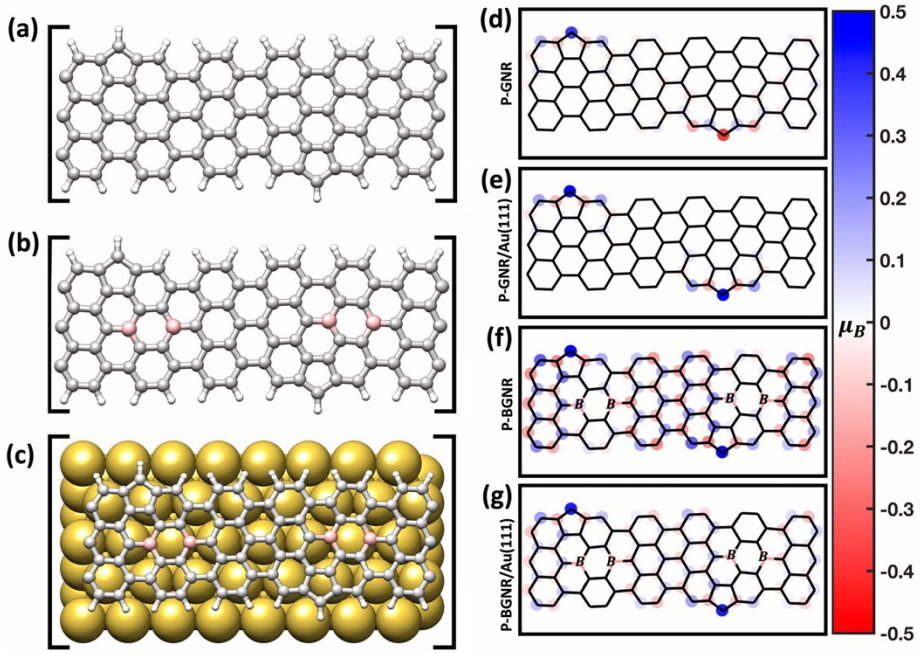


Figure 4.1 Pentagonal topological defect induced magnetic graphene nanoribbons. Chemical structure of the unit cell of (a) all-carbon P-GNR and (b) B-doped P-BGNR. Each pentagon edge contains $S$=1/2. (c) Schematic showing the adsorption of P-BGNR on a Au(111) substrate. A fraction of the Au(111) substrate has been removed for clarity. The total Au(111) model contains 192 atoms over three layers, and the GNR models contain a total of 108 atoms. Ground state local spin-density of (d) freestanding and (e) adsorbed P-GNR and (f) freestanding and (g) adsorbed P-BGNR systems. Large spin density is observed around the pentagon edge, where the topological defects imbalance the Kekulé configurations. The color bar represents the intensity of the local magnetic moment along with the spin alignment along the z-axis (gray atoms: C; white: H; pink: B; yellow: Au).

### 4.3.2 Electronic and Magnetic Properties of P-GNRs

A summary of the electronic and magnetic properties of the P-GNR and P-BGNR systems is reported in Table 4.1. The relative stabilities of DM, FeM, and AFeM phases are given with respect to the ground state of individual unit cells. As discussed above, the relative stability of the magnetic phases indicates that the ground state of freestanding P-GNR is AFeM while it becomes FeM once adsorbed on the Au(111) surface. However, the spin of unpaired electrons in the ground state of P-BGNR remains parallel for both freestanding and gold-adsorbed cases. The band gap energy ($E_g$) for AFeM and FeM phases decreases from P-GNR to P-BNGR for the freestanding structures, and the systems show metallic behavior in their DM phases. A negative Heisenberg spin exchange parameter $J \approx E_{AFeM} - E_{FeM\ (triplet)}$ indicates an AFeM ground state, while a positive value is for a FeM phase. An abrupt change in the sign of $J$ value was observed for P-GNR from freestanding to

adsorbed case, indicating AFeM to FeM transition. A decrease in *J* suggests that the magnetic stability decreases on the Au(111) surface as the electrons are screened by the substrate atoms. This phenomenon also occurs for P-BGNR structures, but the sign of *J* remains positive for both freestanding and adsorbed cases of the triplet configuration of the FeM state. Finally, we used total absolute magnetization ($|m|$) to compare the magnitudes of different local magnetization. The net $|m|$ value drastically decreases for Au-adsorbed cases due to screening by the substrate. On the dopant-induced point potential in P-BGNR increases the net magnetism and the magnetic stability (higher *J* value) compared to the all-carbon P-GNR systems.

Table 4.1 Electronic and Magnetic Properties of Different Freestanding and Adsorbed P-GNRs Calculated at the DFT+U Level[a]

| GNR type | ΔE/unit cell (meV)[b] | | | $E_g$ (meV)[c] | | | *J* (meV) | $\|m\|$ (μB)[d] | Bader charge on GNR (\|e\|) |
|---|---|---|---|---|---|---|---|---|---|
| | | | | AFeM | FeM | | | | |
| | AFeM | FeM | DM | $d_s$[e] | α | β | | | |
| P-GNR | 0 | 60 | 650 | 1.26 | 1.39 | 1.10 | −60 | 6.80 (0.00) | 0.00 |
| P-GNR/Au | 30 | 0 | 340 | 0.75 | 0.98 | - | 30 | 3.90 (1.26) | +0.76 |
| P-BGNR | 360 | 0 | 700 | 0.43 | 0.69 | 0.75 | 360 | 13.46 (2.00) | 0.00 |
| P-BGNR/Au | 50 | 0 | 680 | 1.10 | - | - | 50 | 10.52 (1.87) | +0.43 |
| s-P-GNR | 0 | 160 | 1560 | 1.25 | 1.35 | 0.98 | −53 | 12.30 (0.00) | 0.00 |

a The band gap value $E_g$ is estimated from $|\varepsilon_{HOMO} - \varepsilon_{LUMO}|$.
b Relative energy of AFeM, FeM, and DM phases with respect to the total energy of the ground state (0 eV).
c Semiconducting band gap. Because of the mixture of HOMO and LUMO of GNR with the substrate, the determination of the band gap may be arbitrary; hence we rather used the "–" sign for substrate adsorbed cases.
d Total absolute magnetization per unit cell in their corresponding ground state. Values between parentheses are the actual magnetic moments.
e Band gap values for degenerate bands for both spins in the AFeM phase.

We need to emphasize that magnetic properties (ΔE, *J*, |*m*|) of adsorbed species show that the Au(111) surface does not totally suppress the magnetic behavior of GNRs. This strongly contrasts with the study of Rizzo *et al.* on sawtooth GNR (sGNR), in which the magnetic character of the freestanding sGNR systems was considered completely swapped after an adsorption on Au(111) [94]. The gain of metallicity observed with heat treatment was explained by an increasing electronic coupling between zero mode eigenstates (associated with the unpaired electrons) due to their improved delocalization [94]. Following our DFT+U calculations on similar sGNR, we found in fact that the ground state of the freestanding sGNR is FeM, and its magnetic character persists after the adsorption on Au(111) (see Table S1 in Appendix A). Hence, we believe that the unpaired electrons in pristine sGNRs might rather contribute to the formation of Kondo resonances in the *dI/dV* measurements near zero bias as previously observed on different carbon-based structures [82,103,105]. In this case, the improved electron delocalization induced by heat treatment would attenuate the Kondo effect and improve the metallicity of the sGNR system.

To improve our investigation on the effect of pentagon defects, Table 4.1 also reports the results for a structure that contains symmetric pairs of pentagon defects denoted as s-P-GNR (see Figure S1d in Appendix A). The absolute magnetic moment |*m*| indicates that s-P-GNR has two sets of high-spin atoms in both sublattices A and B in the unit cell and shows the AFeM ground state. However, because the s-P-GNR has a quintet FeM phase with spin $S = 2$ per unit cell, the *J* value was divided by a factor of 3 to avoid double counting [106]. The value of *J* for s-P-GNR is lower than that for P-GNR by 7 meV in its AFeM ground state. In addition to the spin interaction between the pentagon sites of different sublattices (inter-sublattice interactions), we believe there is also some weak interaction between the unpaired electrons from the identical sublattice (intra-sublattice interactions).

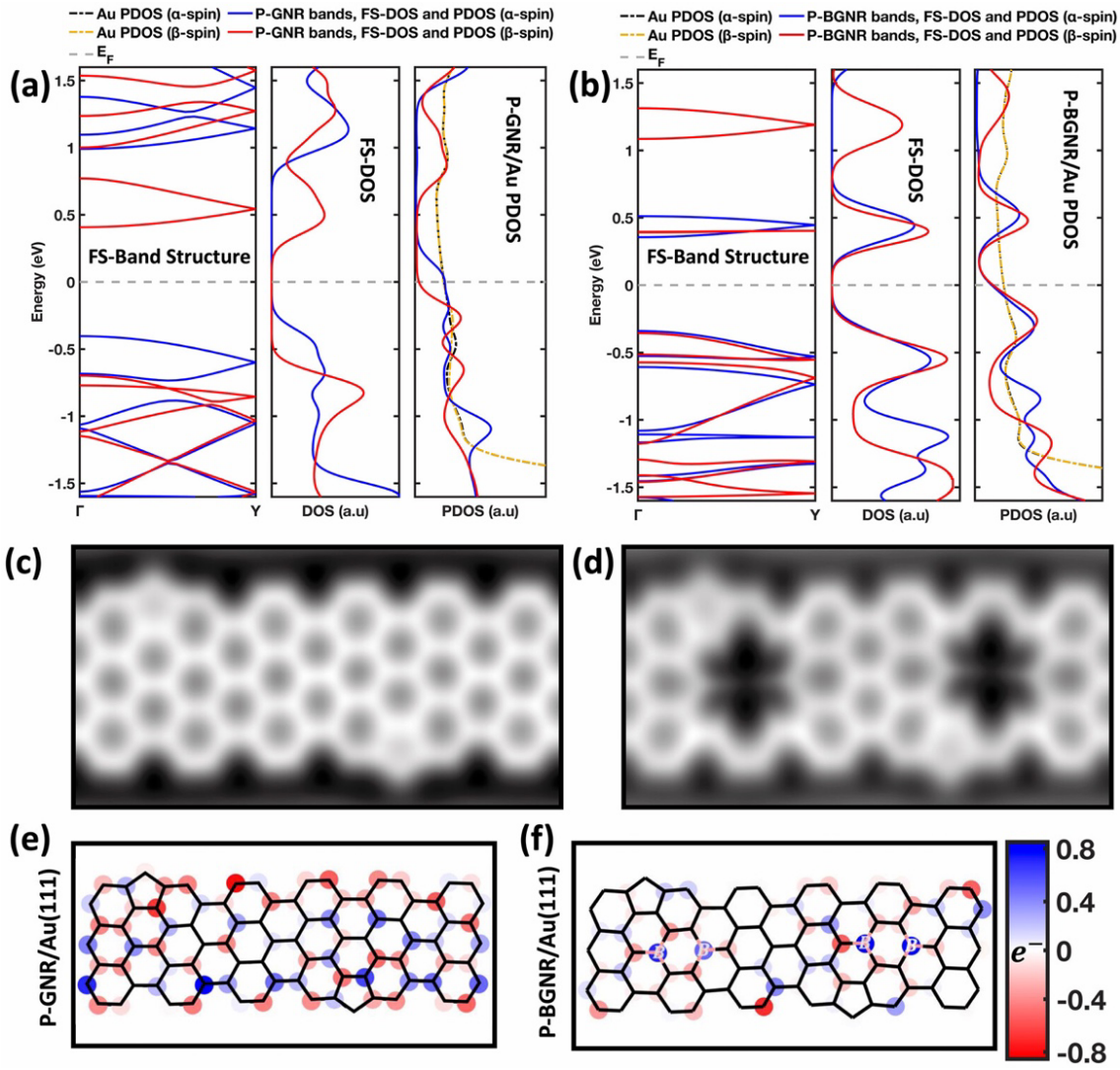


Figure 4.2 Electronic properties of the various chemically stable GNRs. Band structure, DOS, PDOS of freestanding (FS), and adsorbed on Au(111) for (a) P-GNR and (b) P-BGNR. For each GNR, α-spin contribution is specified by the blue color while the red color is used for the β-spin. The Fermi level has been shifted to the zero energy level. PDOS of the on Au(111) GNRs has been upscaled (4×) to show on the same scale as gold PDOS. Simulated AFM images of optimized (c) P-GNR and (d) P-BGNR adsorbed on Au(111). Darker contrast defines the more negative frequency shift compared to the bright one. (e, f) Local electronic charge density showing the charge transfers between the Au(111) substrate and various GNRs. The color bar indicates the charge transfer magnitude and direction where the negative value indicates the electron depletion of GNR. Charge transfer is more prominent on all-carbon (e) P-GNR than the (f) B-doped P-BGNR.

However, this intra-sublattice interactions may introduce opposite local magnetic moment that would reduce the magnetic stability of this s-P-GNR system, although this system has twice more

unpaired electrons than P-GNR. Finally, the band gap in the AFeM ground states remain almost identical in both cases.

### 4.3.3 Electronic Structure of P-GNRs

The electronic structures of the optimized systems are reported in Figure 4.2a,b. Although the ground state of the freestanding P-GNR is AFeM, we compare the band structure and projected density of states (PDOS) of the FeM phase for the sake of simplicity. The electronic structure−properties of the AFeM phases are reported in Figure S2 and the Supporting Information (Appendix A). The band structure of P-GNR shows well-dispersed FeM bands for α (majority) spin and β (minority) spin, below and above the Fermi level, respectively (see Figure 4.2a).

Those bands are degenerate at the Y-point of the Brillouin zone (BZ) in both the valence and conduction band regions for both spins. Such band degeneracy at Y is also observed for the nonmagnetic metallic DM phase of P-GNR (see Figure S2a in Appendix A) as well as for the DM phase of the sGNR system studied by Rizzo *et al* [94]. This also explains the metallic nature of the DM phase (closed-shell structure), where the eigenstates from the non-Kekulé bonded extra electrons cross the Y-point at the Fermi level and are closing the gap [94]. As revealed by the PDOS, the Au(111) substrate shifts the Fermi level toward the valence band of P-GNR, in agreement with a p-type doping of P-GNR. This phenomenon is also observed for P-BGNR, but where the dispersion of HOMO and LUMO bands is lower than for P-GNR. In addition, although P-BGNR has higher magnetization than P-GNR (see Table 4.1), the difference in spin density between α and β bands is much less remarkable in P-BGNR. This can be explained by the facts that (i) the unpaired electrons from the pentagon edge oversaturate the C2pz orbitals around the dopant sites and (ii) the improved quantum interference among electron spin density between point defects of B-dopants.

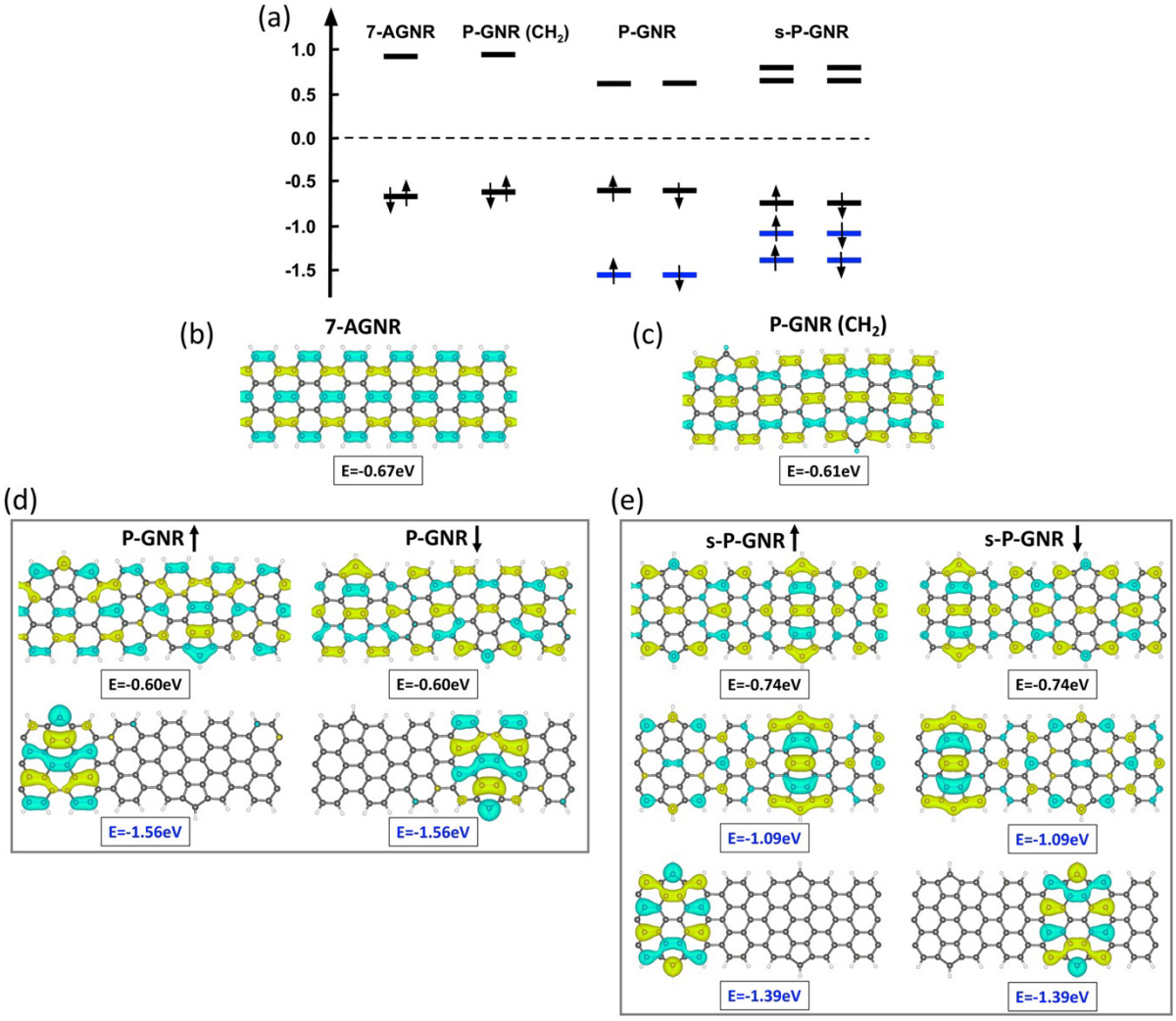


Figure 4.3 Bonding characteristics of various freestanding all-carbon GNRs. (a) MO level diagram of all-carbon-based different GNR species. Only MO levels around the Fermi level are represented. Blue levels are associated with pentagon defects. Wave functions of occupied levels are plotted for (b) defect-free 7-AGNR, (c) 7-GNR with saturated pentagon defects (P-GNR($CH_2$)), (d) 7-AGNR with unsaturated defects (P-GNR), and (e) 7-AGNR with multiple unsaturated defects (s-P-GNR). Magnitude of the isosurfaces = 0.005 $Bohr^{-3/2}$.

In order to validate the geometry used to study the adsorption of P-GNR and P-BGNR on Au(111), as well as the charge transfer calculated from DFT, we used the associated data to simulate the atomic force microscopy (AFM) images shown in Figure 4.2c,d. First, there is an excellent agreement between our simulated AFM images of P-GNR/Au(111) (Figure 4.2c) and P-BGNR/Au(111) (Figure 4.2d) and the experimental images obtained with pristine and B-doped 7-AGNR systems [95,107]. All-carbon structures were found entirely planar on the Au(111) substrate, while our P-BGNR and the B-doped 7-AGNR systems prepared experimentally [95]

show a similar deformation (~40 pm) of B-sites toward the Au(111) surface (see Figure S3 in Appendix A). This structural dip results in the dark contrast features around B-sites in AFM images (Figure 4.2d). The distribution of charges obtained from the Bader analysis that was used to simulate those AFM images is plotted in Figures 2e and 2f for respectively the P-GNR/Au(111) and P-BGNR/Au(111) systems. In these plots, a negative value (red) denotes an electron charge withdrawal while a positive value (blue) denotes the electron charge gain on GNR. The charge distribution along the backbone of P-GNR appears homogeneous, while it is more localized in P-BGNR. Boron pairs are more electroattractive than C atoms and are closer to the substrate; thus, the accumulation of electron charges from Au(111) in that region is more important than the remaining P-BGNR. One important feature in these charge transfer plots is that the pentagon defects hardly contribute to the charge transfer process, reinforcing the persistence of magnetism in those pentagon-induced GNRs.

### 4.3.4 Bonding Character of Pentagon Defects

A more detailed molecular understanding of the role of pentagon defects in the P-GNR systems can be realized by carefully analyzing the evolution of molecular orbitals (MOs) near the Fermi level at the Γ-point of freestanding systems. Figure 4.3 shows the molecular orbital diagrams of frontier orbitals from the defect-free 7-AGNR to the s-P-GNR system that contains two pairs of defects.

P-GNR($CH_2$) has saturated pentagon defects (closed-shell system), and P-GNR contains unsaturated defects (open-shell system). In addition, we show the most representative wavefunction to emphasize the localization aspect of these orbitals. First, we observe that the HOMO level remains in a narrow energy range for all systems. Second, the presence of unsaturated defects brings additional levels at higher binding energy than HOMO, strongly localized near the pentagon defects and mostly responsible for the magnetic behavior of the system. Third, the presence of pentagon defects have a minor effect on the topologically trivial phases ($S = 0$) in the 7-AGNR backbone [66]. A similar trend is observed for open-shell AFeM ground state of P-GNR and s-P-GNR, although the edge states become slightly distorted due to a weak intra-sublattice coupling in s-P-GNR. Hence, although the pentagon sites are the source of magnetism in these systems, they hardly affect the topological phases of the backbone; both characteristics coexist in the open-shell P-GNR systems.

For B-doped GNRs, Cao *et al.* have shown that the substitution of B dopants introduces nontrivial states in the 7-AGNR backbone [66]. The above approach was also used to compare the 7-AGNR with B-pairs (7-BGNR) to P-BGNR-($CH_2$) and P-BGNR (see Figure S5 in Appendix A). For simplicity, we compare the DM states of 7-BGNR and P-BGNR($CH_2$) to the spin degenerated AFeM state of P-BGNR. Indeed, B-pairs induce a nontrivial topological nature along the HOMO of 7-BGNR and P-BGNR($CH_2$) in a similar fashion than reported by Cao and co-workers [66]. Alike P-GNRs, we found strongly localized magnetic states at ∼−0.9 eV that do not interfere with the HOMO level. Such phenomena might open a promising route to achieve magnetic GNRs with trivial and nontrivial topological phases.

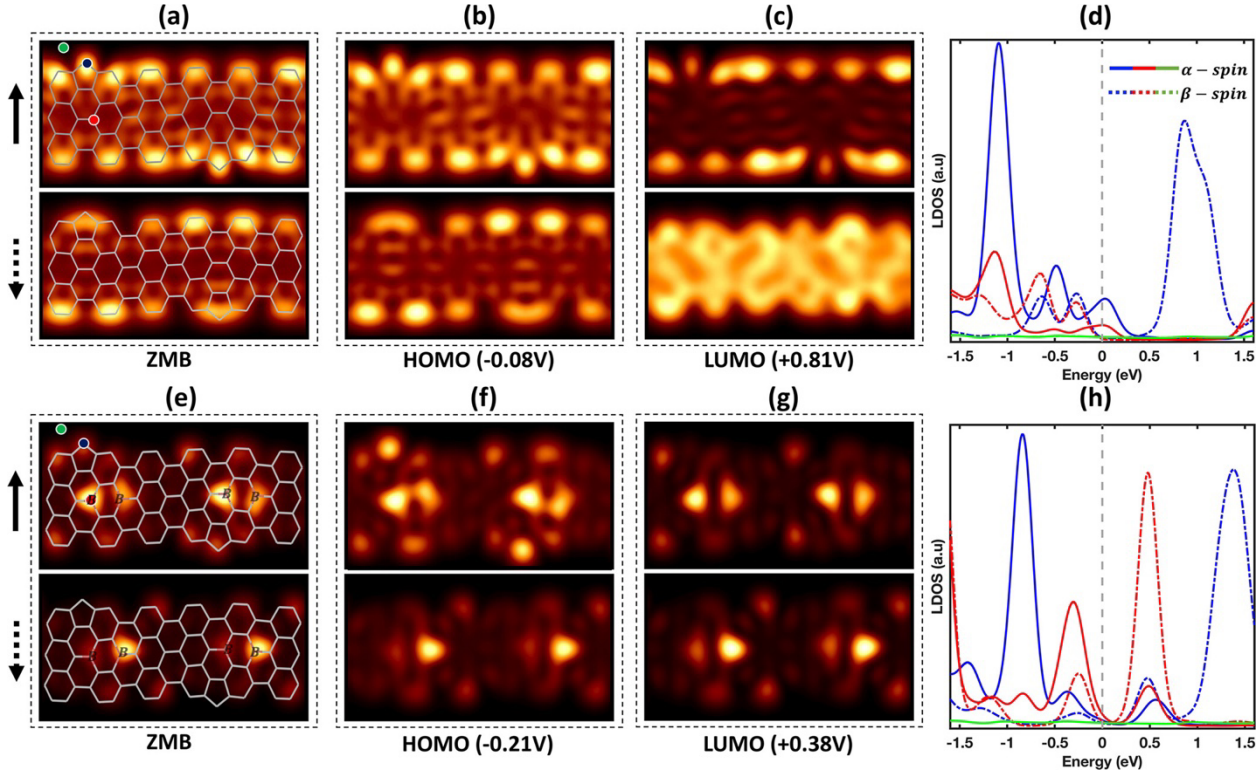


Figure 4.4 LDOS properties of different GNRs adsorbed on a Au(111) substrate. (a–c) LDOS maps of P-GNR/Au(111) at different bias voltages. The corresponding LDOS spectrum is shown in (d), where the different colors correspond to a position identified in (a) with solid dots. (e–g) LDOS maps of P-BGNR/Au(111) and its (h) corresponding LDOS spectrum. Solid lines are for α-spin and dashed lines for β-spin. Wireframe models are placed on top of LDOS maps in (a) and (e) to guide the eyes.

To complete this molecular description, we calculated the spin-polarized local DOS (SP-LDOS) maps as well as the SP-LDOS spectra at different positions on P-GNR/Au(111) and P-BGNR/Au(111) systems. In Figure 4.4, we compare SP-LDOS maps at zero bias (ZMB) to the ones evaluated near the α-HOMO and β-LUMO energy levels. For P-GNR, we observe prominent trivial edge states along the backbone, even at zero bias, very similarly to previous works on related systems [67]. In fact, the maps at zero bias have the same feature of α-HOMO because this last level is very close (−0.08 eV) to the Fermi level. We notice the highly localized character of the pentagon defects for α-spin, while for β-spin, the states are more dispersed. Topological trivial states remain clearly visible near the β-LUMO region for α-spin, but the states become completely dispersed throughout the backbone for β-spin. Furthermore, the intense spectroscopic feature observed at ∼−1.20 eV in Figure 4.4d can clearly be associated with the pentagon defects with α-spin (see Figure S6a in Appendix A), while it appears highly fainted for β-spin. In agreement with previous work [95], no trivial edge states are observed in B-doped systems. This is not surprising because the B-pairs into the 7-AGNR backbone lead to a nontrivial topological nature with localized states near the dopant sites [66]. We observed this phenomenon even at zero bias, although no clear localized states were detected near the pentagon defects (Figure 4.4). However, the α-HOMO (−0.21 eV) shows localized states near the pentagons (see Figure 4.4f), while the β-spin at this bias shows similar features as for ZMB. In addition, the SP-LDOS map calculated at the energy of pentagon defects (∼−0.80 eV) reported in Figure 4.4h is quite similar to the electronic states of the α-HOMO region observed in Figure 4.4f but with slightly higher intensity near pentagon sites. In brief, our SP-LDOS maps revealed that the magnetic behavior of these topologically trivial and nontrivial GNRs is preserved after adsorption on a gold substrate.

## 4.4 Conclusion

In this work, we have shown that the presence of unsaturated pentagon defects introduces magnetism into graphene nanoribbons without affecting the localized topological phases. Substitutional doping with pairs of boron is an interesting approach to improve the stability of the magnetic phases but provokes a reduction of the dispersion of both valence and conduction bands. The presence of a gold substrate has a profound effect on the stability of the magnetic and electronic properties of GNRs. While an Au(111) surface considerably reduces the exchange coupling parameter $J$ of GNRs, the improved magnetic stability of ordered phase in P-GNR is persisting

after adsorption on the substrate. Moreover, although there is always a significant charge transfer from the GNRs to the Au(111) substrate, the strongly localized electrons on the pentagon defects do not significantly contribute to this process.

# CHAPTER 5 ARTICLE 2- CONTROLLING THE MAGNETIC PROPERTIES OF TWO-DIMENSIONAL CARBON-BASED KAGOME POLYMERS

Khalid N. Anindya and Alain Rochefort

Published in Carbon Trends, 7, p.100170, March 27, 2022

*Chapter 5 investigates the magnetic properties of two-dimensional Kagome polymers based on triangulene monomers, addressing the challenge of achieving ferromagnetic FeM phases critical for spintronic applications. Building upon the previous chapter, where defect-engineered approaches in graphene nanoribbons were explored, this chapter extends the focus to organic polymers by utilizing first-principles calculations to demonstrate how doping strategies can tune the magnetic behavior in these systems. The study reveals that while all-carbon triangulene polymers typically exhibit an antiferromagnetic ground state with Mott-insulating behavior, strategic doping with boron or nitrogen atoms can stabilize a ferromagnetic phase with promising electronic properties. The B-rich triangulene polymers show high carrier mobilities, surpassing those of conventional materials like silicon, making them viable candidates for spin-based logic devices, whereas N-rich polymers exhibit half-metallic behavior, offering distinct advantages in quantum storage applications. This chapter not only explores the interplay between symmetry and electronic structure in these systems but also highlights how the careful design of 2D Kagome lattices can lead to the coexistence of robust ferromagnetism and enhanced transport properties. By integrating these findings with the overall thesis objective of advancing magnetic graphene-like systems, this work lays the foundation for future research into tunable, low-dimensional organic magnets suitable for next-generation quantum technologies.*



**Abstract :**

With the help of first principles calculations, we have explored a promising route to control the magnetic properties of two-dimensional organic polymers based on all-carbon triangulene monomers. Similar to small triangulene nanostructures, the Kagome-organized triangulene polymer exhibits an antiferromagnetic ground state, but behaves as a Mott-insulator with relatively poor carrier mobilities. The doping of triangulenes with boron or nitrogen atoms contributes to

switch the ground state of the polymer into a stable ferromagnetic phase, well separated in energy from the antiferromagnetic phase. The existence of a stable ferromagnetic phase is a direct consequence of electron confinement within B/N-rich triangulenes, where the $D_{3h}$ symmetry of the monomers in the Kagome pattern plays a major role on the resulting electronic structure properties. In addition, the two-dimensional Kagome lattice arrangement of B-rich triangulene polymer leads to highly dispersed spin-polarized semiconducting bands and high carrier mobilities that largely exceed known values for pure silicon. In contrast, the ferromagnetic phase of N-rich polymer shows half-metallic behaviour with lower mobilities than B-rich cases. Our results suggest that triangulene-based polymers could be used in diverse sectors from spin-based logic devices to quantum storage applications.

## 5.1 Introduction

Polycyclic conjugated nanostructures such as carbon-based triangulenes have generated a sustained amount of interest over the last decade, and more especially when persisting magnetic properties for adsorbed species were measured [35]. For example, magnetic behaviour for open-shell carbon-derived system adsorbed on Au(111) was observed on six-membered fused-rings triangulene in many forms such as monomer [35], dimer [37] and more recently on a hexamer in a shape of a nanostar [108]. Similar magnetic features were also recently measured on larger triangulenes [36,109,110] and other various triangulene-based nanostructures [38,45,105].

Triangulenes are perfect candidates to form two-dimensional (2D) Kagome polymer (KP) with graphene-like $D_{3h}$ symmetry that leads recognizable electronic features such as Dirac bands, reminiscent of graphene band structure, and flat bands that may lead to anisotropic transport properties [111–113]. Although the creation of a large domain of a 2D magnetic polymer with a surface-assisted synthesis approach constitutes a major challenge, the very recent observation of antiferromagnetism on a triangulene nanostar clearly opens the route for the production of spin-polarized 2D-KP systems [108]. Nonetheless, there are a few synthesis examples where Ullmann coupling was used to produce 2D-KP from heterotriangulenes, species that contain atoms such as oxygen, boron, and nitrogen to create closed-shell building blocks [50,114]. No experimental or theoretical evidence for magnetism was already reported for 2D-KP based on these closed-shell heterotriangulenes, however, the anticipated Dirac and flat band features are present [49,50]. Alternatively, several theoretical works report an antiferromagnetic (AFeM) ground state with

open-shell graphene nanoflakes derived 2D polymers [51,115]; one of them reported fascinating Mott-insulating ground state in heterotriangulene-based polymer [51]. However, to our best knowledge, no ferromagnetic (FeM) ground states were claimed for any triangulenes-based 2D polymers.

In the present work, we used first-principles DFT calculations to study the doping of triangulenes with atomic precision with boron (acceptor) or nitrogen (donor) on the electronic and magnetic properties of conjugated 2D-KP. While we found without too much surprise that the ground state of all-carbon triangulene KP possesses an AFeM phase, DFT+U calculations reveal that ground state of B- and N-rich triangulenes are FeM in nature. The case of B-rich triangulene polymers is particularly interesting since the first excited state is AFeM, located at a practical energy difference (∼100-200 meV) from the FeM ground state, while showing high carrier mobilities in the triplet FeM state.

## 5.2 Computational Details

All monomers forming the 2D-KP are shown in Fig. 19 (a–c), where we denote pure triangulene as Tr and boron (nitrogen)-rich triangulene as Tr3B (Tr3N). The influence of the distance between monomers was investigated by considering a longer diacetylenic linker to form the Kagome polymer while maintaining π-conjugation. The 2D polymers with diacetylenic linker are named Tr-CC, Tr3B-CC, and Tr3N-CC, for all-carbon, B-rich and N-rich polymers, respectively. A representation of the unit cells used in the calculations is given in Figure 5.1 (d–e) for the case of Tr3B and Tr3B-CC polymer. In addition, the presence of unpaired electrons (solid black dot) and holes (hollow black dot), and the corresponding total spin (*S*) for each monomers and repeating units of the polymers (depending on their ground state) are reported for various cases in Figure 5.1 for reference which are analogous to the previous study for different triangulene-based monomers [116].

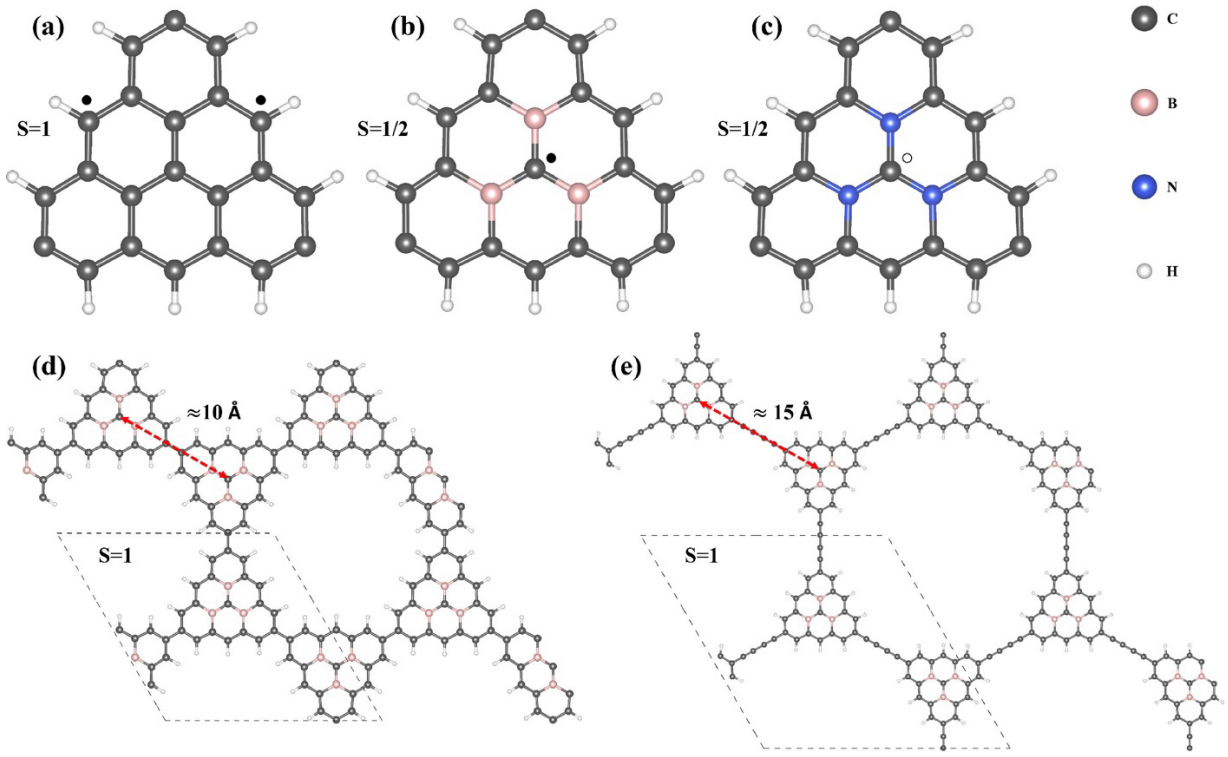


Figure 5.1 Tunable spintronics in triangulene-based polymers. (a-c) Chemical structure of different triangulene-based monomers. Three B or N atoms have replaced the first nearest neighbor atoms of central C atom in (b-c). Unpaired electron sites have been indicated by the solid black dots, while the hollow black dot represent the unpaired hole site in Tr3N (and Tr3N-CC). (d-e) Formation of Kagome lattice: B-rich triangulene polymer with (d) direct C-C bond and (e) diacetylenic linker between monomers. The distance between central C atoms is indicated by a red arrow. Dashed box depicts the repeating units of the polymers. Corresponding total spin (*S*) for the monomers and polymers (spin/unit cell) are provided for reference.

All results are obtained through DFT+U calculations that were performed within the PBE functional limit [96] using the Quantum ESPRESSO package [55,97]. However, to validate the consistency of our numerical findings, we deliberately used three different computational approaches to evaluate the electronic and magnetic properties of the polymers which is explained in the Supplementary Information (SI) section (Appendix B). With a careful selection of Hubbard *U* parameter for C(2p) orbitals, we can improve the localization of open-shell electronic states around Fermi level, and nearly reproduce the experimental values that supports the stable magnetic ground states of similar systems [35,37,108]. We have calculated the repulsion *U* parameter for all symmetric local atomic sites in the unit cell of each polymer by employing the well-established linear-response method introduced by Cococcioni and de Gironcoli [59]. Furthermore, we have only considered out-of-plane spin-alignment along z-direction for simplicity throughout our spin-

polarized calculations. Additional computational details related to optimization cycles and evaluation of electronic and magnetic properties are included in the SI section (Appendix B).

## 5.3 Results and Discussion

### 5.3.1 Magnetic Properties of Kagome Polymers

To emphasize the magnetic properties of the polymers, at first we performed a more global analysis of the spin alignment along the z-direction. We have plotted the magnitude of the local magnetic moments of ground states of the polymers in Figure 5.2, and the corresponding total absolute magnetization per unit cell are reported in Table 5.1. As expected for an AFeM phase, Tr and Tr-CC polymers have opposite spin-densities along each monomer for individual atoms where an inverse mirror symmetry is found in spin-density between the adjacent monomers. Moreover, these local spin-density plots also correspond well to the Ovchinnikov's rule which suggest alternating pattern of spin-alignment along *z*-direction for adjacent atoms in different sub-lattices of spin-polarized graphene-derived systems [24,117]. In addition, the spin-alignment of the neighbouring atoms in the same monomer also corresponds well to the previous study on graphene nanoflakes [105,118]. The presence of a diacetylenic linker in Tr-CC polymer amplifies the total spin-densities where the linker atoms also show alternating spin alignment. In addition, the ferromagnetic ground state phase for B/N-rich polymers shows spin alignment pointing toward a similar direction, and the central C atom remains the main contributor to the total magnetization of the B/N-rich polymers. We want to emphasize here on the mirror symmetry of spin-alignment between the adjacent monomers for these FeM ground states unlike the inverse mirror symmetry for AFeM case in Tr and Tr-CC polymers. In addition, we can clearly see that N-rich polymers have the lowest magnetic moments of the systems investigated, while the all-carbon triangulene has the highest. From these local magnetic signature, we can state that the ferromagnetism in such triangulene based polymers mainly depends on the central atom: how well we can localize the unpaired electrons or holes to that central atom of the monomers using different dopants. In brief, we need to create a symmetric environment where the unpaired carriers cannot overcome their exchange coupling to align in the opposite direction; otherwise, we will observe the AFeM ground phase in these strongly correlated systems similar to previous studies [37,51,108].

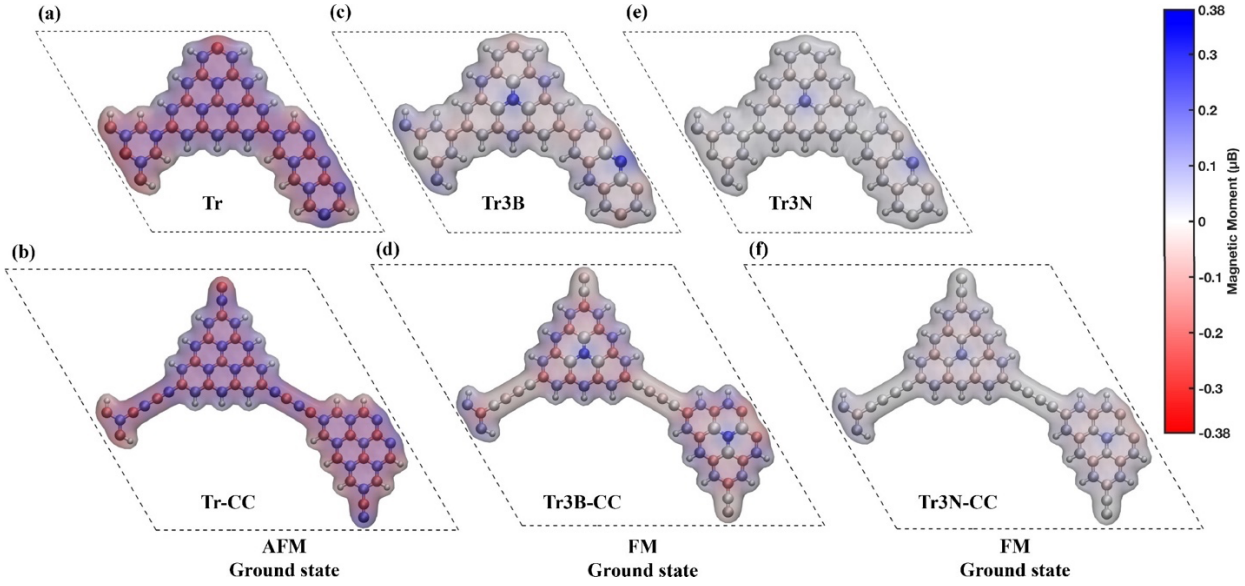


Figure 5.2 Ground state spin-configurations of different polymers. The dashed boxes highlight the repeating unit. The intensity of the local site magnetic moments per atom is represented through the corresponding colors as denoted in the colorbar on the rightmost side. The color gradient underneath the atoms have been induced to achieve a simple graphical understanding of the magnetic signature. (a-b) Ground states of Tr and Tr-CC polymers show an alternating pattern of magnetic signature indicating the AFeM ordering. (c-d) Compared to other sites' magnetic moments, large spin-density is observed for the central carbon atoms in Tr3B and Tr3B-CC polymers which are aligned in the same -direction indicating the FeM ground state. (e-f) Overall magnetic signature of the Tr3N polymer points toward the positive -direction, where the central carbon atoms possess the most spin density, while in Tr3N-CC polymer, the diacetylenic linker exhibit comparatively similar spin density as the central carbon atoms in positive *z*-direction; therefore, both polymers lead to FeM ordering.

A proper overview of the electronic and magnetic properties of the investigated polymers is given in Table 5.1 along with the relative stability of the diamagnetic (DM) and FeM phases with respect to the AFeM phase energy. We are also providing out the band gap values and total absolute magnetization of the polymers studied. Although the total magnetization for AFeM states are zero, for the sake of comparison, we have thus mentioned the absolute value for magnetization. For Tr and Tr-CC, we can clearly state that the AFeM phase is more stable than both DM and FeM phase, and where the FeM phase is the closest excited state. Table 5.1 also reports the Heisenberg spin exchange parameter, $J = E_{AFeM} - E_{FeM\ (triplet)}$ [119]. However, since all-carbon polymers have quintet FeM phase with spin $S = 2$ per unit-cell, we need to divide $\delta E = E_{AFeM} - E_{FeM\ (quintet)}$ by a factor of 3 to get the right value of $J$ [37], which are -0.14 eV and -0.10 eV for Tr and Tr-CC, respectively. For any magnetic material, a negative $J$ value gives the AFeM phase as the ground state, while a

positive *J* value gives the FeM phase as the ground state. Therefore, we see a negative value of *J* for Tr and Tr-CC, and positive values for the B- and N-rich species. Moreover, the band gaps for the ground state of all-carbon triangulene polymers (~2.2 eV) are much higher than the B/N-rich polymers (< 1.0 eV) along with their corresponding total magnetization. This last result is also justified owing to the entire spin configurations; while pure triangulene polymers have a total spin *S*= 2 per unit cell, the B/N-rich polymers have *S*= 1. We observe even more positive *J* values when the diacetylenic linker is present, indicating an increasing ferromagnetism when the distance between open-shell electron/hole sites increases. In addition, B-rich systems possess significantly larger magnetization values than the N-rich systems, this supports that unpaired electrons are better spin carriers than unpaired holes for nanomagnets. However, the band gaps are almost similar for α and β spins of B- and N-rich polymers, respectively.

Table 5.1 Electronic and magnetic properties of different triangulene-based polymers. The band gap value $E_g$ is estimated from $|\varepsilon_{HOMO} - \varepsilon_{LUMO}|$.

| Polymer | ΔE/unit cell (eV)[a] | | | $E_g$ (eV)[b] | | | *J* (eV) | *m* ($\mu_B$)[d] |
|---|---|---|---|---|---|---|---|---|
| | AFeM | FeM | DM | AFeM | FeM | | | |
| | | | | $d_s$[c] | α | β | | |
| Tr | 0.0 | 0.4113 | 1.7117 | 2.13 | 2.15 | 2.13 | -0.1371 | 12.54 |
| Tr-CC | 0.0 | 0.3028 | 2.0271 | 2.18 | 2.03 | 2.09 | -0.1009 | 16.48 |
| Tr3B | 0.0 | -0.1013 | 0.1534 | 0.18 | 0.61 | 0.14 | 0.1013 | 5.92 |
| Tr3B-CC | 0.0 | -0.2269 | 0.1556 | 0.22 | 0.94 | 0.25 | 0.2269 | 10.75 |
| Tr3N | 0.0 | -0.0309 | 0.0005 | - | - | 0.72 | 0.0309 | 2.41 |
| Tr3N-CC | 0.0 | -0.0735 | 0.0009 | - | - | 0.96 | 0.0735 | 4.87 |

[a] Relative energy of FeM and DM phases with respect to total energy of AFeM phase.
[b] Semiconducting band gap. '-' sign is used for metallic feature in corresponding band structures.
[c] Band gap values for degenerate bands for both spins in AFeM phase.
[d] Total absolute magnetization per unit cell in their corresponding ground state.

### 5.3.2 All-Carbon Triangulene Kagome Polymers

We then computed the electronic structure of all-carbon triangulene polymer (Tr) with a simple C-C bond between monomers, the corresponding band structure is shown in Figure 5.3(a). The number of unpaired electrons or the Head-Gordon $N_u$ metrics [120] obtained from the DFT self-consistent simulation over the Tr unit-cell is +4.03, in agreement with the theoretical value of +4.

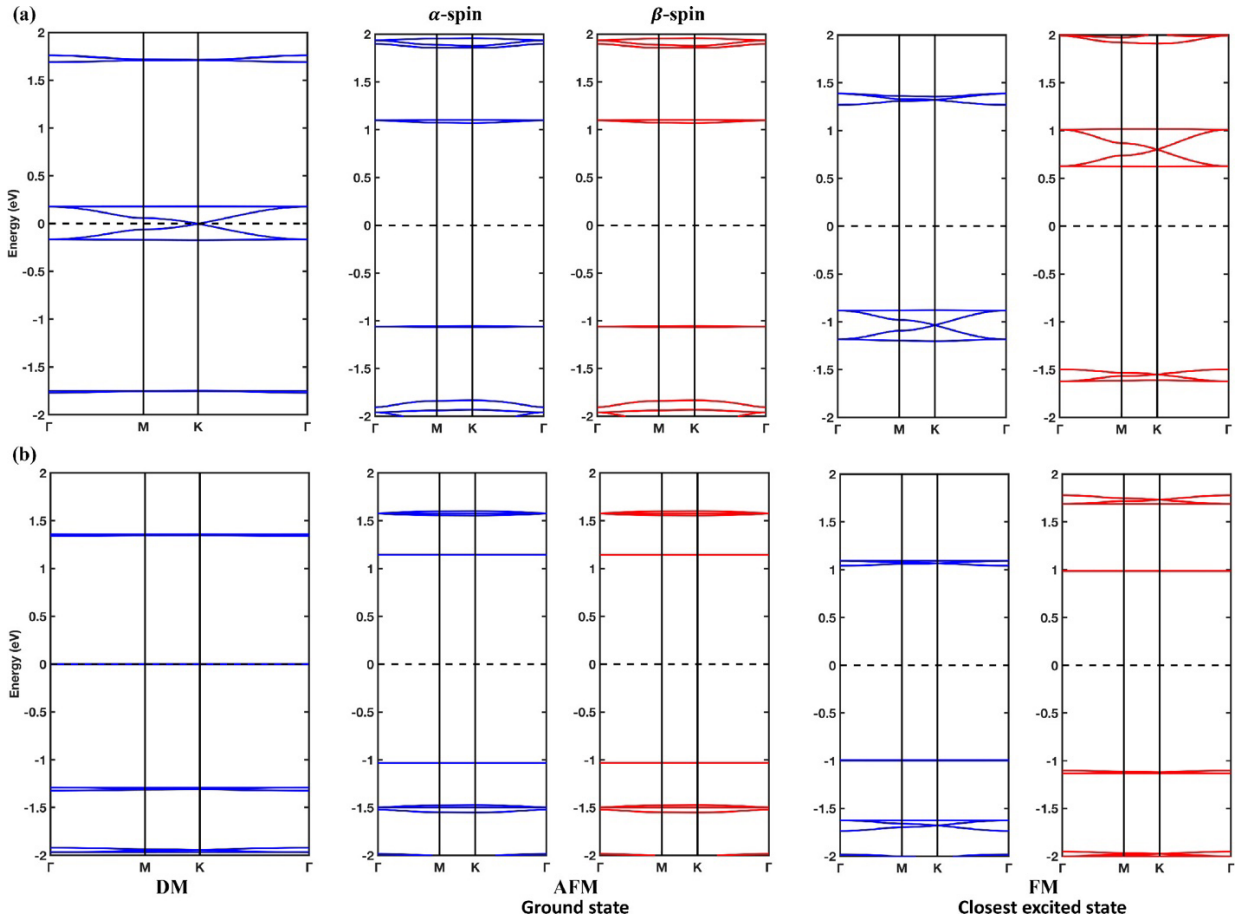


Figure 5.3 Mott-insulating AFeM ground state in all-carbon triangulene polymers. Electronic band structures of different magnetic phases (DM, AFeM and FeM) for (a) Tr and (b) Tr-CC polymers. Dispersion of the bands has been dampened at the presence of the diacetylenic linker. Dirac coupling is completely vanished in DM phase of Tr-CC polymer, where a very tiny band gap opens up along the Fermi level. HOMO-LUMO bands of the AFeM phase have become entirely flat for both spins of Tr-CC polymer, while in the FeM phase, HOMO (LUMO) band maxima (minima) are present at the Γ-point of the BZ with a narrow dispersion along the *K*-point.

We deliberately used the positive value for $N_u$ to present the excess unpaired electrons while a negative value of $N_u$ corresponds to the surplus equivalent holes in the system. Owing to the presence of 4 unpaired electrons per unit-cell of the all-carbon polymers (while the Tr monomer is FeM [35]), spin density along the *z*-direction could be very anisotropic. Moreover, the separation between the FeM type monomers with spin $S = 1$ in these 2D-KP pattern are not much which helps to overcome the exchange-coupling energy, leading to an AFeM ground state for the all-carbon polymers (see Table 5.1). Moreover, a previous study [121] demonstrated that Mott-insulating AFeM phase depends mainly on the $U/t$ ratio, where $U$ is the Hubbard parameter associated to

Coulomb repulsion between two open-shell electrons aligned in the opposite direction and *t* is the electronic coupling between the nearest neighbouring electrons with the same spin. We have estimated *U* and *t* values with a similar approach previously used by Thomas *et al.* for related systems [51]. A value for $U = 2.21$ eV was calculated for the all-carbon 2D-KP, where *t* is the width of the top valence band of the FeM state (the Dirac bandwidth for the α-spin of corresponding polymers), and $U = 2.20$ eV is estimated from the band gap of the AFeM phase (Coulomb gap) at the *K*-point of the Brillouin zone (BZ). Therefore, $U/t = 42.6 / 4.3$ indicates a stable Mott-insulating AFeM ground state [121].

To clarify the electron coupling in different states and to compare them with previous studies [49], [51], we have evaluated the band structures of DM, AFeM, and FeM phases. Owing to the $sp^2$ hybridization nature between the central carbon atoms of the triangulene based 2D-KP retaining $D_{3h}$ symmetry [49], the DM phase shows weakly dispersed Dirac bands around the Fermi level sandwiched by two flat bands that might arise from the unpaired electrons. We want to stress that the semi-metallic nature of this DM phase highly depends on the symmetric nature in the 2D-KP that is similar to the $D_{3h}$ symmetry of graphene, and thus, this semi-metallic feature can be easily changed by breaking this symmetry among the unit cell [122]. The calculated Dirac bandwidth is only 0.34 eV as compared to ∼23 eV for graphene; the Dirac dispersion of Tr is nearly two orders of magnitude less than a pristine graphene sheet. This large dispersion drop is directly linked to the porosity of triangulene based 2D-KP system in which a significant charge localization near edges is observed [115,116]. For the Mott-insulating AFeM phase (see middle panels in Figure 5.3(a)), degenerate bands are observed for both spins with a direct band gap at the *K*-point of the BZ, in agreement a previous study on related systems [51]. While we acknowledge that pure triangulene would be per se a quite reactive precursor to form a polymer, excellent Mott-insulating magnetic properties can be observed for Tr polymer without using any longer linkers between monomers as previously proposed [51]. Finally, we observe a lifting of the spin degeneracy of the bands around the Fermi level as predicted for the FeM phase, along with a band gap opening at the Γ-point of the BZ. This FeM phase for the Tr polymer contains Dirac band features that suggest much better spin transport properties among the α-HOMO and β-LUMO bands than in their opposite spin bands, β-HOMO and α-LUMO for which the band dispersion is lower.

The influence of the distance between open-shell electrons within individual monomers on the magnetic and electronic properties of the polymer was investigated by placing a diacetylenic linker

(Tr-CC) which is a conjugated carbon chain with two triple bonds between monomers. Based on previous studies on related systems [49,51], such longer linker should further decrease the Dirac bandwidth and leads to improve the confinement of electronic states from the open-shell orbitals. The band structures of the different magnetic phases of Tr-CC are illustrated in Figure 5.3(b). We can clearly observe an increasing localization of the states around the Fermi level. For the DM phase, the Dirac coupling has virtually vanished, a direct consequence of an improved localization of unpaired electrons on monomers in the system. For Tr-CC polymer, we again found Mott-insulating AFeM phase as the ground state for which a considerable value of $U/t$ = 1555.07 is estimated. Here, we note a significant decrease of the t value (= 0.0014 eV) that is also related to the loss of Dirac coupling in the DM phase. However, the $U$ value remains approximately identical (2.21 eV from AFeM phase band gap as described previously), which is justified for a polymeric system made of identical monomers with an exact number of open-shell electrons showing similar AFeM phase. Although the presence of that diacetylenic linker weakens the electronic coupling, it helps to enhance the total absolute magnetic moment of the system (see Table 5.1). This result is related to the more localized electronic orbitals and to the loss of electron-electron interaction between open-shell sites. For the FeM phase, LUMO and HOMO bands contain very narrow Dirac features for α- and β-spin, respectively, with a band gap (∼2 eV) at the Γ-point of the BZ.

To complete our analysis of all-carbon triangulene systems, we have evaluated the $U$ and $J$ value for an isolated triangulene dimer (see Fig. S1, SI in Appendix B) with DFT+U approach. We found $U$ = 2.0 eV and $J$ = -46 meV that are close to the experimental values ($U$ = 1.65 eV, $J$ = -14 meV) reported by Mishra *et al.* for a triangulene dimer on a Au(111) substrate [37]. Our slightly larger calculated values are reasonable since the Au(111) substrate was not considered in our calculations. The calculated values for the spin exchange parameter and the Coulomb gap for the AFeM phase may be screened by the presence of a metal substrate, which would finally lead to a decrease in the energy values with respect to the freestanding case. Moreover, our Tr polymer shows significantly larger $J$ parameter than the triangulene dimer owing to the strong collective magnetism in periodic 2D system with respect to the 0D counterpart. A similar argument can be used to compare other related studies where $J$ is slightly larger for a triangulene nanostar [108] than for a dimer [37]. Furthermore, a more careful comparison between Tr and Tr-CC polymer clearly indicates that Tr has higher negative $J$ value than Tr-CC (see Table 5.1). The diacetylenic linker is responsible for this lower $J$ parameter which also supports the experimental findings by Mishra *et al.* where the

presence of phenylene spacer between triangulene monomers contributes to decrease the value of $J$ [37]. In summary, according to the Mott-insulating (AFeM) ground state nature of all-carbon Tr and Tr-CC polymers, such material could be promising for spin-based memory devices and optical switches [123] but would poorly perform in transistor applications.

### 5.3.3 Dopant-Rich Triangulene Kagome Polymers

Due to low dispersive HOMO and LUMO bands in the ground state AFeM phase and the closest excited FeM phase, all-carbon triangulene polymers do not appear suitable candidates for spin-based logic devices in which good transport properties are required along with proper spin-polarized semiconducting properties. When triangulene monomer is doped with three boron (B) or nitrogen (N) atoms as shown in Figure 5.1(b-c), this first reduces the number of unpaired electrons. In fact, the theoretical total spin of both B/N-rich triangulene is 1 per unit cell; where Tr3B monomer has one unpaired electron while Tr3N monomer has one unpaired hole. The calculated $N_u$ values/unit-cell, +2.09 and -1.85 for Tr3B and Tr3N, respectively, agree with the p-type doping in Tr3B (theoretical $N_u \approx +2$ for two unpaired electrons) and n-type doping in Tr3N (theoretical $N_u \approx -2$ for two unpaired holes). In contrast to Tr (and Tr-CC), we found that both Tr3B and Tr3N polymers exhibit a triplet ground state; more specifically, it gives a very stable FeM phase (see Table 5.1) with a reasonably good dispersion for either spin. The symmetric arrangement of the dopants around the central carbon atom allows the monomer to maintain its $D_{3h}$ symmetry, which is beneficial to form a mesoscale-sized 2D polymeric system where the wavefunctions can possess symmetric nature throughout the system. Moreover, breaking the symmetry between the nearest neighbor monomers, the dispersion of the HOMO-LUMO bands can also be dampened [122].

The band structures for different Tr3B and Tr3B-CC phases are reported in Figure 5.4(a) and (b), respectively. The bands for the DM phase of Tr3B show a metallic nature, which also justifies the existing magnetic ground state owing to the fact that these symmetric superlattice formed 2D-KP systems contain zero-mode states with localized unpaired electrons. We notice the absence of the Dirac feature indicating the loss of $sp^2$-coupling between the central carbon atoms surrounded by three B atoms. When the 1st nearest neighbors of the central carbon sites are doped with B (N), they confine the unpaired electron (hole) to that central site of the monomer with strongly localized states and thus they cannot form graphene-like $sp^2$-coupling, unlike the previous study [49]. The band structure of the AFeM phase of Tr3B is quite contrasting with the Tr polymer previously

described. The HOMO bands of Tr3B shows a comparatively better dispersion, and the band gap is smaller than for the AFeM phase of the Tr polymer. Nonetheless, the wider dispersion of the HOMO bands of the AFeM phase indicate a disordered spin-liquid phase [121], which is not predictable to be the ground state for this periodic 2D-KP retaining $D_{3h}$ symmetry.

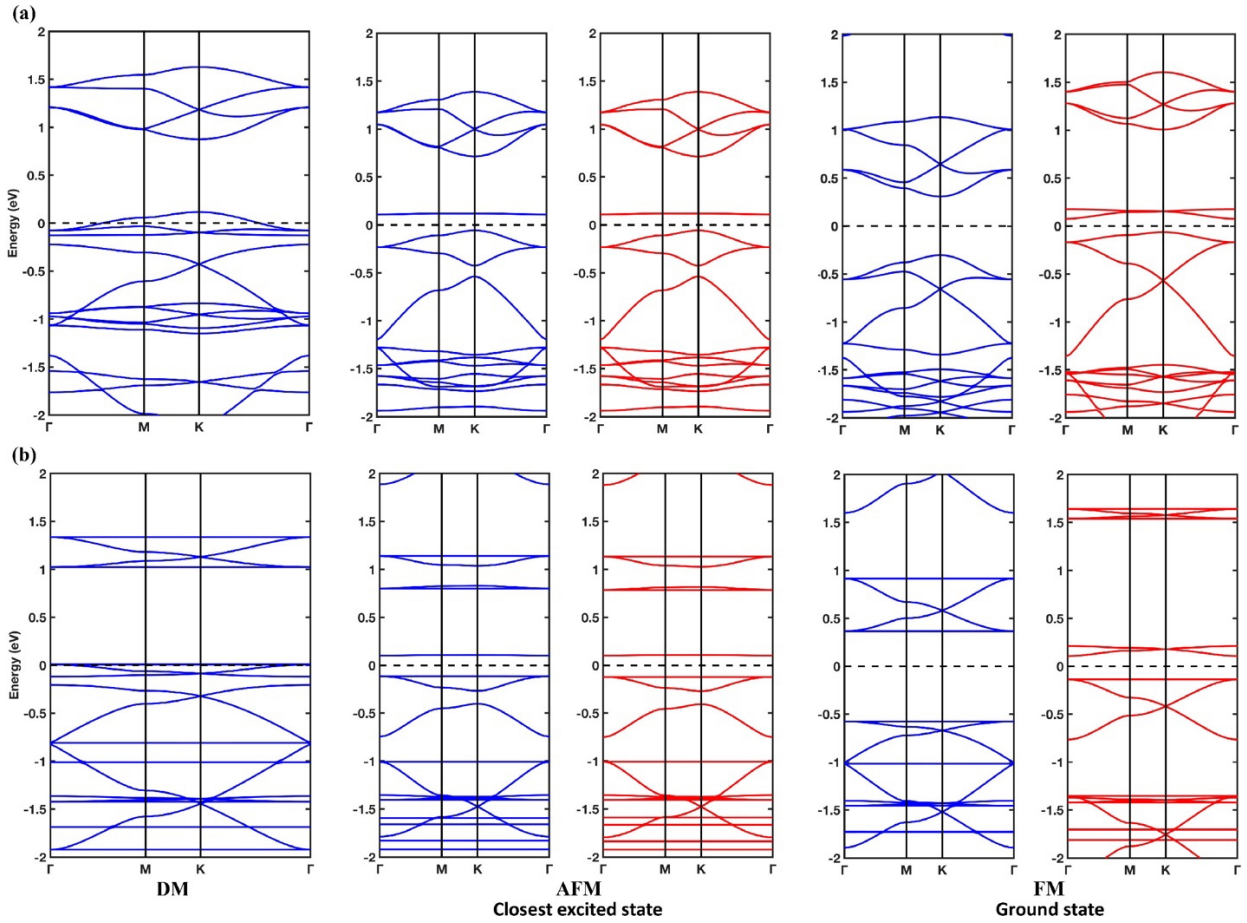


Figure 5.4 FeM ground state in B-rich triangulene polymers where unpaired electron carriers exist around the central carbon atoms. Electronic band structures of DM, AFeM and FeM phases for (a) Tr3B and (b) Tr3B-CC polymers. Both polymers show metallic feature in the DM phase, while the triplet ground state shows very good dispersion, specially for α-spin HOMO-LUMO bands for direct C-C linker based system. Moreover, the AFeM phase HOMO also retains comparatively good dispersion in Tr3B polymer. In contrast, longer spacer between the central carbon atoms leads to smaller dispersion in Tr3B-CC polymer.

The aforementioned phenomena observed for DM and AFeM phases indicate that the ground state magnetism could be mainly linked to the FeM phase, although the AFeM phase is the closest excited state. Concerning the bands of the ground state FeM phase of Tr3B, α-spin shows a direct band gap at the Γ-point of the BZ with reasonably good dispersion for HOMO and LUMO bands.

On the other hand, β-spin has a comparatively narrower indirect band gap where the minima of the LUMO is located at Γ-point, and the maxima of the HOMO is centered at the K-point of the BZ.

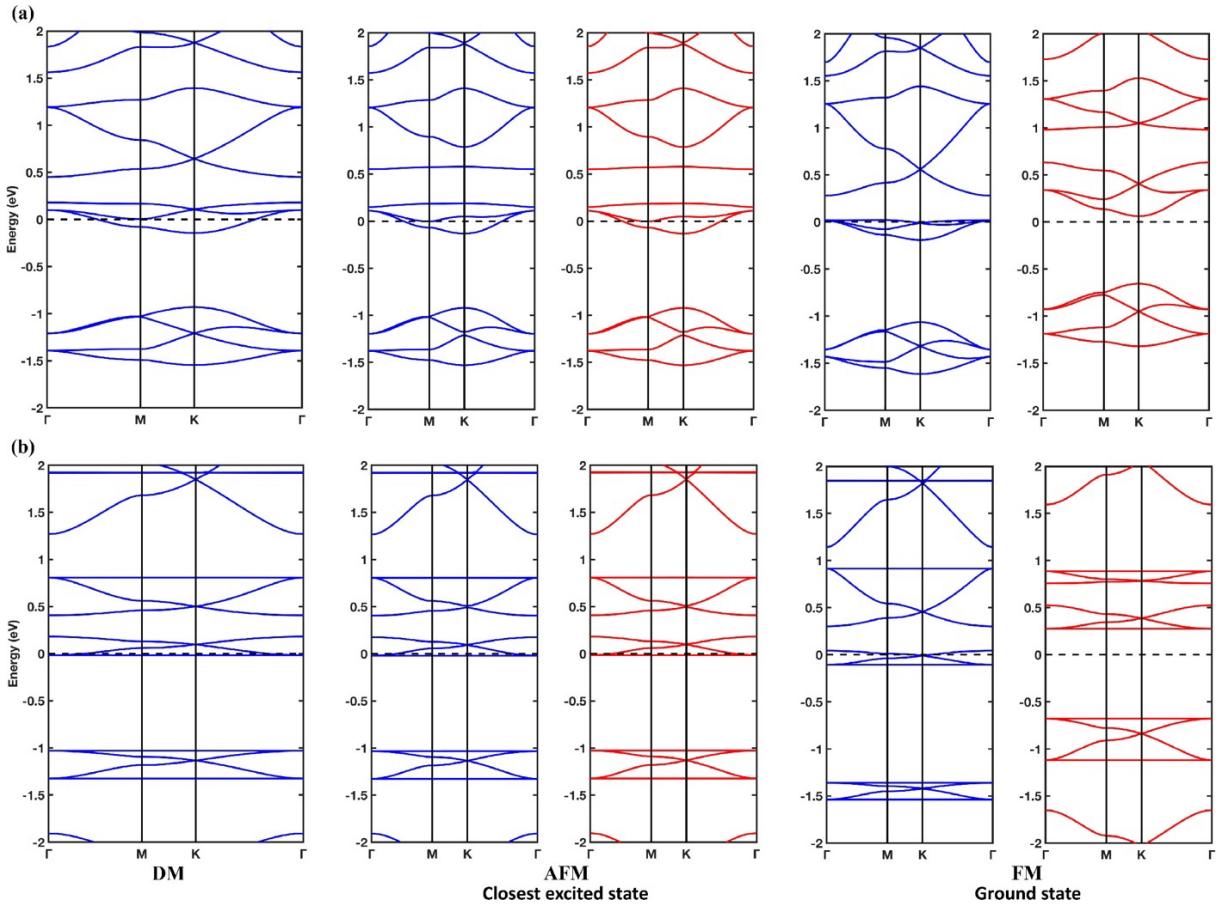


Figure 5.5 FeM ground state in N-rich triangulene based polymers where unpaired hole carriers exist around the central carbon atoms. Electronic band structures of DM, AFeM and FeM phases for (a) Tr3N and (b) Tr3N-CC polymers. Both polymers show metallic feature in the DM and AFeM phases. Besides, α-spin of the triplet ground state in Tr3N retains three zero-mode bands crossing the Fermi level indicating metallic nature, while in Tr3N-CC polymer, a well defined Dirac feature is observed for the same spin. In contrast, β-spin exhibit reasonably good dispersion in Tr3N polymer, which is flattened out at the presence of a longer spacer in the Tr3N-CC polymer.

The presence of the diacetylenic linker in the polymer (Tr3B-CC) leads to similar consequences as previously described for the Tr-CC polymer; the bands around the Fermi level are more strongly localized and less dispersed than the Tr3B case. Nevertheless, the total absolute magnetization of Tr3B-CC is significantly larger than Tr3B (see Table 5.1). The bands around Fermi level for DM and AFeM phases are nearly flat (see Figure 5.4(b)), but the DM phase retains the metallic feature and the AFeM phase shows a small band gap. For the FeM ground state, α-spin shows a similar

band gap as the Tr3B polymer, although the band dispersion around the Fermi level has practically disappeared, indicating an improved localization of unpaired electrons due to the longer distance to overcome the exchange coupling. In addition, although the β-spin retains its Dirac feature as the LUMO band of Tr3B, while the HOMO band becomes completely flat unlike the case of Tr3B.

The band structures of the N-rich systems are reported in Figure 5.5(a) and (b) for Tr3N and Tr3N-CC, respectively. The DM phase of Tr3N possesses a similar metallic feature (see Figure 5.5(a)) with some dispersed bands around Fermi level as the Tr3B polymer. Surprisingly, the AFeM phase also shows a dominant metallic feature with degenerate bands for both spins. This behavior sounds reasonable since Tr3N monomer contains more electrons due to their n-type doping that shifts the Fermi level towards the conduction band region and gives rise to an unpaired hole. Furthermore, the FeM ground state of Tr3N polymer boasts a half-metallic feature for α-spin, while β-spin shows a direct band gap at the K-point with a reasonable amount of dispersion. Nonetheless, the Fermi level has been further shifted towards the conduction band region than the α-spin bands of Tr3B polymer. This similar nature of the ground state FeM bands for the opposite spins of Tr3B and Tr3N also justifies that the magnetism comes from two different types of carriers, either electrons or holes, respectively. In contrast, the DM bands of Tr3N-CC polymer also contain metallic features with highly localized flat bands near Fermi level, which is also true for the AFeM phases (see Figure 5.5(b)). The FeM phase retains a narrow Dirac feature around the Fermi level in its α-spin. In contrast, the β-spin has a band gap with two complete flat bands on either side of the Fermi level, as described previously for the α-spin of Tr3B-CC polymer.

### 5.3.4 Nature of Frontier Orbitals in Triangulene-Based Kagome Polymers

The nature of HOMO, LUMO, and the zero-mode orbital (ZMO) around the Fermi level can be described with the help of charge density distribution. Here, we considered ZMOs as the corresponding bands that cross the Fermi level, except the Dirac-like bands (see Fig. S2 in SI (Appendix B) for more detailed description). For simplicity, Figure 5.6 reports a representation of the charge distribution only for the magnetic ground states of Tr (AFeM), Tr3B (FeM) and Tr3N (FeM) polymers at the Γ-point of the BZ. For Tr polymer (Figure 5.6(a)), the ground state is a Mott-insulating AFeM phase with highly localized charge distribution on monomer of opposite spins, leading to weakly dispersed bands. More precisely, for a given orbital (either HOMO or LUMO) the charges are localized on different monomers for each spins. Moreover, the charge is

distributed mostly at the edges of monomer while retaining a symmetric nature along each monomer, in agreement with the presence of two unpaired electrons near the triangulene monomer edge [35,116]. A similar description can be used for the ground state (AFeM) of Tr-CC (see Fig. S3(b), SI (Appendix B)) although the charge localization is even stronger due to the decreasing exchange coupling between the unpaired electrons separated by a larger distance. The charge distribution of the excited states (DM, FeM) of Tr and Tr-CC polymers are reported in Fig. S3 of SI in Appendix B.

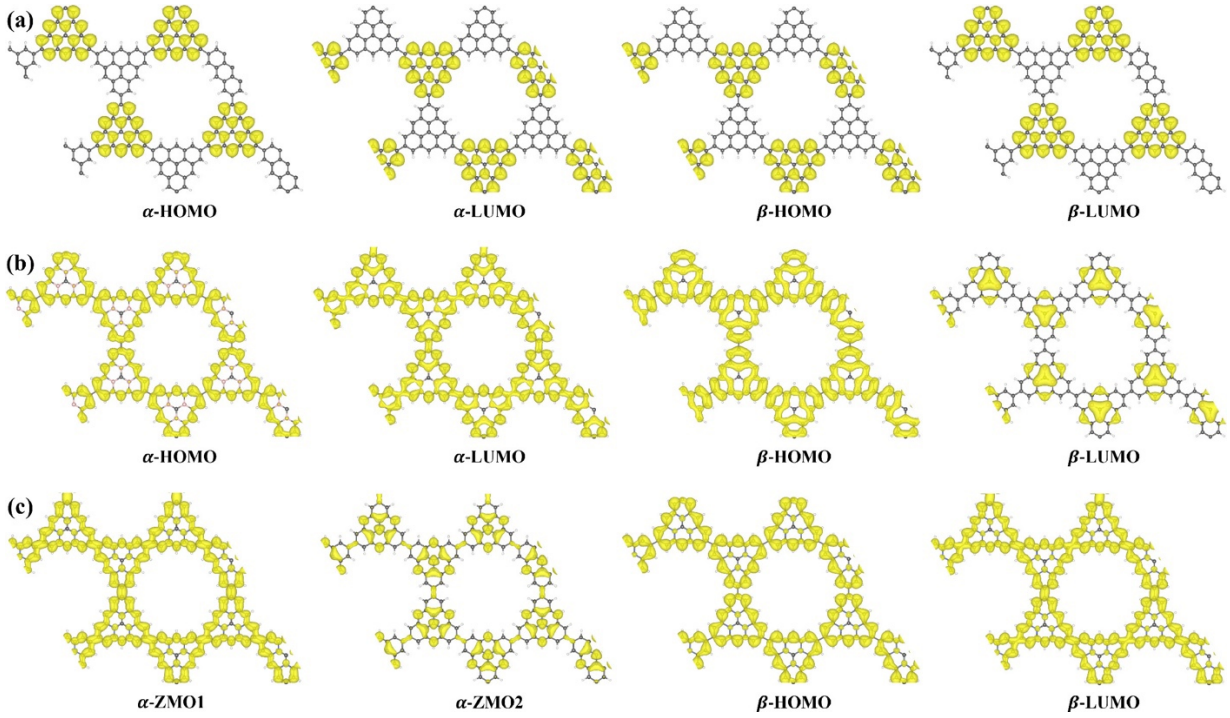


Figure 5.6 Charge density distribution (at the Γ-point of the BZ) in molecular orbitals around the Fermi level for ground state magnetic phases of polymers with direct C-C linkers. The corresponding orbitals have been indicated on the figure. Charge densities for two-fold degenerate bands at the Γ-point of the BZ have been summed up. Isosurface has been set to 0.0005 e/Å$^3$ for the illustration. (a) Mott-insulating AFeM phase in Tr polymer shows strongly localized HOMO-LUMOs for either spins. Exceptional delocalization of charge has been observed in (b) Tr3B and (c) Tr3N for both spins in their FeM ground states, except for the β-LUMO (FeM phase) of Tr3B polymer where charge is mostly localized around the central parts of each consisting monomers where the unpaired electrons exist. α-ZMO1 (the uppermost ZMO) of Tr3N is mostly delocalized around the central atom and the dopant sites, while α-ZMO2 (the nearest one to the ZMO1) is delocalized mostly around the edges of Tr3N.

The spin-polarized semiconducting nature of the ground state FeM phase for Tr3B demonstrates some interesting charge density distribution of HOMO and LUMO bands, and where the

localization phenomenon becomes amplified for Tr3B-CC due to larger distance between monomers. The charge density is well delocalized among the α-spin for HOMO and LUMO, which suggest its good transport properties, while the β-spin has some different charge distribution. The β-LUMO has a localized charge distribution just around the central carbon atoms but in all monomers of the system, this gives rise to the weakly dispersed β-LUMO band observed in Figure 5.4 for the FeM phase. The charge distribution obtained for the FeM phase of Tr3B-CC (see Fig.S4(b), SI in Appendix B) help to reveal the real nature of those bands, which show similar type of charge distribution along the B-rich triangulene monomers. Moreover, charge distribution was also observed along the diacetylenic linkers except for the β-LUMO of Tr3B-CC for FeM phase. Highly localized charge distribution was observed in the β-LUMO of Tr3B-CC. The charge density distribution of Tr3N for the near Fermi bands also appears quite delocalized over the entire polymer. According to the n-type doping character of the system, α-spin shows metallic feature, while β-spin has an n-type semiconducting band gap. The charge distribution in Tr3N-CC polymer follows its Tr3N counterpart along the monomers, although charge was also well-distributed along the diacetylenic linkers. Moreover, the β-LUMO and β-HOMO forms a Dirac cone at the Γ-point of the BZ (see Fig. S5(b), SI in Appendix B) owing to the long range graphene like sp2-hybridization through the diacetylenic linkers between the monomers. The metallic nature of this Dirac band exhibits a well-delocalized charge distribution throughout the polymer. Although all the phases may have topological edge distribution coming from the near Fermi flat bands which are non-degenerate at the Γ- and *K*-points of the BZ, depending on the spins and orbitals, the direction of the topological edge states can vary. The existence of such topological states that run in different directions among the 2D-KP was previously observed on polymers built from BN-based triangular doped-monomer [98]. Hence, as far as those topological states are delocalized over the entire polymer, this could lead to a strong anisotropy in charge transport among the spin-states, and even allow room-temperature superconducting phenomena.

### 5.3.5 Transport Properties of Kagome Polymers

To conclude this study on nanomagnetic materials based on triangulene, we have also quantified the mobility of the different carriers of the different spins for FeM phases of the polymers connected by direct C-C bonds (see Table 5.2). To estimate the carrier mobilities, we have used an approach that was successfully applied by us and others on related systems [49,98]. Although pure triangulene polymers have AFeM ground state with Mott-insulating phase, we have considered

their closest excited FeM phase carrier mobilities for simplicity in comparison. We have not considered the mobility for the polymers with diacetylenic linkers owing to their comparatively lower band dispersions. Overall, due to the narrower dispersion of the HOMO-LUMO bands of Tr polymer, very low carrier mobility is obtained for both carriers (electrons (e) and holes (h)). Moreover, electron and hole mobility of the α and β-spin tends to zero, respectively, for which the complete flat bands are responsible. As discussed previously, B and N doping can improve the carrier mobility of these related systems and can thus help to implement these materials in spin-based logic devices. We observed almost three times hole carrier mobility than silicon in the α-spin of Tr3B polymer, while the β-spin has almost similar hole carrier mobility than silicon. On the other hand, N doping can also improve the carrier mobility. We have estimated the carrier mobility for just the α-spin of Tr3N, which has semiconducting nature, unlike the β-spin that possesses the metallic feature. As observed from Table 5.2, Tr3N polymer can also offer reasonable spin-polarized carrier transport capability in its α-spin. Moreover, we have observed almost similar value of elastic modulus, χ, as previous study on related systems [49], which further justifies our DFT+U approach to study the electronic and magnetic properties of these advanced 2D nanomaterials.

Table 5.2 Calculated effective masses ($m^*$) and mobilities (μ) for different charge carriers of the FeM phase of the direct C-C bonded polymers under investigation. Deformed potential (ζ) and elastic modulus (χ) have also been tabulated for reference.

| Polymer | Carrier | Spin | $m^*$ ($m_0$) | $S^a$ (eV) | $\chi^a$ (N/m) | μ ($cm^2V^{-1}s^{-1}$) |
|---|---|---|---|---|---|---|
| Tr | e | α | 13.61 | 3.34 | 39.16 | 0.27 |
| | h | | 2.72 | 4.40 | | 3.88 |
| | e | β | 3.40 | 0.50 | | 192.26 |
| | h | | ∞ | 1.24 | | ≈0.00 |
| Tr3B | e | α | 0.36 | 5.24 | 64.50 | 260.21 |
| | h | | 0.33 | 1.72 | | 2808.12 |
| | e | β | 0.85 | 7.20 | | 24.45 |
| | h | | 0.97 | 1.16 | | 720.28 |
| Tr3N | e | β | 0.39 | 7.50 | 93.39 | 155.77 |
| | h | | 0.32 | 4.88 | | 530.36 |

[a] ζ and χ parameters are taken from the average value for various compressive and tensile strains in either 2D direction.

## 5.4 Conclusion

To summarize, we have described with the help of first-principles DFT calculations, a promising route to tune the magnetic properties of 2D Kagome polymer with triangulene-based species by introducing atomic dopants. Although all-carbon triangulene polymers show good magnetic properties, they do not appear suitable for spin-polarized transport applications owing to their Mott-insulating ground state. In contrast, 2D-KP from B- and N-rich triangulene can retain good dispersion in their HOMO-LUMO bands for both spins. More especially α-spin of both systems are very interesting; while Tr3B shows the largest carrier mobility in its α-spin, Tr3N retains a metallic feature for the same spin. Moreover, we have demonstrated the great importance of symmetry in these 2D-KP nanomagnets; breaking the symmetry can dramatically dampen the band dispersion. We have highlighted a way to increase the total magnetic moments by including long spacer between monomers, although this can degrade the carrier mobilities. Based on the flexibility to tune the magnetic properties of all-organic 2D-KP, this work could stimulate further effort to fabricate next-generation organic spin-based logic devices. In addition, the presence of direct bandgap in Mott-insulating ground state of pure triangulenes and in the triplet ground states of the B/N-rich triangulenes may lead to possible applications in quantum optical switches.

# CHAPTER 6 ARTICLE 3- COLLECTIVE MAGNETISM IN 2D POLYMER MADE OF C-DOPED TRIANGULAR BORON NITRIDE NANOFLAKES

Khalid N. Anindya and Alain Rochefort

Published in Advanced Theory and Simulations, 4(5), p.2100028, March 5, 2021

*Building on the investigations in Chapters 4 and 5, which focused on introducing robust magnetism in graphene nanoribbons and triangulene-based polymers, Chapter 6 extends the exploration of spintronic materials to carbon-doped triangular boron nitride (tBN) monomers arranged in a 2D polymer framework. Through first-principles DFT calculations, this chapter examines how carbon substitution in tBN monomers enables the emergence of spin-polarized ground states and long-range magnetic order, addressing the challenge of achieving stable ferromagnetism in a traditionally insulating material. Similar to the approach in Chapter 5, where boron and nitrogen doping in triangulene polymers led to enhanced spin coherence and transport properties, this chapter explores how doping strategies can be applied to boron nitride systems to engineer desirable electronic and magnetic features. The study reveals that specific carbon-doped configurations introduce collective magnetism and create semiconductor properties with coexisting Dirac and flat bands near the Fermi level, offering high carrier mobilities and spin coherence. Moreover, the chapter highlights how varying the arrangement of doped monomers can result in different electronic behaviors, from spin-polarized semiconducting to non-magnetic states, depending on the orbital overlap and symmetry. By bridging the findings from earlier chapters, this work provides a cohesive understanding of how defect-engineered and doped 2D materials can be optimized for spintronic applications, ultimately advancing the development of organic materials with metal-free magnetic ordering and anisotropic topological states.*



**Abstract :**

The electronic and magnetic properties of 2D polymer built from triangular boron nitride monomers (tBN) doped with C atom are investigated with first-principles DFT calculations. Polymers made of pure tBN are insulators as pristine h-BN, but substituting the central B(N) by C atom in tBN(NB) spontaneously leads to the creation of a spin-polarized ground state polymer.

Moreover, the ground state of C-doped polymer is an open-shell semiconductor in which both Dirac and flat bands coexist nearby Fermi level while the nearest excited state is a closed-shell semi-metal where the Dirac cone crossed Fermi level. The triangular shape of the monomer, the nature of atomic substitution, and the relative position of C-dopant among the 2D polymer are contributing to create a strong collective magnetism in conjunction with a significant orbital overlap between C-dopants separated by 1.0 nm. This collective magnetism is totally suppressed in (CtBN-CtNB) copolymer arrangement, where the material shows a semiconducting gap with no spin-polarization and strongly localized states around Fermi level. The results predict a 2D material with long range metal free magnetic ordering, in conjunction with high carrier mobilities from Dirac bands and anisotropic shapes of topological states, that opens the door for 2D organic spintronic applications.

## 6.1 Introduction

The development of metal-free magnetic applications from C-based materials, such as graphene, remains a major challenge since the last 2 decades [124]. Beyond graphene, a plethora of polymeric units can also be used to produce materials with comparable electronic properties to graphene, more especially regarding the Dirac cones [49,111]. The electronic and magnetic properties of 2D organic polymers are strongly influenced by the atomic structure and the nature of dopant among the building blocks [125]. Although a major difficulty persists to characterize magnetic materials in contact with metal that screens or quenches its magnetic behavior, a recent experimental evidence of the persistence of magnetism with a pure carbon triangulene dimers adsorbed on Au(111) keeps horizons widely opened for applications [37]. Such interest for organic triangulene is to build 2D polymers, but in contrast to graphene, for which the band gap can be controlled [36,49,105]. In particular, 2D conjugated polymers made from C-based nanoflakes are predicted to show graphene like Dirac cone around Fermi level [111], and can be covalently formed on surfaces without defects from triangular nanoflakes [126]. For example, Galeotti *et al.* [50] synthesized two different mesoscale sized ordered 2D Kagome lattice (KL) that are characterized by Dirac cones and flat band features on Au(111) surface. Furthermore, these specific materials were predicted to have high carrier mobilities that can reach values up to 8000 $cm^2\ V^{-1}\ s^{-1}$, that is similar to the observed value for crystalline silicon [49]. Surprisingly, although doped-heterotriangulene monomers have unpair electrons, only closed-shell structures were reported. Since magnetism is conserved with triangulene dimers on Au(111) [37], there are good reasons to

believe that it should be also observed with heterotriangulenes as well. In addition, ferromagnetism is typical for the presence of flat bands [127]. However, due to the presence of highly reactive lone pair C-atom at edges in triangulene, it is reasonable to terminate those edge atoms such a way to form closed-shell derivatives and that leads to diamagnetic ground states in the triangulene based KLs even with the B and N dopants [49]. From a different perspective, the building block in 2D KL polymers can be viewed as superatoms arranged in a hexagonal unit-cell like graphene, and exhibit an equivalent semi-metal behavior as graphene near the Fermi level, through the presence of Dirac cones [49,111,125]. By realizing that central dopants in heterotriangulenes play a major role in the resulting electronic properties, we also explored the role of such dopant within a non-conjugated environment such as triangular boron nitride nanoflakes. It is also fundamentally important to realize magnetic behavior in materials made of light-weight atoms containing only s and p orbitals in addition to transition metals. Owing to the higher stability of the BN based triangular nanoflakes [128,129], it is quite justified to study 2D polymers made of these derivatives and to explore magnetism in that organic framework.

In order to realize the magnetic properties in 2D polymers influenced by the presence of dopant, we have investigated dimers and KL polymers built from boron nitride nanoflakes in a triangular shape, and doped with carbon. Magnetism in C-doped boron nitride materials has been already reported for nanoflakes [130,131], nanoribbon [132–135], nanotubes [135–139], and sheets [135,140–144]. On the other hands, although the presence of carbon in BN was shown to have a major impact on the transport properties of nanoribbons and nanotubes [145], there are no clear evidences for spin-dependant transport. Zhao *et al.* partly explained this behavior by showing that coupling between local magnetic moments increases as the separation between C dopant decreases, to a point (around 0.6 nm) where the exchange coupling is sufficiently important to convert the long-range ferromagnetic state into an antiferromagnetic. Hence, since an efficient charge transport would be favored in systems with short distances between C dopant to maximize the orbital overlap, this would obviously favor the antiferromagnetic phase [141].

## 6.2 Computational Details

This current study is aiming to theoretically anticipate the ferromagnetism or anti-ferromagnetism along with the emergence of the flat bands in a chemically stable 2D organic framework. A defect free system is considered, influenced by the possibility to synthesize large scale KLs from the

triangular derivatives [50]. The main advantage in using triangular BN nanoflakes to build C-doped materials, as for heterotriangulenes [50], is to potentially synthesize the building blocks from borazine-based molecules with an atomic precision. Following the spirit of the precursors used along the Ullmann coupling to produce 2D polymer from heterotriangulenes, we considered C-doped halogenated boron nitride triangular units shown in Figure 6.1 in the DFT calculations. Since the electronic properties of such triangular BN nanoflakes depend on the composition of edges, we also differentiate the a) N-edges triangular BN (CtBN) and b) the B-edges triangular BN (CtNB) doped precursors. Following Ullmann reaction path, the B−Br (N−Br) bonds are broken to form the $P^2$-tBN ($P^2$-tNB) polymer or copolymer (P-(tBN-tNB)) illustrated in Figure 6.1c. In order to validate the consistency of our findings, we deliberately used two different computational approaches to evaluate the electronic properties of monomers and polymers. The electronic structure calculations on monomers and dimers were performed with the density functional theory (DFT) and time dependent DFT methods included in the NwChem 6.6 package [146]. The molecular structures were fully optimized without any symmetry constraints with a quasi-Newton technique until the gradient convergence factor was lower than $10^{-5}$ Hartree/Bohr. We have used 6-311G basis sets for all atoms, in conjunction with PBE0 exchange-correlation functionals and van der Waals corrections [100]. The electronic structures of the 2D KL polymers were carried out using DFT contained in Quantum ESPRESSO package [55,97] (PAW potential [101], cutoff energy of 480 eV, Monkhorst-Pack [147] k-point grid of 8 × 8 × 1 and PBE functional [96]). Since PBE belongs to the group of generalized gradient approximation, it takes into account the density of the local sites along with its few neighbouring sites. Therefore, PBE functionals correct the local spin density approximation by considering the gradient of densities around the local site which is more robust during the quantum calculation of electronic structure and is already proved to give very accurate results for a variety of systems. In addition, we have taken PAW potentials instead of ultra-soft pseudo-potential since PAW can better restore the pseudo-wavefunctions up to almost all electron contributions. The images of the molecular models were generated with the Chimera software [148], and the charge density plots were produced with the VESTA software [149]. More computational details are provided in the Supporting Information in Appendix C.

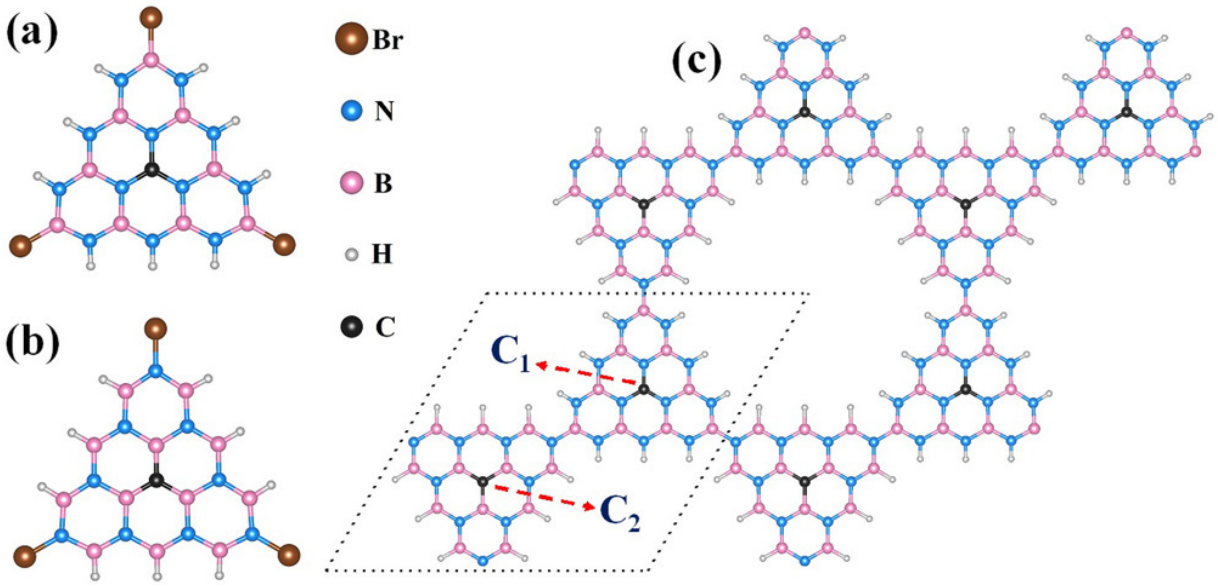


Figure 6.1 Models of a) CtBN and b) CtNB molecular precursors, and c) Kagome lattice constructing the C-doped copolymer where the dashed tiling represent the unit cell. The C atom centered in the tBN(NB) monomer substitutes a B(N) atom, and gives a n(p)-doped building block.

## 6.3 Results and Discussion

Prior to discuss the electronic and magnetic properties of tBN polymers, we first describe the properties of simple monomer and dimer units. Table 6.1 summarizes the band gap characteristics of all systems considered, including the 2D polymer. As expected, the band gap value decreases from the monomer to the polymer for most species due to the formation of an increasing amount of bonds between boron nitride units. The ground state of the undoped dimers is stable with a closed-shell configuration, and although the band gap depends on the chemical nature of the triangular edges, both dimers show insulator characteristics. Furthermore, the nature of frontier orbitals and the vertical transitions among them are contrastingly different from (tBN)2 to (tNB)2 (Table S1 and Figure S1, Supporting Information in Appendix C).

The C-doped monomers have an unambiguous single unpaired electron, and that electron remains unpaired in the dimer except for CtBN-CtNB for which the ground state is a closed-shell singlet state. The distance between C-dopant in the dimers, ≈1.04 nm, agrees with the turning point for exchange coupling proposed by Zhao *et al.* [141] where a ferro- to antiferromagnetic transition should occur. The total energy difference between low spin singlet and high spin triplet states of C-doped systems is around 1.2–1.4 eV, indicating very stable ground state systems. The doping

considerably reduces the band gap values, and the vertical (HOMO-LUMO) transitions are favored in (CtBN)2 and (CtNB)2, and are practically forbidden in the mixed (CtBN-CtNB) dimer. This last behavior can be easily understood from the nature of frontier orbitals of CtBN-CtNB dimer that are strongly localized on CtBN or CtNB monomer, with virtually no coupling between them. We also observed that C-dopant, more especially in (CtBN)2 and (CtNB)2, improves the orbital delocalization among the dimers (Figure S1, Supporting Information in Appendix C).

Table 6.1 Electronic structure properties of the more stable singlet (S) and triplet (T) states of tBN dimers and polymers. The band gap $E_g$ and $E_{gP}$ are obtained from $|\varepsilon_{HOMO} - \varepsilon_{LUMO}|$, while $E_g^*$ is the energy of the few first electron transition calculated with TDDFT. See Table S1, Supporting Information (Appendix C) for more details.

| Dimer | ΔE [eV] | State | $E_g$ [a] [eV] | $E_g^*$ [b] [eV] | $E_{gP}$ [c] [eV] |
|---|---|---|---|---|---|
| $(tBN)_2$ | 0.00 | S | 6.44 (7.70) | 5.63 | 4.55 |
| | 4.45 | T | 3.94 | | |
| $(CtBN)_2$ | 0.00 | T | 2.95 (3.44) | 2.16 | 0.25 |
| | 1.18 | S | 0.64 | 0.93 | |
| (CtBN-CtNB) | 0.00 | S | 1.26 | 0.90[d] | 1.48 |
| | 1.36 | T | 1.55 | >1.92 | 0.22 |
| $(CtNB)_2$ | 0.00 | T | 2.84 (3.12) | 2.06 | 0.72 |
| | 1.21 | S | 0.54 | 0.85 | |
| $(tNB)_2$ | 0.00 | S | 5.48 (5.78) | >5.22 | 3.47 |
| | 2.41 | T | 4.83 | | 2.41 |

a) HOMO-LUMO gap from DFT, the value in parenthesis is the monomer value; b) first vertical transition from TDDFT; c) polymer band gap from DFT; d) this transition is allowed but is associated to a relatively low oscillator strength (Table S1, Supporting Information in Appendix C).

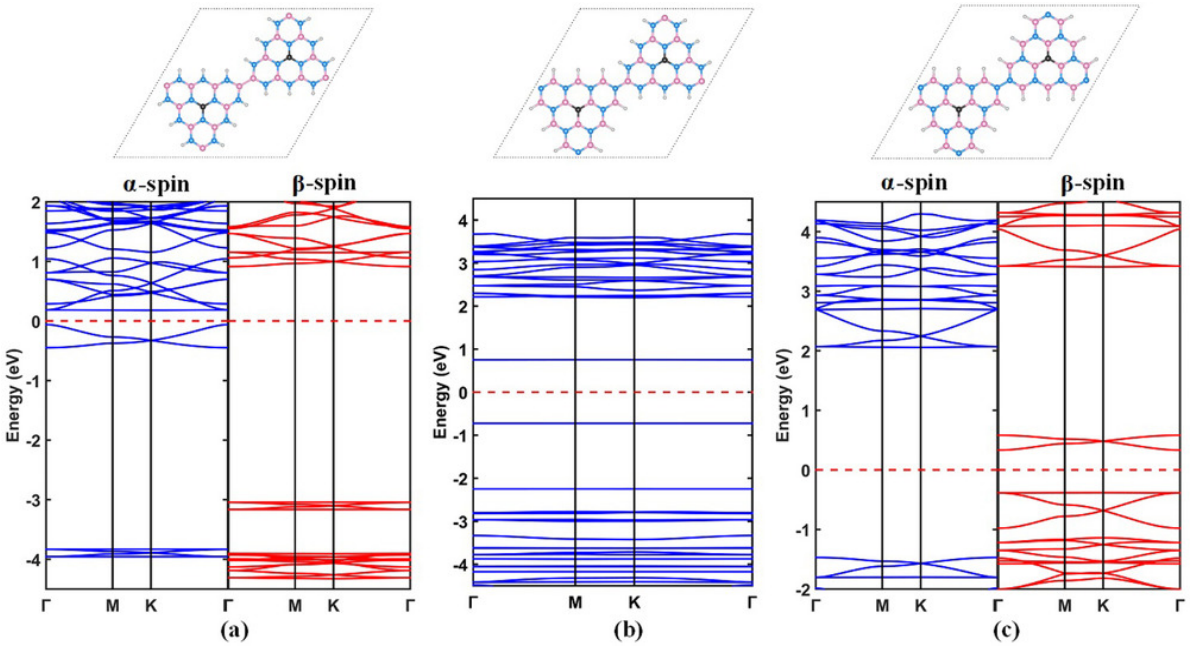


Figure 6.2 Band structures of ground states of Kagome polymer based on a) CtBN and b) CtBN-CtNB and c) CtNB along with their corresponding unit cells (top). The Fermi level has been referenced to zero and is identified by the red dashed line. Triplet state spins are indicated inside the figure.

The calculated electronic structure properties of tBN/tNB polymer and copolymer are fully consistent with results obtained on dimers. First, the polymers made of undoped tBN show large band gap and weakly dispersed bands, as for h-BN insulator. We also point out that band gap for $P^2$-tBN with N-edges terminated is larger than in the B-edges terminated ($P^2$-tNB) polymer. Second, we found similar open-shell (triplet) ground states for C-doped polymers and closed-shell (singlet) for the copolymer, the resulting band structures are shown at Figure 6.2. The C-doped polymers present similar well-dispersed Dirac cones and flat bands around Fermi level than those expected for a conjugated 2D KL polymer [49]. In this open-shell ground state, the Dirac cone is shifted below (above) Fermi level for $\alpha$-spin ($\beta$-spin), to create a small band gap in $P^2$-CtBN ($P^2$-CtNB) where a B (N) atom was substituted by C atom to make a n-type (p-type) semiconductor (see Figure 6.2a,c). We do not observe such features for $\beta$-spin ($\alpha$-spin) for $P^2$-CtBN ($P^2$-CtNB), but a wide band gap and weakly dispersed bands. This contrasts with the first (singlet) excited states where the Dirac cone crosses the Fermi level and makes the polymers, a semi-metal (Figure S2, Supporting Information in Appendix C).

A peculiar phenomenon can be observed here: although the distance between C atoms in polymers is about 1.0 nm, monomers act like $sp^2$ hybridized $\pi$ orbitals as in graphene, and are at the origin of highly dispersed Dirac bands within an insulating material like boron nitride. A more detailed analysis of the projected density of states (PDOS) for 2p-orbital of C (C2p) atoms clearly reveals Dirac bands mainly originate from the contribution of C atoms among the KL polymer (Figure S3, Supporting Information in Appendix C). In addition, the analysis of PDOS also shows that C atoms are not responsible for the presence of highly localized flat bands around the Fermi level of perfect CtBN and CtNB polymers. In contrast, the presence of C atoms in the copolymer gives rise to very weakly dispersed bands around Fermi level that originate from C atoms but remain strongly localized on one or the other monomer, with very little or no overlap with neighboring monomers. The copolymer exhibits a diamagnetic Mott insulating phase around the Fermi level (see Figure 6.2b); which points toward the quantum confinement behavior among the individual monomers that comes from the symmetry breakdown of the polymeric building blocks. Figure 6.3 gives a different perspective of Dirac bands dispersion in the vicinity of Fermi level, where we see a major electron delocalization among the entire KL network for the $P^2$-CtBN (Figure 6.3a) and $P^2$-CtNB (Figure 6.3b) polymers, and a strong electron localization on individual units in the copolymer (Figure 6.3c,d). The C2p-orbital on tBN and tNB are not overlapping in the copolymer for energy and symmetry reasons, the C2p orbitals interact among a single monomer to induce a p- and n-doped species in CtNB and CtBN, respectively. In addition to this long-range orbital-coupling, our results identified a significant spin-coupling in $P^2$-CtBN and $P^2$-CtNB polymers where the coupling of local magnetic moment centered on C ($\approx$0.20 $\mu$B) leads to a magnetization up to $M$ = 2.3 $\mu$B per cell, which is an order of magnitude higher than the local components (Table S2, Supporting Information in Appendix C).

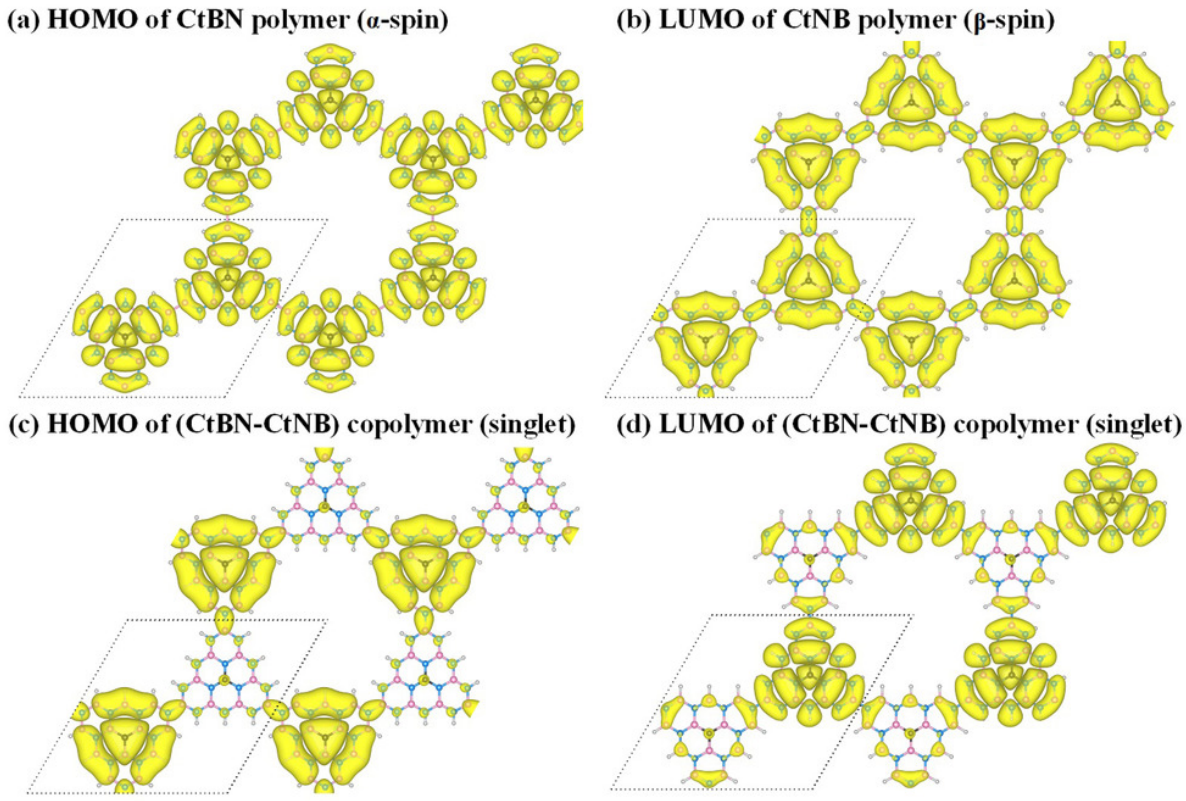


Figure 6.3 Charge density distribution of different polymeric configurations for different bands in different states (indicated inside the figure). Isosurface has been set to 0.0002 e $Å^{-3}$ for all figures.

We turn now on the description of flat bands around Fermi level, they are strictly different from the polymer to the copolymer. As explained above, the contribution of C-dopants to the formation of flat bands is negligible in the polymers but becomes dominant in the copolymer. For polymers, the charge density distribution for flat bands (Figure S4, Supporting Information in Appendix C) of $\alpha$-spin ($\beta$-spin) of CtBN (CtNB) show no contribution from the central C atoms, and the charge density within a monomer is localized on edges that, in combination to other unit cells, forms a highly anisotropic charge density channel along the two directions where the monomers bind into a polymeric form. These flat bands show the main characteristics of a topological states [150]. As shown in Figure 6.3, the presence of flat bands for the copolymer is related to the strong charge localization on one monomer below Fermi level (HOMO) and on the second monomer above Fermi level (LUMO). In addition, the copolymer is found non-magnetic, and in absence of orbital-coupling between super-atoms, this creates highly localized molecular orbital or flat bands instead

of Dirac bands near the Fermi. In contrast to the flat bands described above for the polymer, these are not topological states.

Table 6.2 Estimated effective masses ($m^*$) and mobilities (μ) for various charge carriers in ground states C-doped tBN/tNB polymers and copolymer. The values for the deformed potential (ζ) and the elastic modulus (χ) are given for reference.

| Polymer | Carrier | Spin | $m^*$ [$m_0$] | ζ [eV] | χ [$Nm^{-1}$] | μ [$cm^2\ V^{-1}\ s^{-1}$] |
|---|---|---|---|---|---|---|
| P²-CtBN | e | α | 13.61 | 1.86 | 12.57 | 0.28 |
| | h | α | 0.11 | 2.75 | | 1997.40 |
| P²-CtNB | e | β | 0.54 | 1.46 | 11.11 | 249.35 |
| | h | β | 2.23 | 0.67 | | 69.82 |
| P-(CtBN-CtNB) | e | - | 13.61 | 3.78 | 14.03 | 0.08 |
| | h | - | ∞ | 1.85 | | ≈0 |

Finally, the presence of spin-dependent Dirac cones in $P^2$-CtBN ($\alpha$-spin) and $P^2$-CtNB ($\beta$-spin) polymers suggests highly mobile charge carriers for one side of Fermi level and nearly immobile charge carriers for the other side which can even quench the kinetic energy of the carriers. According to the method described by Jing and Heine [49], we have estimated the mobilities into the C-doped polymers and copolymer, the results are summarized in Table 6.2. As observed in Table 6.1, band gaps vary from 0.25 to 1.48 eV for corresponding polymers, where the extreme of the Dirac bands lie at Γ-point. For the Dirac bands with $\alpha$-spin in $P^2$-CtBN, an effective mass of $0.11m_0$ is found, which is a little less than for $P^2$-CtNB ($0.54m_0$). All the effective masses and calculated mobilities ($\mu$) for the ground states of different polymeric configurations are tabulated in Table 6.2. The calculation procedure is described in the Supporting Information. $P^2$-CtBN configuration is found to be more mobile for the $\alpha$-spin holes, ($\mu$ = 1997.40 $cm^2\ V^{-1}\ s^{-1}$) than the $P^2$-CtNB for the $\beta$-spin electrons, ($\mu$ = 249.35 $cm^2\ V^{-1}\ s^{-1}$). In contrast, the flat band is found to be more mobile and slightly more dispersed in $P^2$-CtNB than in $P^2$-CtBN, where the highest calculated effective mass is about $13.61m_0$ and for both lattice, the extreme of the flat bands are found at K-points. However, the HOMO of the copolymer possesses a complete flat band with a large effective mass that tends to ∞, that in turn corresponds to highly localized and immobile holes in the copolymer. In addition, the electrons in the copolymer are also found to be almost immobile ($\mu$ =

0.08 $cm^2 V^{-1} s^{-1}$). It is worth mentioning that electron–phonon interaction was not considered for the mobility calculation, which might result in marginally overestimated mobility values.

## 6.4 Conclusion

In conclusion, we have shown with the help of first principles calculations, the coexistence of long-range orbital and spin-coupling in a Kagome lattice polymer formed from C-doped triangular boron nitride (tBN) nanoflakes. We showed that polymers built from tBN units present Dirac bands states with high carrier mobilities that are strongly spin-dependant. We also identified flat bands states that have the main characteristics of topological states in polymers but that exist as strongly localized states in the copolymer. Owing to the chemical stability of our proposed materials, this study should certainly motivate and help the scientific community in 2D materials to synthesize ferromagnetic organic polymers with the co-existence of non-trivial topological states and highly dispersive Dirac bands in planar 2D organic frameworks made of light-weight atoms.

# CHAPTER 7 CHARACTERIZATION AND DYNAMICS OF MAGNETISM IN 2D-KAGOME HETEROTRIANGULENE STRUCTURES

## 7.1 Introduction

As discussed earlier in Chapter 2 (Section 2.3.3), heterotriangulene (HT)-based Kagome polymers exhibit both Dirac bands and flat bands near the Fermi level, potentially leading to exotic properties such as topological insulating states [49]. Motivated by these unique properties, we sought to explore the dynamics of magnetism in 2D Kagome polymers made from HT monomers, specifically trioxoazatriangulene (TANGO), referred to as CTPA in ref. 49 (see Figure 2.13). In continuation of the exploration of defect-engineered magnetism and topological phases in low-dimensional materials discussed in Chapters 4 through 6, this chapter builds on the established themes of how defects, doping strategies, and structural modifications influence the emergence of robust magnetism. By leveraging the unique properties of heterotriangulene-based Kagome polymers, this chapter focuses on synthesizing and analyzing a TANGO-based 2D polymer using the Ullmann coupling reaction on an Au(111) substrate.

Through a combination of experimental AFM/STM imaging and DFT+U calculations, we demonstrate the emergence of spin-polarized states and localized magnetic moments when unpaired electrons are introduced via chemical modification in TANGO polymer. DFT+U calculations further explores how defect concentration and symmetry breaking affect the magnetic and electronic properties of the polymer, leading to increased band localization and the disruption of Dirac cones at the K points of the Brillouin Zone (BZ). By investigating the behavior of multiple defects per unit cell, we draw parallels to the findings in Chapters 4, 5 and 6 regarding the impact of localized spins on system-wide magnetic ordering. This chapter thus reinforces the broader thesis objective of advancing organic spintronic materials by providing new insights into the tunability of magnetic and topological properties in 2D Kagome polymers, paving the way for future applications in quantum devices. We emphasize that this chapter is theoretically driven and contains unpublished experimental results. Although it is work in progress, it demonstrates that DFT calculations constitute a very powerful and accurate tool to predict electronic and magnetic properties.

## 7.2 Results and Discussion

### 7.2.1 Synthesization of TANGO Polymer

Using the Ullmann coupling reaction, our collaborators achieved a covalent structure composed of TANGO monomers after annealing at 300°C on Au(111) substrate [50]. Figure 7.1a presents the experimental AFM image of the 2D Kagome polymer (2D-KP) made from TANGO, while Figure 7.1b displays the STM images at different bias voltages for conduction (top) and valence (bottom) regions.

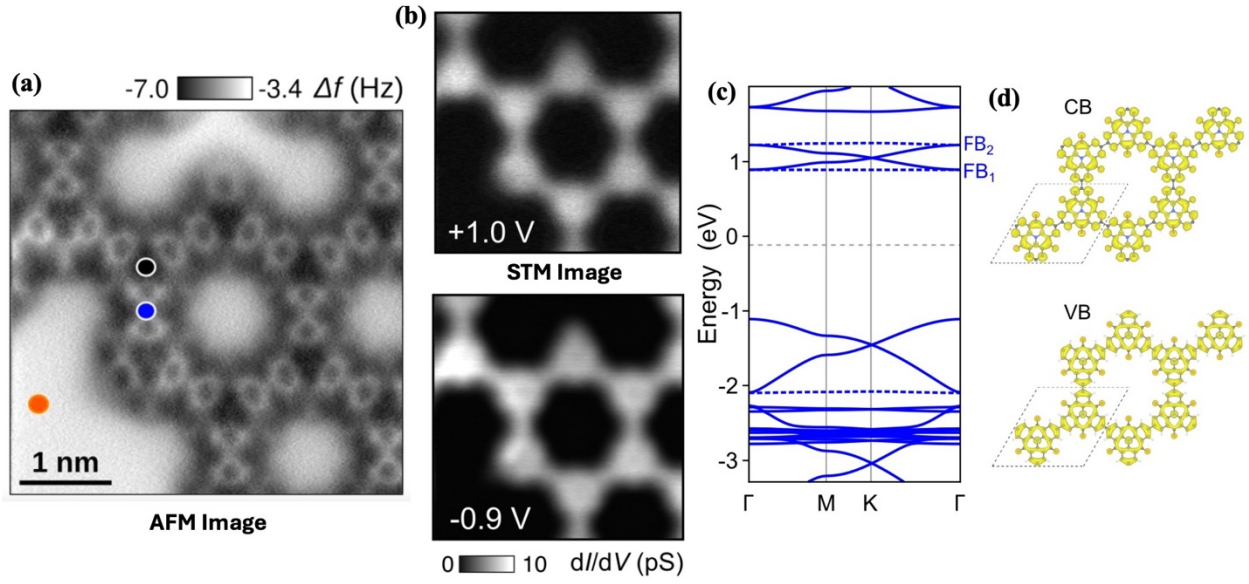


Figure 7.1 (a) AFM image of the TANGO polymer on Au(111) substrate with color-coded markers indicating specific sites for electronic measurements (not in the scope of this thesis). (b) STM images at bias voltages of +1.0 V and -0.9 V, highlighting the topographical features and electronic states. (c) Electronic band structure showing the flat bands ($FB_1$ and $FB_2$) and other Dirac like conduction and valence bands; (d) Charge density distributions associated with the CB and VB states, illustrating the spatial distribution of electronic states in the material.

We further investigated the electronic properties of this 2D-KP using the DFT+U method described previously. Figure 7.1c shows that our simulated band structure of this TANGO 2D-KP system closely matches Figure 2.14c as found by Jing *et al.* [49]. We observed flat bands in the conduction region, degenerated at the Γ-point of the BZ with Dirac-like bands, while the valence band features Dirac bands similar to graphene, although their dispersion is 20 times less than that of graphene. Additionally, we plotted the charge density at the Γ-point of the BZ for the first conduction band (CB) and valence band (VB) (see Figure 7.1d). These plots correspond well with our experimental

STM images (Figure 7.1b) and demonstrate the delocalized nature of the VB and CB throughout the 2D-KP structure.

### 7.2.2 Introducing Free-Radicals in TANGO Polymer

Inspired by Wang *et al.*'s study [40] on magnetic aza-triangulene (see Figure 2.9), we attempted to introduce unpaired electrons into the TANGO-based 2D-KP system. As described in their study [40], unpaired electrons can be introduced by hydrogenating the ketone group and then performing a dehydrogenation process to remove one atom from the hydrogen dimer group at the edges (see Figure 7.2a).

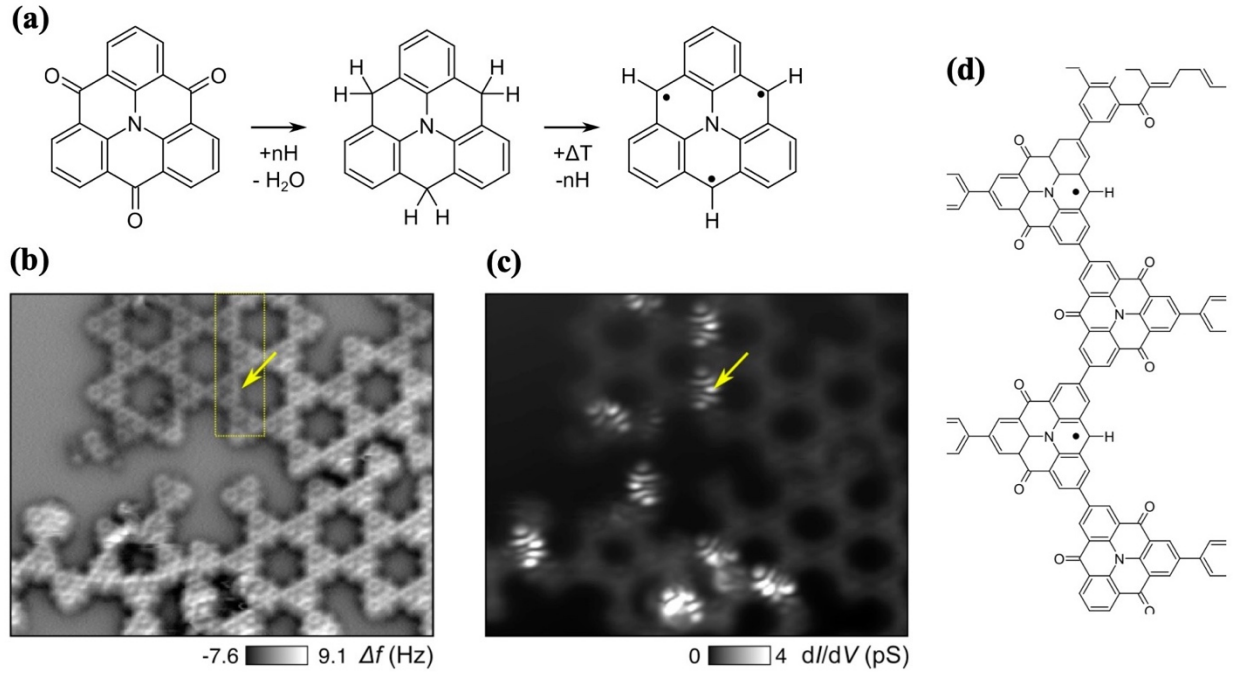


Figure 7.2 (a) Chemical reaction pathway leading to the generation of unpaired electrons in the TANGO molecule through sequential hydrogenation and dehydrogenation and thermal activation. (b) AFM image depicting the molecular arrangement, with the yellow arrow indicating the site of unpaired electron formation in TANGO polymer. (c) *dI/dV* map highlighting electronic states associated with the unpaired electrons in the polymer. (d) Schematic representation of the TANGO polymer in its high-spin state, post-unpaired electron generation, illustrating the extended molecular structure.

Following this procedure, we were able to create a few unpaired electrons throughout the polymer, as shown in the AFM and STM images in Figure 7.2b and 7.2c, respectively. However, we did not determine the conditions to replace all edge ketone groups with unpaired electrons in the polymer. This could be due to the low hydrogenation reaction yield in the polymer compared to the single

molecule. The corresponding structure of the TANGO-based 2D-KP with unpaired electrons is shown in Figure 7.2d, which reflects the yellow boxed region of the AFM image in Figure 7.2b.

### 7.2.3 Theoretical Investigation of Magnetic TANGO Polymer

Given the complex nature of this magnetic 2D-KP system, we further investigated its electronic and magnetic properties using the DFT+U method. The UC we considered is shown in Figure 7.3a, which includes one unpaired electron (UE) defect per UC, aligning well with the experimental structure (see Figure 7.2d). The non-spin-polarized DOS shows a non-bonding zero-mode state at the Fermi level, indicating a high-spin state in this 2D-KP (see Figure 7.3b). Additionally, we observed the opening of a Coulomb gap in the spin-polarized DOS in Figure 7.3c, representing the system's ground state. This gap results from the repulsive energy cost associated with unpaired spins attempting to occupy the same site in this magnetic system, similar to the triangulene dimer discussed in Figure 2.6a [37].

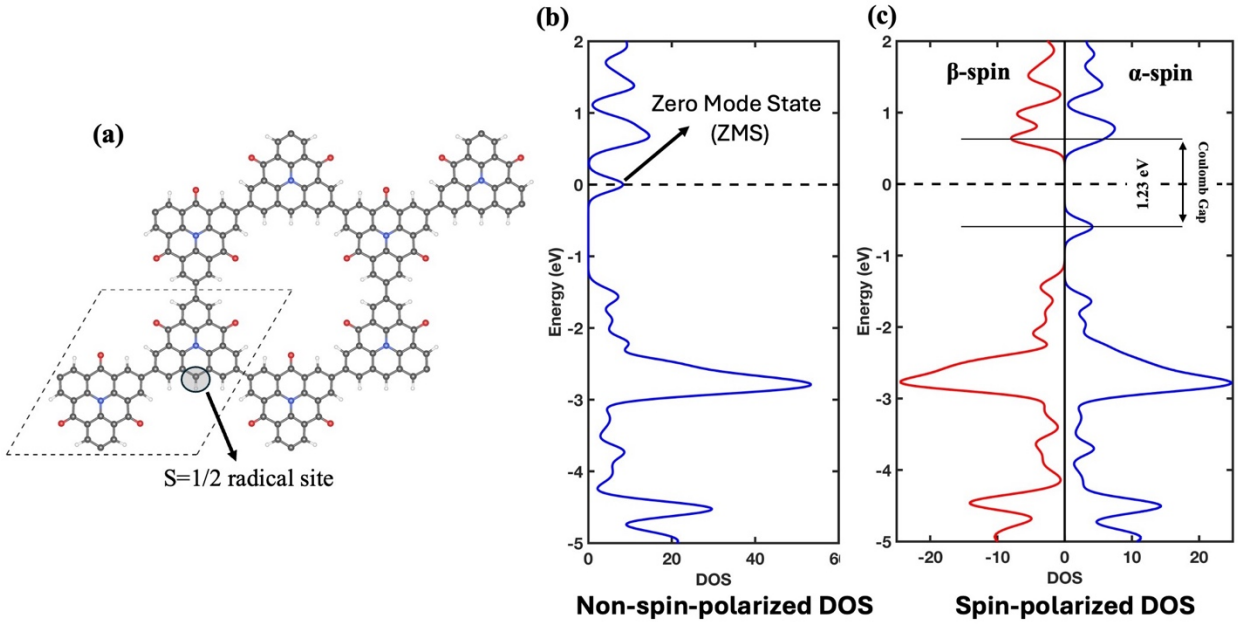


Figure 7.3 (a) Structural model showing the TANGO-based polymer with a highlighted *S*=1/2 radical site and the unit cell outlined. (b) Non-spin-polarized DOS highlighting the Zero Mode State (ZMS). (c) Spin-polarized DOS illustrating the separation between β-spin and α-spin states, with a Coulomb gap of 1.23 eV, indicating the electronic structure changes due to the presence of the unpaired electron in the polymer.

The presence of this magnetic impurity was also experimentally analyzed using STS (see Figure 7.4a). STS measurements were performed at two positions indicated on high-resolution STM

images (Figure 7.4b). The black solid circle denotes the position with a localized unpaired electron on the 2D-KP, and the red solid circle is placed on a no-defect site.

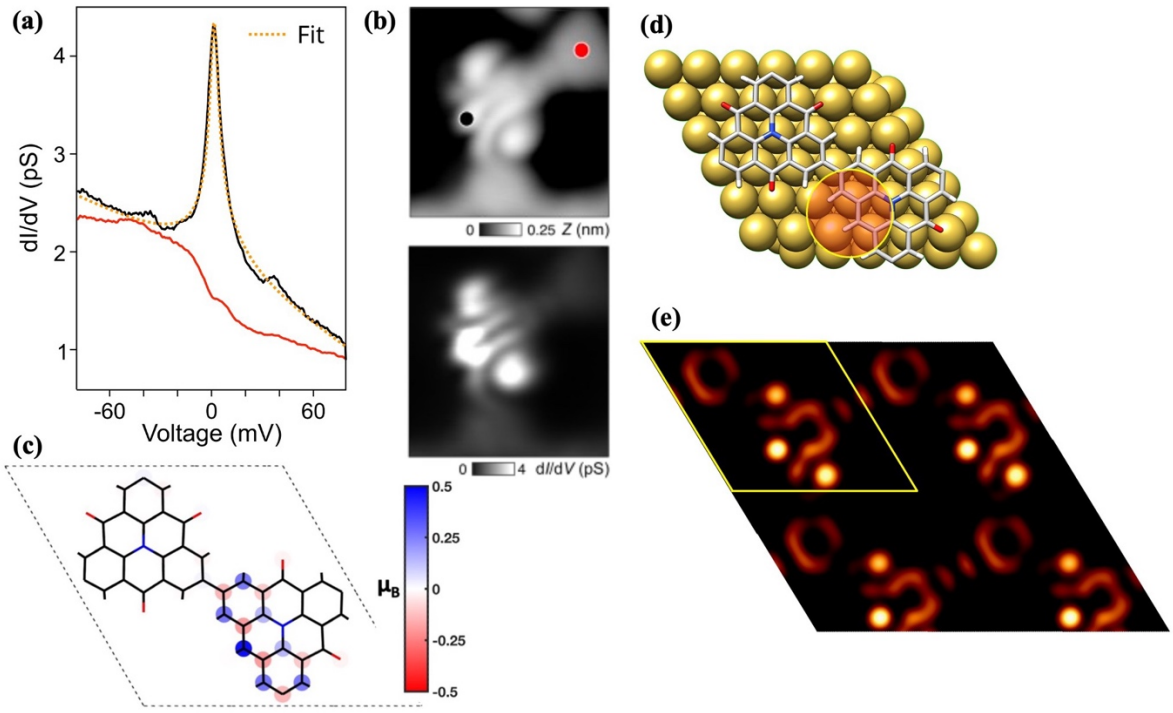


Figure 7.4 (a) STS measurements revealing a sharp peak at zero bias at the unpaired electron site (black solid line), indicating a Kondo resonance, compared to a no-defect site (red solid line). (b) High-resolution STM images: the top image is a constant current mode showing height variations (*Z*) in the scalebar (with black and red circles indicating the sites where STS measurements were performed), and the bottom image is a constant height mode with a *dI/dV* map. (c) Theoretical spin-density map of the 2D-KP system with one defect per UC, showing magnetic moments at the defect site. (d) Schematic diagram of the UC on an Au(111) substrate, highlighting the defect site with a red transparent circle. (e) Calculated LDOS map illustrating the localized nature of the unpaired electron, which aligns with the experimental STM images, confirming the theoretical model.

STS measurements on the unpaired electron site (black solid line in Figure 7.4a) revealed a sharp peak at zero bias, suggesting a Kondo resonance due to the interaction between the unpaired electron on TANGO 2D-KP and the conduction electrons of the underlying Au(111) substrate [40, 47]. No such anomaly was observed on the no-defect site (red solid line in Figure 7.4a). Our theoretical spin-density map of the one-defect per UC 2D-KP system in Figure 7.4c supports these high-resolution STM images, showing magnetic moments along the defect site but no magnetism at the no-defect site of the UC. The defect site is indicated by the red transparent circle in the schematic diagram of the UC on Au(111) substrate (Figure 7.4d), which aligns well with our

calculated LDOS map showing the localized nature of the unpaired electron (Figure 7.4e). Our calculated LDOS map also matches the experimental STM images, validating our theoretical approach to studying this system. Using a 2x2 supercell, we calculated $J_{eff}$=$J_{AFeM}$−$J_{FeM(triplet)}$ ≈ 0 meV for this TANGO 2D-KP with one defect per UC, indicating its paramagnetic nature.

In addition to our experimental findings, we investigated the influence of multiple defects per UC in the TANGO 2D-KP system (see Figure 7.5a-b). We observed AFeM coupling between the spins of neighboring monomers when considering two and four defects per UC, respectively (see Figure 7.5c-d). The energy difference between the ground state (AFeM) and FeM state, and the $J_{\text{eff}}$ values for all three systems, are tabulated in Table 7.1. Notably, in the four defects per UC system, we observed FeM coupling between spins of the same monomer, though they form an AFeM coupling with adjacent neighboring monomers. This behavior is similar to the triangulene dimer, which also includes four unpaired electrons [37]. Because of the quintet nature of its FeM phase, to get the actual $J_{eff}$ value for this four defects per UC structure, we have to divide the ΔE=$J_{AFeM}$−$J_{FeM(quintet)}$ by a factor of three as tabulated in Table 7.1.

Table 7.1 Energy difference (ΔE), Heisenberg spin exchange parameter ($J_{eff}$), and corresponding magnetic ground states for TANGO 2D-KP polymer with varying numbers of free radicals per UC in free-standing and Au(111) supported configurations.

| Polymers | | ΔE=$J_{AFeM}$−$J_{FeM}$ (meV) | $J_{eff}$ (meV) | Ground State |
|---|---|---|---|---|
| TANGO | | - | - | Non-magnetic |
| TANGO (1UE/UC) | Free-standing | - | - | Paramagnetic |
| | On Au(111) | - | - | Paramagnetic |
| TANGO (2UE/UC) | Free-standing | -95 | -95 | Antiferromagnetic |
| | On Au(111) | -48 | | Antiferromagnetic |
| TANGO (4UE/UC) | Free-standing | -192 | -64 | Antiferromagnetic |
| | On Au(111) | -114 | -38 | Antiferromagnetic |

Furthermore, we investigated the electronic properties of this structure with four UE per UC. The SP-DOS shown in Figure 7.6 demonstrates the degeneracy between spins in its AFeM ground state.

We found highly localized electronic states near the Fermi level. Our charge density plots for the VB and CB for both spins indicate that the radicals introduced in this structure are responsible for these localized states near the Fermi level. This observation aligns well with our experimental and theoretical findings for the one defect per UC system, confirming that radicals remain localized even when their number per UC is increased in this TANGO 2D-KP.

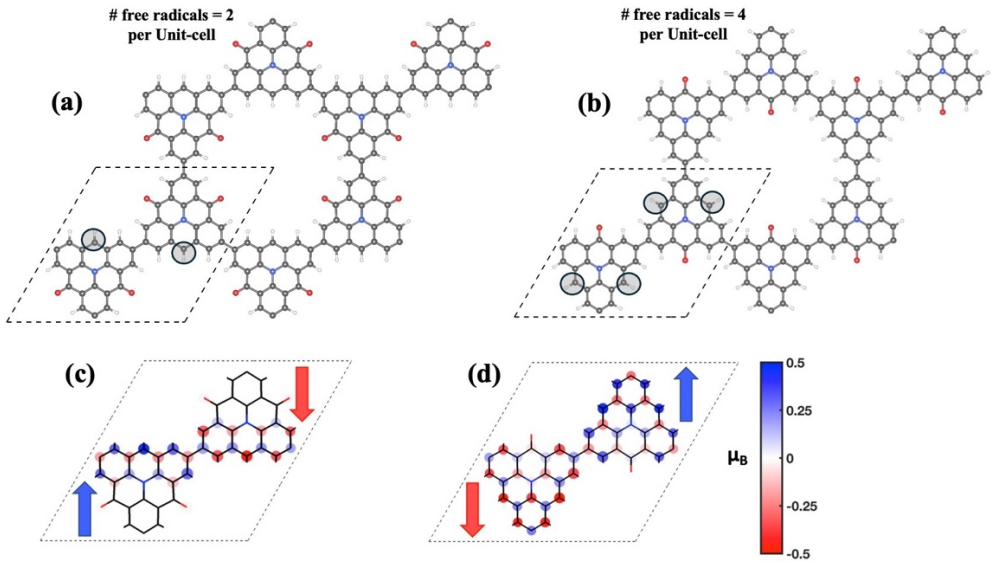


Figure 7.5 Magnetic properties of TANGO 2D-KP polymer with varying numbers of free radicals per unit cell: (a, b) Structural models of the TANGO polymer showing configurations with 2 (a) and 4 (b) free radicals per unit cell; (c, d) Spin-density distributions for the corresponding configurations with 2 (c) and 4 (d) free radicals, indicating spin alignment with blue and red arrows representing spin-up and spin-down orientations. The color scale represents the magnetic moment in units of Bohr magnetons ($\mu_B$).

Figure 7.7 illustrates the band structures for a TANGO 2D-KP polymer with increasing numbers of free radicals per UC, specifically 1, 2, and 4 radicals. In the leftmost panel (Figure 7.7(a)), where there is 1 free radical per UC, both spin-up (red) and spin-down (blue) bands are present, indicating spin polarization. The presence of the defect causes a breaking of symmetry, as reflected in the asymmetry between the spin channels. Additionally, the defect leads to the breaking of the Dirac cones at the K point, disrupting the characteristic linear dispersion typically seen in pristine Kagome lattices. This breaking introduces localized states near the Fermi level, leading to a distinct splitting of the bands. As we move to the middle panel with 2 free radicals per UC (Figure 7.7(b)), the band structure becomes more localized, particularly around the Fermi level. This localization is a result of the stronger interaction between the radicals, which further disrupts the periodicity of

the lattice and enhances the breaking of symmetry. Importantly, in this configuration, the α-spin and β-spin bands are degenerate in AFeM ground state. The bands in this configuration are noticeably flatter, indicating a higher degree of localization of the electronic states due to the presence of multiple defects. The breaking of the Dirac cones at the K point becomes more pronounced, further emphasizing the impact of the defects on the electronic structure.

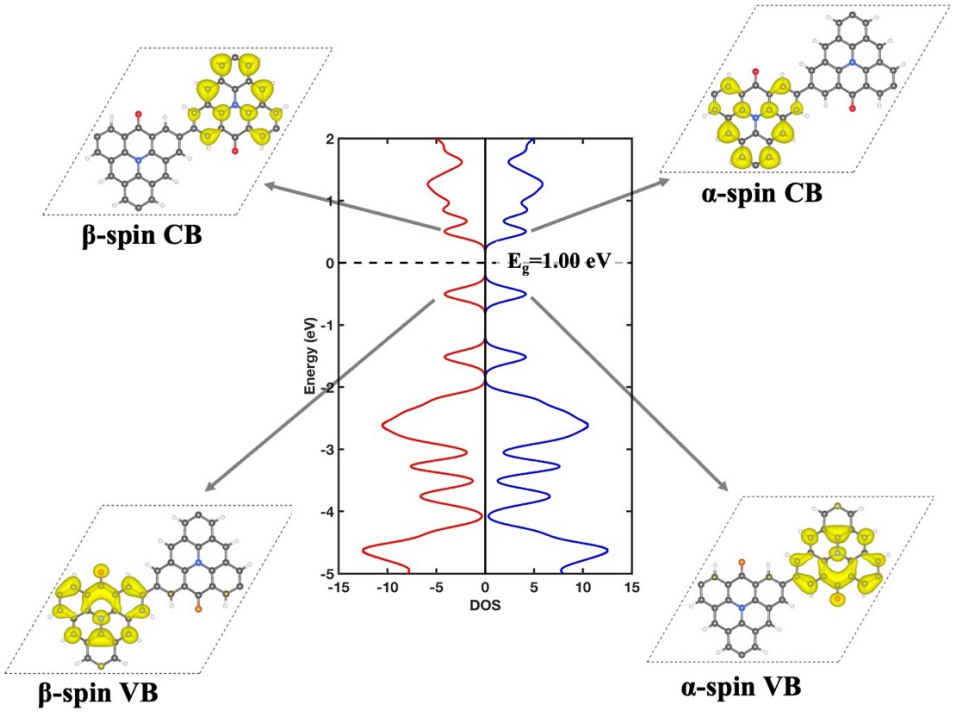


Figure 7.6 Electronic and Spin-Polarized DOS for TANGO 2D-KP Polymer with 4 Free Radicals per Unit Cell: The central plot displays the spin-polarized DOS with a band gap $E_g$=1.00 eV, where red and blue curves represent the α-spin and β-spin states, respectively. All states are degenerated for both spins. Surrounding the DOS plot are charge density distributions for the CB) and VB states, separated by spin: α/β-spin CB/VB, α-spin CB, highlighting the spatial localization of electronic states associated with each spin orientation.

In the rightmost panel, with 4 free radicals per UC (Figure 7.7(c)), the band structure exhibits even more pronounced localization effects. The bands near the Fermi level are highly flat and narrow, signifying strong localization of the electronic states. Similar to the 2 free radicals case, the α-spin and β-spin bands are degenerate, consistent with the AFeM ground state. The breaking of the Dirac cones at the K point is now even more severe, with the defects leading to a substantial alteration of the electronic structure. This increased localization is accompanied by a more significant breaking of symmetry, as the multiple defects interact and alter the electronic structure of the 2D-KP system.

The progression from 1 to 4 free radicals per UC shows a clear trend of increasing localization and symmetry breaking, alongside the emergence of AFeM ground states with degenerate spin bands and the pronounced breaking of Dirac cones at the K point. The results underscore the impact of defect concentration and symmetry breaking on the electronic and magnetic properties of the TANGO 2D-KP polymer, demonstrating how these factors can lead to significant modifications in the system's overall behavior.

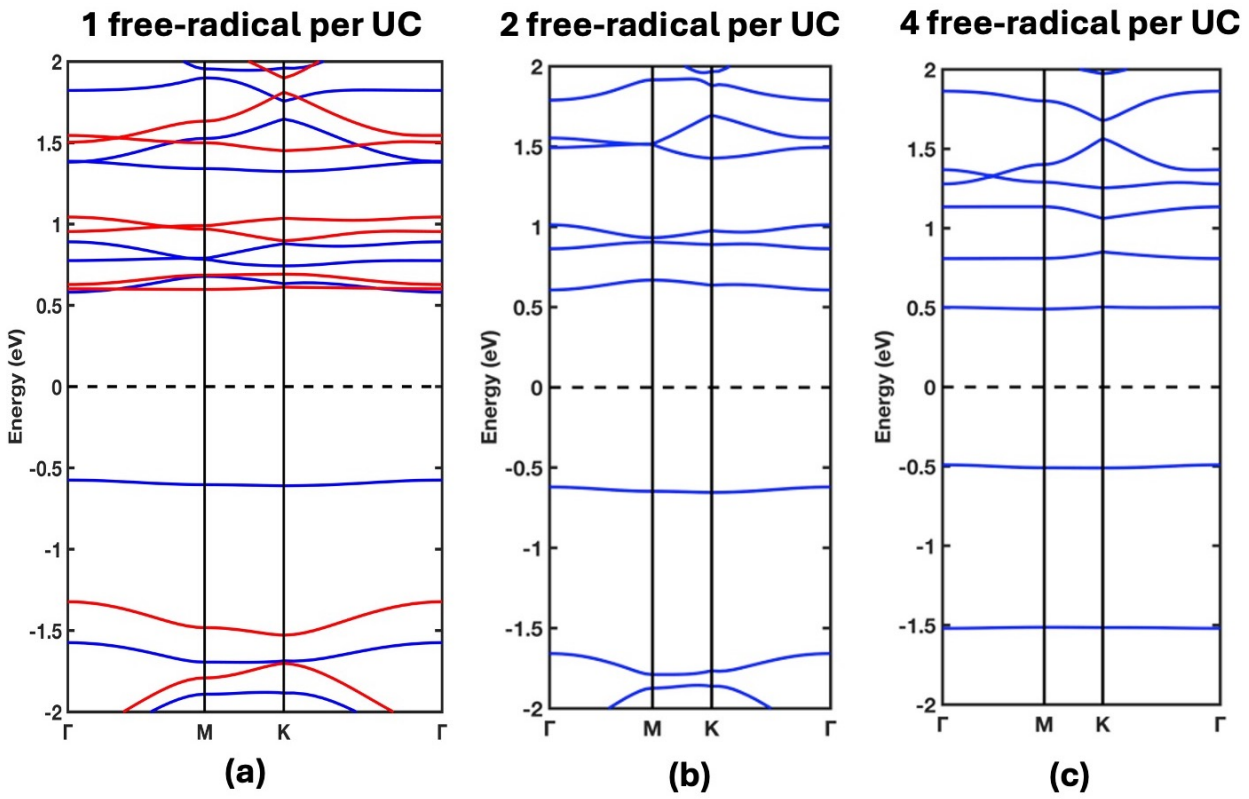


Figure 7.7 Band structures of TANGO 2D-KP with (a) 1, (b) 2, and (c) 4 free radicals per UC, illustrating the effects of defects on Dirac cone formation, band localization, and symmetry breaking at the K point of BZ. α/β-spin bands in (a) is denoted by red/blue solid lines. The α-spin and β-spin bands are degenerate in the AFeM ground states for configurations with 2 and 4 free radicals per UC.

As a future work aspect, if the defects in the TANGO 2D-KP polymer could be introduced while maintaining the overall symmetry of the lattice, it is plausible that the electronic structure could preserve the formation of Dirac cones at the K points, similar to those seen in pristine Kagome lattices. Symmetric incorporation of the defects would mitigate the disruption of the lattice periodicity, allowing the system to retain the linear band dispersion characteristic of Dirac cones. This symmetry would reduce the band flattening and localization observed with asymmetric defect

introduction, potentially leading to more delocalized electronic states. In such a scenario, the interplay between the unpaired electrons could stabilize Dirac-like excitations, preserving the high mobility of charge carriers and resulting in a system that combines the unique magnetic properties associated with the defects with the desirable electronic properties of a less localized and more conductive material. This approach could offer a pathway to engineer materials with tunable electronic and magnetic properties, balancing defect-induced magnetism with the advantageous transport properties of Dirac materials.

## 7.3 Conclusion

This study explored the magnetic properties and electronic structure of 2D Kagome polymers made from TANGO monomers. Using the Ullmann coupling reaction and annealing, we synthesized a covalent TANGO structure on Au(111) substrate. Our experimental and theoretical investigations revealed flat and Dirac bands near the Fermi level for the TANGO 2D-KP, consistent with predictions. Introducing unpaired electrons in this 2D-KP via hydrogenation and dehydrogenation resulted in localized magnetic moments, confirmed by STS measurements showing Kondo resonance at defect sites. Spin-density maps supported these findings, showing magnetism at defect sites but not in the rest of the structure. Examining multiple defects per unit-cell, we found that radicals remain localized and observed antiferromagnetic coupling between neighboring monomers. In conclusion, the introduction of defects in the TANGO 2D-KP disrupts lattice symmetry, leading to the breaking of Dirac cones at the K points, band flattening, and increased localization of electronic states. This results in significant alterations to the electronic and magnetic properties of the material. However, if future work focuses on introducing these defects while maintaining lattice symmetry, it could preserve the formation of Dirac cones, reduce localization, and stabilize Dirac-like excitations, offering a balanced combination of defect-induced magnetism and enhanced electronic transport properties. This dual approach highlights the potential to engineer advanced materials with tailored properties for specific applications.

# CHAPTER 8 CONCLUSION AND PERSPECTIVES

This thesis has explored the rich and complex field of low-dimensional organic materials, particularly focusing on their electronic and magnetic properties. The primary objective was to investigate how these materials could be manipulated at the molecular level to exhibit specific electronic and room-temperature collective magnetic behaviors in one-dimensional (1D) and two-dimensional (2D) systems, that are critical for advancing quantum technologies, including quantum computing, spintronics, and next-generation electronic devices.

## 8.1 A New Paradigm of Magnetism in Low-Dimensional Organic Magnets

Throughout this work, a strong emphasis was placed on understanding and enhancing magnetism in low-dimensional organic materials, particularly in 1D and 2D systems. The exploration began with molecular magnets, where it was demonstrated that organic magnets offer unique advantages over their inorganic counterparts, such as increased magnetic homogeneity, tunability, and reduced fabrication costs. The research revealed that by incorporating specific structural and chemical modifications—such as introducing pentagon edge defects in graphene nanoribbons or chemical substitution with different organic atoms (boron, nitrogen) in carbon-based Kagome polymers—the magnetic properties of these materials could be significantly enhanced. Specifically, the magnetic properties impacted by these modifications include the induction of localized magnetic moments and the transition from antiferromagnetic to ferromagnetic states, crucial for spintronics. Doping strategies, like boron in triangulene based Kagome polymers, enhanced spin coherence and increased carrier mobility, stabilizing ferromagnetic phases essential for spin-based devices. Additionally, carbon doping in triangular boron nitride (tBN) polymers enabled long-range magnetic order, while in heterotriangulene-based Kagome polymers, chemical modifications introduced unpaired electrons, leading to localized magnetic moments and spin-polarized states.

The studies on graphene nanoribbons (GNRs) highlighted the potential for inducing robust ferromagnetism by introducing non-benzenoid topological defects, which disrupt the graphene bipartite lattice and lead to highly ordered spin states. These findings suggest that defect engineering is a viable strategy for overcoming the challenge of maintaining and enhancing magnetism in low-dimensional organic systems. Moreover, the investigation into the effects of metallic substrates on these modified GNRs provided valuable insights into the real-world

applicability of these materials, showing that robust magnetism can persist even under substrate screening effects.

In the context of two-dimensional systems, Kagome polymers composed of organic triangulene monomers arranged in a hexagonal lattice structure, were a central focus of this investigation. These 2D polymers, with their distinctive Kagome lattice geometry, allow for unique electronic and magnetic behaviors, particularly due to the interaction between the triangulene monomers. The study demonstrated that a substitutional doping of these polymers with organic atoms such as boron or nitrogen could stabilize ferromagnetic phases, which is essential for spintronics applications. The all-carbon triangulene polymers generally exhibit antiferromagnetic ground states due to Mott-insulating behavior, but strategic doping can introduce metallic behavior and enhanced spin coherence. The results showed that by carefully selecting dopants—such as boron for high carrier mobility and nitrogen for half-metallic behavior—the electronic and magnetic properties of these polymers can be finely tuned to meet the requirements for spin-based logic devices and quantum storage applications. Further, the research explored how carbon-doped triangular boron nitride (tBN) monomers, arranged in a 2D polymer framework, can exhibit spin-polarized ground states and long-range magnetic order. Carbon substitution in these typically insulating boron nitride systems was shown to enable collective magnetism, with the ability to tune electronic and magnetic behaviors depending on the arrangement of the doped monomers. This demonstrated the versatility of defect-engineering approaches in organic systems and their potential for creating materials that exhibit a range of desirable properties, from semiconducting to spin-polarized states. Another critical exploration involved heterotriangulene-based 2D Kagome polymers made of TANGO (trioxoazatriangulene) monomers, where experimental and theoretical work demonstrated the emergence of localized magnetic moments via defect engineering. Spin-polarized states and Kondo resonances were observed at defect sites, emphasizing how symmetry breaking and defect manipulation could influence both Dirac cone formation and band localization. These findings deepen the understanding of the interplay between defect engineering and magnetism, advancing the broader goals of creating tunable organic spintronic materials for next-generation devices.

In summary, the research presented in this thesis opens up several promising avenues for future exploration. The following perspectives outline potential directions that could build upon the findings of this work and further advance the field of low-dimensional organic materials.

## 8.2 Exploring Topological Phases in Organic Materials

The research presented in this thesis has highlighted the potential for topological phases to emerge in low-dimensional organic materials, particularly in 2D Kagome polymers. The presence of Dirac and flat bands near the Fermi level in these materials suggests that they could exhibit exotic properties, such as topological insulating states, which are of great interest for quantum computing and other advanced technologies. Future research could focus on exploring the conditions under which topological phases emerge in organic materials and how these phases can be manipulated through chemical modification, defect engineering, and external fields. Additionally, the synthesis of new organic materials with non-trivial topological states could lead to the development of novel quantum devices with enhanced performance and stability.

## 8.3 Enhancing Superconductivity in Organic Systems

The exploration of superconductivity in low-dimensional organic materials, particularly in twisted bilayer graphene, has uncovered intriguing opportunities while also revealing significant challenges. A key discovery in this area is the identification of flat bands in such materials, which foster a high density of states at the Fermi level. This characteristic is conducive to the formation of Cooper pairs, a precursor to superconductivity. These findings represent a substantial step forward in understanding how superconductivity can emerge within organic systems, pointing toward the potential for novel quantum device applications. However, achieving superconductivity at practical, higher temperatures remains a significant barrier. Current results indicate that superconductivity in graphene-based systems only occurs at extremely low temperatures, around 1.7 K. This creates a considerable limitation for real-world applications such as energy transmission and storage, where room-temperature superconductors would be transformative. The observed superconducting states underscore the complex interplay between electronic structure, material composition, and external conditions, all of which need to be delicately balanced to achieve higher critical temperatures.

Our research contributes valuable insights into addressing these challenges. By investigating how different structural modifications, doping strategies, and hybrid materials influence electronic behavior, we have laid the groundwork for exploring new pathways toward enhancing superconductivity in low-dimensional organic systems. For example, our work on defect engineering and chemical modifications in 2D systems provides new perspectives on how localized

states and band structures can be manipulated to control electronic properties, potentially leading to more favorable conditions for superconductivity. The findings in this thesis, particularly around the introduction of dopants in low-dimensional systems, suggest that tailored doping strategies could play a critical role in stabilizing superconducting phases at higher temperatures. These modifications influence the density of states and the interaction strength between electrons, providing a promising route toward achieving more robust superconducting properties. Looking ahead, the potential for higher-temperature superconductivity in these materials will require continued exploration of new organic compounds, novel doping techniques, and better control over material synthesis. The advancements made in this research provide a roadmap for future studies, particularly in understanding how flat band structures and localized electronic states can be manipulated to enhance superconducting behavior. By building on these findings, there is significant potential to develop organic materials with superconducting properties at more practical temperatures. Theoretical insights from this research pave the way for experiments exploring these hybrid systems, potentially leading to more stable and higher-temperature superconducting phases.

## 8.4 Advancing Organic Spintronics

The findings of this thesis underscore the potential of organic materials in spintronics, particularly in the design of spin-based logic devices and quantum storage applications. Moving forward, research could focus on the development of new organic spintronic materials with improved magnetic stability and spin coherence. This could involve the exploration of novel doping strategies, defect-engineering techniques, and the synthesis of new 2D polymers with tailored electronic and magnetic properties. Moreover, the integration of organic spintronic materials into practical devices remains a significant challenge. Future efforts could aim to develop fabrication techniques that allow for the scalable production of these materials and their incorporation into device architectures. Additionally, the study of the interactions between organic spintronic materials and various substrates could provide valuable insights into how these materials can be optimized for real-world applications.

## 8.5 Final Remarks

In conclusion, this thesis has made significant contributions to the understanding and development of low-dimensional organic materials with unique magnetic and superconducting properties. The research has demonstrated the potential of these materials to play a central role in advancing

quantum technologies and has opened up new avenues for exploration in the field of materials science. By building on the findings of this work and pursuing the perspectives outlined above, future research has the potential to unlock the full potential of low-dimensional organic materials, leading to groundbreaking advancements in technology and our understanding of the quantum world.

# REFERENCES


1. Hurst, P. (2007). Metal-organic and organic molecular magnets. Royal Society of Chemistry.
2. Veciana, J. (1996). Organic magnetic materials. ChemInform, 28, 425-448.
3. Bola, J. S., Popli, H., Stolley, R. M., Liu, H., Malissa, H., Kwon, O., Boehme, C., Miller, J. S., & Vardeny, Z. V. (2021). Fabrication method, ferromagnetic resonance spectroscopy and spintronics devices based on the organic-based ferrimagnet vanadium tetracyanoethylene. Advanced Functional Materials, 31(30), 2100687.
4. Blundell, S. J. (2002). Magnetism in polymeric fullerenes: A new route to organic magnetism? Journal of Physics: Condensed Matter, 14(22), V1-V3.
5. Miyasaka, H., & Yamashita, M. (2007). A look at molecular nanosized magnets from the aspect of inter-molecular interactions. Dalton Transactions, 4, 399-406.
6. Christou, G., Gatteschi, D., Hendrickson, D. N., & Sessoli, R. (2000). Single-molecule magnets. MRS Bulletin, 25(11), 66-71.
7. Troiani, F., & Affronte, M. (2011). Molecular spins for quantum information technologies. Chemical Society Reviews, 40(6), 3119-3129.
8. Rabelo, R., Stiriba, S. E., Cangussu, D., Pereira, C. L. M., Moliner, N., Ruiz-García, R., Cano, J., Faus, J., Journaux, Y., & Julve, M. (2020). When molecular magnetism meets supramolecular chemistry: Multifunctional and multiresponsive dicopper (II) metallacyclophanes as proof-of-concept for single-molecule spintronics and quantum computing technologies? Magnetochemistry, 6(4), 69.
9. Ollier, A., Kisiel, M., Lu, X., Gysin, U., Poggio, M., Efetov, D. K., & Meyer, E. (2023). Energy dissipation on magic angle twisted bilayer graphene. Communications Physics, 6(1), 344.
10. Chichinadze, D. V., Classen, L., & Chubukov, A. V. (2020). Nematic superconductivity in twisted bilayer graphene. Physical Review B, 101(22), 224513.
11. Ranade, V., Gautam, S., & Chae, K. H. (2023). Magnetism in carbon-based fiber materials. Journal of Magnetism and Magnetic Materials.
12. Guo, J., Jiang, H., Teng, Y., Xiong, Y., Chen, Z., You, L., & Xiao, D. (2021). Recent advances in magnetic carbon nanotubes: Synthesis, challenges and highlighted applications. Journal of Materials Chemistry B, 9(44), 9076-9099.

13. Polshyn, H., Yankowitz, M., Chen, S., Zhang, Y., Watanabe, K., Taniguchi, T., Dean, C. R., & Young, A. F. (2019). Large linear-in-temperature resistivity in twisted bilayer graphene. Nature Physics, 15(10), 1011-1016.
14. Cao, Y., Fatemi, V., Fang, S., Watanabe, K., Taniguchi, T., Kaxiras, E., & Jarillo-Herrero, P. (2018). Unconventional superconductivity in magic-angle graphene superlattices. Nature, 556(7699), 43-50.
15. Guinea, F., & Walet, N. R. (2018). Electrostatic effects, band distortions, and superconductivity in twisted graphene bilayers. Proceedings of the National Academy of Sciences, 115(52), 13174-13179.
16. Tanaka, A., & Sasaki, T. (2015). Focus on materials science of topological insulators and superconductors. Science and Technology of Advanced Materials.
17. Tokura, Y., Yasuda, K., & Tsukazaki, A. (2019). Magnetic topological insulators. Nature Reviews Physics, 1(2), 126-143.
18. Geim, A. K., & Novoselov, K. S. (2007). The rise of graphene. *Nature Materials, 6*(3), 183-191.
19. Castro Neto, A. H., Guinea, F., Peres, N. M. R., Novoselov, K. S., & Geim, A. K. (2009). The electronic properties of graphene. *Reviews of Modern Physics, 81*(1), 109-162.
20. Nobel Prize in Physics. (2010). Graphene discovery. Retrieved from https://www.nobelprize.org/prizes/physics/2010/summary/
21. Allen, M. J., Tung, V. C., & Kaner, R. B. (2010). Honeycomb carbon: A review of graphene. *Chemical Reviews, 110*(1), 132-145.
22. Wallace, P. R. (1947). The band theory of graphite. *Physical Review, 71*(9), 622-634.
23. Peres, N. M. R. (2010). The transport properties of graphene: An introduction. *Reviews of Modern Physics, 82*(3), 2673–2700.
24. Yazyev, O. V. (2010). Emergence of magnetism in graphene materials and nanostructures. *Reports on Progress in Physics, 73*(5), 056501.
25. Novoselov, K. S., Geim, A. K., Morozov, S. V., Jiang, D., Katsnelson, M. I., Grigorieva, I. V., Dubonos, S. V., & Firsov, A. A. (2005). Two-dimensional gas of massless Dirac fermions in graphene. *Nature, 438*(7065), 197–200.
26. Santos, E. J. G., Ayuela, A., & Sanchez-Portal, D. (2012). Magnetism of graphene nanostructures. *Physical Chemistry Chemical Physics, 14*(47), 16369-16376.

27. Nair, R. R., Sepioni, M., Tsai, I. L., Lehtinen, O., Keinonen, J., Krasheninnikov, A. V., Thomson, T., Geim, A. K., & Grigorieva, I. V. (2012). Spin-half paramagnetism in graphene induced by point defects. *Nature Physics, 8*(3), 199-202.
28. Han, K. H., Kwon, H. J., Kim, S. K., Ryu, S., & Yun, W. S. (2014). Inducing magnetic ordering in graphene nanoribbons through selective doping. *Nano Letters, 14*(8), 4446-4453.
29. Lieb, E. H. (1989). Two theorems on the Hubbard model. *Physical Review Letters, 62*(10), 1201-1204.
30. Terrones, H., Terrones, M., Charlier, J. C., Banhart, F., & Ajayan, P. M. (2012). New directions in nanotube science. *Materials Today, 15*(9), 348-358.
31. Coey, J. M. D., & Sanvito, S. (2010). Magnetism in graphene. *Journal of Physics: Condensed Matter, 22*(16), 164208.
32. Nkou, F. B. S., Douma, D. H., Malonda Boungou, B. R., Raji, A. T., Kenmoe, S., & M'Passi Mabiala, B. (2021). Theoretical insights into magnetization in graphene containing single and interacting nanoporous defects. *Physica E: Low-dimensional Systems and Nanostructures, 124*, 114311.
33. Friedrich, N., Menchón, R. E., Pozo, I., Hieulle, J., Vegliante, A., Li, J., Sánchez-Portal, D., Peña, D., Garcia-Lekue, A., & Pascual, J. I. (2022). Addressing electron spins embedded in metallic graphene nanoribbons. *ACS Nano, 16*(9), 14819–14826.
34. Pan, M., & Yuan, H. (2020). Experimental observation of low-dimensional magnetism in graphene nanostructures. *Nature, 580*(7802), 437-440.
35. Pavliček, N., Mistry, A., Majzik, Z., Moll, N., Meyer, G., Fox, D. J., & Gross, L. (2017). Synthesis and characterization of triangulene. *Nature Nanotechnology, 12*(4), 308-311.
36. Mishra, S., Beyer, D., Eimre, K., Liu, J., Berger, R., Gröning, O., & Ruffieux, P. (2019). Synthesis and characterization of π-extended triangulene. *Journal of the American Chemical Society, 141*(27), 10621-10625.
37. Mishra, S., Beyer, D., Eimre, K., Ortiz, R., Fernández-Rossier, J., Berger, R., & Ruffieux, P. (2020). Collective all-carbon magnetism in triangulene dimers. *Angewandte Chemie, 132*(29), 12139-12145.
38. Mishra, S., Beyer, D., Eimre, K., Kezilebieke, S., Berger, R., Gröning, O., & Fasel, R. (2020). Topological frustration induces unconventional magnetism in a nanographene. *Nature Nanotechnology, 15*(1), 22-28.

39. Clar, E. (1983). The aromatic sextet. In *Mobile source emissions including polycyclic organic species* (pp. 49-58). Dordrecht: Springer Netherlands.
40. Wang, T., Berdonces-Layunta, A., Friedrich, N., Vilas-Varela, M., Calupitan, J. P., Pascual, J. I., & de Oteyza, D. G. (2022). Aza-triangulene: On-surface synthesis and electronic and magnetic properties. *Journal of the American Chemical Society, 144*(10), 4522-4529.
41. Magda, G., Jin, X., Hagymási, I., Vancsó, P., Osváth, Z., Nemes-Incze, P., Hwang, C., Biró, L., & Tapasztó, L. (2014). Room-temperature magnetic order on zigzag edges of narrow graphene nanoribbons. *Nature, 514*(7524), 608-611.
42. Xu, K., & Ye, P. (2014). Electron spin magnetism of zigzag graphene nanoribbon edge states. *Applied Physics Letters, 104*(16), 163104.
43. Conrad, L., Alcón, I., Tremblay, J. C., & Paulus, B. (2023). Mechanistic insights into electronic current flow through quinone devices. *Nanomaterials, 13*(4), 833.
44. Gordeev, E., Pentsak, E. O., & Ananikov, V. P. (2020). Carbocatalytic acetylene cyclotrimerization: A key role of unpaired electron delocalization. *Journal of the American Chemical Society, 142*(6), 2628-2637.
45. Mishra, S., Lohr, T. G., Pignedoli, C., Liu, J., Berger, R., Urgel, J. I., Müllen, K., Feng, X., Ruffieux, P., & Fasel, R. (2018). Tailoring bond topologies in open-shell graphene nanostructures. *ACS Nano, 12*(12), 11917-11927.
46. Sun, Q., Yao, X., Gröning, O., Eimre, K., Pignedoli, C. A., Müllen, K., Narita, A., Fasel, R., & Ruffieux, P. (2020). Coupled spin states in armchair graphene nanoribbons with asymmetric zigzag edge extensions. *Nano Letters, 20*(9), 6429-6436.
47. Friedrich, N., Brandimarte, P., Li, J., Saito, S., Yamaguchi, S., Pozo, I., Peña, D., Frederiksen, T., Garcia-Lekue, A., Sánchez-Portal, D., & Pascual, J. I. (2020). Magnetism of topological boundary states induced by boron substitution in graphene nanoribbons. *Physical Review Letters, 125*(14), 146801.
48. Sharpe, A. L., Fox, E. J., Barnard, A. W., Finney, J., Watanabe, K., Taniguchi, T., Kastner, M. A., & Goldhaber-Gordon, D. (2019). Emergent ferromagnetism near three-quarters filling in twisted bilayer graphene. *Science, 365*(6453), 605-608.
49. Jing, Y., & Heine, T. (2019). Two-dimensional kagome lattices made of hetero triangulenes are Dirac semimetals or single-band semiconductors. *Journal of the American Chemical Society, 141*(2), 743-747.

50. Galeotti, G., De Marchi, F., Hamzehpoor, E., MacLean, O., Rajeswara Rao, M., Chen, Y., Besteiro, L. V., Dettmann, D., Ferrari, L., Frezza, F., Sheverdyaeva, P. M., Liu, R., Kundu, A. K., Moras, P., Ebrahimi, M., Gallagher, M. C., Rosei, F., Perepichka, D. F., & Contini, G. (2020). Synthesis of mesoscale ordered two-dimensional π-conjugated polymers with semiconducting properties. *Nature Materials, 19*(8), 874-880.
51. Thomas, S., Li, H., & Brédas, J. L. (2019). Emergence of an antiferromagnetic Mott insulating phase in hexagonal π-conjugated covalent organic frameworks. *Advanced Materials, 31*(17), 1900355.
52. He, S., Zhou, P., Yang, Y., Wang, W., & Sun, L. Z. (2021). 1T-$CrO_2$ monolayer: A high-temperature Dirac half-metal for high-speed spintronics. *Nanoscale Advances, 3*(11), 3093-3099.
53. Si, N., Su, X., Meng, J., Miao, H., Zhang, Y., & Jiang, W. (2020). Magnetic properties of decorated 2D kagome-like lattice. *Physica A: Statistical Mechanics and Its Applications, 560*, 125222.
54. Guo, J. (2019). Performance potential of 2D kagome lattice interconnects. *IEEE Electron Device Letters, 40*(12), 1973-1975.
55. Giannozzi, P., Baroni, S., Bonini, N., Calandra, M., Car, R., Cavazzoni, C., Ceresoli, D., Chiarotti, G. L., Cococcioni, M., Dabo, I., Dal Corso, A., de Gironcoli, S., Fabris, S., Fratesi, G., Gebauer, R., Gerstmann, U., Gougoussis, C., Kokalj, A., Lazzeri, M., ... & Wentzcovitch, R. M. (2009). QUANTUM ESPRESSO: A modular and open-source software project for quantum simulations of materials. *Journal of Physics: Condensed Matter, 21*(39), 395502.
56. Blöchl, P. E. (1994). Projector augmented-wave method. *Physical Review B, 50*(24), 17953-17979.
57. Kohn, W., & Sham, L. J. (1965). Self-consistent equations including exchange and correlation effects. *Physical Review, 140*(4A), A1133–A1138.
58. Martin, R. M. (2004). Electronic structure: Basic theory and practical methods. Cambridge University Press.
59. Cococcioni, M., & de Gironcoli, S. (2005). Linear response approach to the calculation of the effective interaction parameters in the LDA+U method. *Physical Review B, 71*(3), 035105.
60. Perdew, J. P. (1985). Density functional theory and the band gap problem. *International Journal of Quantum Chemistry, 28*(S19), 497-523.

61. Adamo, C., & Barone, V. (1999). Toward reliable density functional methods without adjustable parameters: The PBE0 model. *The Journal of Chemical Physics, 110*(13), 6158–6170.

62. Xu, Z., Joshi, Y. V., Raman, S., & Kitchin, J. (2015). Accurate electronic and chemical properties of 3d transition metal oxides using a calculated linear response U and a DFT + U(V) method. *The Journal of Chemical Physics, 142*(14), 144701.

63. Miwa, K. (2018). Prediction of Raman spectra with DFT+U method. *Physical Review B, 97*(7), 075143.

64. Kane, C. L., & Mele, E. J. (2005). Z2 topological order and the quantum spin Hall effect. *Physical Review Letters*, 95(14), 146802.

65. Kane, C. L., & Mele, E. J. (2005). Quantum spin Hall effect in graphene. *Physical Review Letters*, 95(22), 226801.

66. Cao, T., Zhao, F., & Louie, S. G. (2017). Topological phases in graphene nanoribbons: Junction states, spin centers, and quantum spin chains. *Physical Review Letters*, 119(7), 076401.

67. Rizzo, D. J., Veber, G., Cao, T., Bronner, C., Chen, T., Zhao, F., Rodriguez, H., Louie, S. G., Crommie, M. F., & Fischer, F. R. (2018). Topological band engineering of graphene nanoribbons. *Nature*, 560(7717), 204–208.

68. Droth, M., & Burkard, G. (2016). Spintronics with graphene quantum dots. *Physica Status Solidi (RRL) – Rapid Research Letters*, 10(1), 75–90.

69. Balasubramanian, G., Neumann, P., Twitchen, D., Markham, M., Kolesov, R., Mizuochi, N., Isoya, J., Achard, J., Beck, J., & Tissler, J. (2009). Ultralong spin coherence time in isotopically engineered diamond. *Nature Materials*, 8(5), 383–387.

70. Ruffieux, P., Wang, S., Yang, B., Sánchez-Sánchez, C., Liu, J., Dienel, T., Talirz, L., Shinde, P., Pignedoli, C. A., Passerone, D., Dumslaff, T., Feng, X., Mullen, K., & Fasel, R. (2016). On-surface synthesis of graphene nanoribbons with zigzag edge topology. *Nature*, 531(7595), 489–492.

71. Narita, A., Feng, X., Hernandez, Y., Jensen, S. A., Bonn, M., Yang, H., Verzhbitskiy, I. A., Casiraghi, C., Hansen, M. R., Koch, A. H. R., Fytas, G., & Mullen, K. (2014). Synthesis of

structurally well-defined and liquid-phase-processable graphene nanoribbons. *Nature Chemistry*, 6(2), 126–132.

72. Coey, M., & Sanvito, S. (2004). The magnetism of carbon. *Physics World*, 17(11), 33.

73. Son, Y.-W., Cohen, M. L., & Louie, S. G. (2006). Half-metallic graphene nanoribbons. *Nature*, 444(7117), 347–349.

74. Yang, L., Park, C.-H., Son, Y.-W., Cohen, M. L., & Louie, S. G. (2007). Quasiparticle energies and band gaps in graphene nanoribbons. *Physical Review Letters*, 99(18), 186801.

75. Blackwell, R. E., Zhao, F., Brooks, E., Zhu, J., Piskun, I., Wang, S., Delgado, A., Lee, Y.-L., Louie, S. G., & Fischer, F. R. (2021). Spin splitting of dopant edge state in magnetic zigzag graphene nanoribbons. *Nature*, 600(7890), 647–652.

76. Kunstmann, J., Özdoğan, C., Quandt, A., & Fehske, H. (2011). Stability of edge states and edge magnetism in graphene nanoribbons. *Physical Review B*, 83(4), 045414.

77. Lawrence, J., Berdonces-Layunta, A., Edalatmanesh, S., Castro-Esteban, J., Wang, T., Jimenez-Martin, A., de la Torre, B., Castrillo-Bodero, R., Angulo-Portugal, P., Mohammed, M. S. G., Rogero, C., de Oteyza, D. G., Sanchez-Portal, D., Pascual, J. I., & Cirera, J. (2022). Circumventing the stability problems of graphene nanoribbon zigzag edges. *Nature Chemistry*, 14(12), 1451–1458.

78. Zhang, J., Ragab, T., & Basaran, C. (2019). Comparison of fracture behavior of defective armchair and zigzag graphene nanoribbons. *International Journal of Damage Mechanics*, 28(3), 325–345.

79. Kimouche, A., Ervasti, M. M., Drost, R., Halonen, S., Harju, A., Joensuu, P. M., Sainio, J., & Liljeroth, P. (2015). Ultra-narrow metallic armchair graphene nanoribbons. *Nature Communications*, 6, 10177.

80. Pan, Y., & Yang, Z. (2011). Exploration of magnetism in armchair graphene nanoribbons with radical groups. *Chemical Physics Letters*, 518, 104–108.

81. Lieb, E. H. (1989). Two theorems on the Hubbard model. *Physical Review Letters*, 62(10), 1201–1204.

82. Mishra, S., Beyer, D., Berger, R., Liu, J., Gröning, O., Urgel, J. I., Müllen, K., Ruffieux, P., Feng, X., & Fasel, R. (2020). Topological defect-induced magnetism in a nanographene. *Journal of the American Chemical Society*, 142(3), 1147–1152.

83. Lahiri, J., Lin, Y., Bozkurt, P., Oleynik, I. I., & Batzill, M. (2010). An extended defect in graphene as a metallic wire. *Nature Nanotechnology*, 5(5), 326–329.

84. Yazyev, O. V., & Louie, S. G. (2010). Electronic transport in polycrystalline graphene. *Nature Materials*, 9(10), 806–809.

85. Cretu, O., Krasheninnikov, A. V., Rodríguez-Manzo, J. A., Sun, L., Nieminen, R. M., & Banhart, F. (2010). Migration and localization of metal atoms on strained graphene. *Physical Review Letters*, 105(19), 196102.

86. Bhatt, M. D., Kim, H., & Kim, G. (2022). Various defects in graphene: A review. *RSC Advances*, 12(37), 21520–21547.

87. Wakabayashi, K., Okada, S., Tomita, R., Fujimoto, S., & Natsume, Y. (2010). Edge states and flat bands of graphene nanoribbons with edge modification. *Journal of the Physical Society of Japan*, 79(3), 034706.

88. Friedrich, N., Brandimarte, P., Li, J., Saito, S., Yamaguchi, S., Pozo, I., Peña, D., Frederiksen, T., Garcia-Lekue, A., & Sánchez-Portal, D. (2020). Magnetism of topological boundary states induced by boron substitution in graphene nanoribbons. *Physical Review Letters*, 125(14), 146801.

89. Barth, J. V., Costantini, G., & Kern, K. (2005). Engineering atomic and molecular nanostructures at surfaces. *Nature*, 437(7059), 671–679.

90. Lin, N., & Barth, J. V. (2008). Surface-confined supramolecular coordination chemistry. *Topics in Current Chemistry*, 287, 1–44.

91. Dong, L., Gao, Z., & Lin, N. (2016). Self-assembly of metal–organic coordination structures on surfaces. *Progress in Surface Science*, 91(2), 101–135.

92. Clair, S., & de Oteyza, D. G. (2019). Controlling a chemical coupling reaction on a surface: Tools and strategies for on-surface synthesis. *Chemical Reviews*, 119(7), 4717–4776.

93. Pawlak, R., Anindya, K. N., Shimizu, T., Liu, J.-C., Sakamaki, T., Shang, R., Rochefort, A., Nakamura, E., & Meyer, E. (2022). Atomically precise incorporation of BN-doped rubicene into graphene nanoribbons. *The Journal of Physical Chemistry C*, 126(45), 19726–19733.

94. Rizzo, D. J., Veber, G., Jiang, J., McCurdy, R., Cao, T., Bronner, C., Chen, T., Louie, S. G., Fischer, F. R., & Crommie, M. F. (2020). Inducing metallicity in graphene nanoribbons via zero-mode superlattices. *Science*, 369(6506), 1597–1603.

95. Kawai, S., Saito, S., Osumi, S., Yamaguchi, S., Foster, A. S., Spijker, P., & Meyer, E. (2015). Atomically controlled substitutional boron-doping of graphene nanoribbons. *Nature Communications*, 6, 8098.

96. Perdew, J. P., Burke, K., & Ernzerhof, M. (1996). Generalized gradient approximation made simple. *Physical Review Letters*, 77(18), 3865–3868.

97. Giannozzi, P., Andreussi, O., Brumme, T., Bunau, O., Nardelli, M. B., Calandra, M., Car, R., Cavazzoni, C., Ceresoli, D., Cococcioni, M., et al. (2017). Advanced capabilities for materials modelling with Quantum ESPRESSO. *Journal of Physics: Condensed Matter*, 29(46), 465901.

98. Anindya, K. N., & Rochefort, A. (2022). Controlling the magnetic properties of two-dimensional carbon-based Kagome polymers. *Carbon Trends*, 7, 100170.

99. Mosey, N. J., & Carter, E. A. (2007). Ab initio evaluation of Coulomb and exchange parameters for DFT+U calculations. *Physical Review B*, 76(15), 155123.

100. Grimme, S. (2006). Semiempirical GGA-type density functional constructed with a long-range dispersion correction. *Journal of Computational Chemistry*, 27(15), 1787–1799.

101. Blöchl, P. E. (1994). Projector augmented-wave method. *Physical Review B*, 50(24), 17953–17979.

102. Hapala, P., Kichin, G., Wagner, C., Tautz, F. S., Temirov, R., & Jelínek, P. (2014). Mechanism of high-resolution STM/AFM imaging with functionalized tips. *Physical Review B*, 90(8), 085421.

103. Wang, T., Berdonces-Layunta, A., Friedrich, N., Vilas-Varela, M., Calupitan, J. P., Pascual, J. I., Peña, D., Casanova, D., Corso, M., & de Oteyza, D. G. (2022). Aza-triangulene: On-

surface synthesis and electronic and magnetic properties. *Journal of the American Chemical Society*, 144(11), 4522–4529.

104. Wang, X., Sun, G., Routh, P., Kim, D.-H., Huang, W., & Chen, P. (2014). Heteroatom-doped graphene materials: Syntheses, properties and applications. *Chemical Society Reviews*, 43(20), 7067–7098.

105. Li, J., Sanz, S., Castro-Esteban, J., Vilas-Varela, M., Friedrich, N., Frederiksen, T., Peña, D., & Pascual, J. I. (2020). Uncovering the triplet ground state of triangular graphene nanoflakes engineered with atomic precision on a metal surface. *Physical Review Letters*, 124(17), 177201.

106. Mishra, S., Beyer, D., Eimre, K., Ortiz, R., Fernandez-Rossier, J., Berger, R., Gröning, O., Pignedoli, C. A., Fasel, R., Feng, X., & Ruffieux, P. (2020). Collective all-carbon magnetism in triangulene dimers. *Angewandte Chemie International Edition*, 59(30), 12041–12047.

107. Ishii, A., Shiotari, A., & Sugimoto, Y. (2020). Quality control of on-surface-synthesised seven-atom wide armchair graphene nanoribbons. *Nanoscale*, 12(13), 6651–6657.

108. Hieulle, J., Castro, S., Friedrich, N., Vegliante, A., Lara, F. R., Sanz, S., Rey, D., Corso, M., Frederiksen, T., Pascual, J. I., & Peña, D. (2021). On-surface synthesis and collective spin excitations of a triangulene-based nanostar. *Angewandte Chemie International Edition, 60(48)*, 25224-25229.

109. Su, J., Telychko, M., Hu, P., Macam, G., Mutombo, P., Zhang, H., Bao, Y., Cheng, F., Huang, Z.-Q., Qiu, Z., Tan, S. J. R., Lin, H., Jelínek, P., Chuang, F.-C., Wu, J., & Lu, J. (2019). Atomically precise bottom-up synthesis of π-extended triangulene. *Science Advances, 5(7)*, eaav7717.

110. Mishra, S., Xu, K., Eimre, K., Komber, H., Ma, J., Pignedoli, C. A., Fasel, R., Feng, X., & Ruffieux, P. (2021). Synthesis and characterization of [7]triangulene. *Nanoscale, 13(3)*, 1624-1628.

111. Adjizian, J.-J., Briddon, P., Humbert, B., Duvail, J.-L., Wagner, P., Adda, C., & Ewels, C. (2014). Dirac cones in two-dimensional conjugated polymer networks. *Nature Communications, 5(1)*, 5842.

112. Jing, Y., & Heine, T. (2020). Making 2D topological polymers a reality. *Nature Materials, 19(8)*, 823-824.

113. Springer, M. A., Liu, T.-J., Kuc, A., & Heine, T. (2020). Topological two-dimensional polymers. *Chemical Society Reviews, 49(7)*, 2007-2019.

114. Steiner, C., Gebhardt, J., Ammon, M., Yang, Z., Heidenreich, A., Hammer, N., Görling, A., Kivala, M., & Maier, S. (2017). Hierarchical on-surface synthesis and electronic structure of carbonyl-functionalized one- and two-dimensional covalent nanoarchitectures. *Nature Communications, 8(1)*, 14765.

115. Maruyama, M., Cuong, N. T., & Okada, S. (2016). Coexistence of Dirac cones and Kagome flat bands in a porous graphene. *Carbon, 109*, 755-763.

116. Sandoval-Salinas, M. E., Carreras, A., & Casanova, D. (2019). Triangular graphene nanofragments: open-shell character and doping. *Physical Chemistry Chemical Physics, 21(18)*, 9069-9076.

117. Ovchinnikov, A. A. (1978). Multiplicity of the ground state of large alternant organic molecules with conjugated bonds. *Theoretical Chemistry Accounts, 47(4)*, 297-304.

118. Fernández-Rossier, J., & Palacios, J. J. (2007). Magnetism in graphene nanoislands. *Physical Review Letters, 99(17)*, 177204.

119. Xiang, H., Lee, C., Koo, H.-J., Gong, X., & Whangbo, M.-H. (2012). Magnetic properties and energy-mapping analysis. *Dalton Transactions, 42(4)*, 823-853.

120. Head-Gordon, M. (2003). Characterizing unpaired electrons from the one-particle density matrix. *Chemical Physics Letters, 372*, 508-511.

121. Meng, Z. Y., Lang, T. C., Wessel, S., Assaad, F. F., & Muramatsu, A. (2010). Quantum spin liquid emerging in two-dimensional correlated Dirac fermions. *Nature, 464(7290)*, 847-851.

122. Alcón, I., Viñes, F., de P. R., M. I., & Bromley, S. T. (2017). Existence of multi-radical and closed-shell semiconducting states in post-graphene organic Dirac materials. *Nature Communications, 8(1)*, 1957.

123. Roy, S. B. (2019). *Mott Insulators: Physics and Applications*. IOP Publishing.

124. Makarova, T., & Palacio, F. (2006). Carbon-based magnetism: An overview of the magnetism of metal-free carbon-based compounds and materials. *Elsevier*.

125. Springer, M. A., Liu, T.-J., Kuc, A., & Heine, T. (2020). Topological two-dimensional polymers. *Chemical Society Reviews*, 49, 2007.

126. Steiner, C., Gebhardt, J., Ammon, M., Yang, Z., Heidenreich, A., Hammer, N., Görling, A., Kivala, M., & Maier, S. (2017). Hierarchical on-surface synthesis and electronic structure of carbonyl-functionalized one- and two-dimensional covalent nanoarchitectures. *Nature Communications*, 8, 14765.

127. Liu, Z., Wang, Z. F., Mei, J. W., Wu, Y. S., & Liu, F. (2013). Flat Chern band in a two-dimensional organometallic framework. *Physical Review Letters*, 110, 106804.

128. Maruyama, M., & Okada, S. (2018). Energetics and electronic structure of triangular hexagonal boron nitride nanoflakes. *Scientific Reports*, 8, 16657.

129. Viana, G. E. D., Silva, A. M., Barros, F. U. da C., da Silva, F. J. A. M., Caetano, E. W. S., Melo, J. J. S., & Macedo-Filho, A. (2020). Thermal stability and electronic properties of boron nitride nanoflakes. *Journal of Molecular Modeling*, 26, 100.

130. Xi, Y., Zhao, X., Wang, A., Wang, X., Bu, H., & Zhao, M. (2013). Tuning the electronic and magnetic properties of triangular boron nitride quantum dots via carbon doping. *Physica E: Low-Dimensional Systems and Nanostructures*, 49, 52.

131. Mokkath, J. H., & Schwingenschlögl, U. (2014). Tuning the optical response in carbon-doped boron nitride nanodots. *Journal of Materials Chemistry C*, 2, 8322.

132. Du, A. J., Smith, S. C., & Lu, G. Q. (2007). First-principle studies of electronic structure and C-doping effect in boron nitride nanoribbon. *Chemical Physics Letters*, 447, 181.

133. Tang, S., & Cao, Z. (2010). Carbon-doped zigzag boron nitride nanoribbons with widely tunable electronic and magnetic properties: Insight from density functional calculations. *Physical Chemistry Chemical Physics*, 12, 2313.

134. Huang, B., Lee, H., Gu, B. L., Liu, F., & Duan, W. (2012). Edge stability of boron nitride nanoribbons and its application in designing hybrid BNC structures. *Nano Research*, 5, 62.

135. Li, X., Wu, X., Zeng, X. C., & Yang, J. (2012). Band-gap engineering via tailored line defects in boron-nitride nanoribbons, sheets, and nanotubes. *ACS Nano*, 6, 4104.

136. Wu, R. Q., Liu, L., Peng, G. W., & Feng, Y. P. (2005). Magnetism in BN nanotubes induced by carbon doping. *Applied Physics Letters*, 86, 122510.

137. Hao, S., Zhou, G., Duan, W., Wu, J., & Gu, B. L. (2006). Tremendous spin-splitting effects in open boron nitride nanotubes: Application to nanoscale spintronic devices. *Journal of the American Chemical Society*, 128, 8453.

138. Zhou, G., & Duan, W. (2007). Spin-polarized electron current from carbon-doped open armchair boron nitride nanotubes: Implication for nano-spintronic devices. *Chemical Physics Letters*, 437, 83.

139. Guan, Z., Wang, W., Huang, J., Wu, X., Li, Q., & Yang, J. (2014). Tunable electronic and magnetic properties of graphene flake-doped boron nitride nanotubes. *Journal of Physical Chemistry C*, 118, 28616.

140. Wu, R. Q., Peng, G. W., Liu, L., & Feng, Y. P. (2005). Possible graphitic-boron-nitride-based metal-free molecular magnets from first principles study. *Journal of Physics: Condensed Matter*, 18, 569.

141. Zhao, C., Xu, Z., Wang, H., Wei, J., Wang, W., Bai, X., & Wang, E. (2014). Carbon-doped boron nitride nanosheets with ferromagnetism above room temperature. *Advanced Functional Materials*, 24, 5985.

142. Choudhuri, I., & Pathak, B. (2018). Ferromagnetism and half-metallicity in a high-band-gap hexagonal boron nitride system. *ChemPhysChem*, 19, 153.

143. Fan, M., Wu, J., Yuan, J., Deng, L., Zhong, N., He, L., Cui, J., Wang, Z., Behera, S. K., Zhang, C., Lai, J., Jawdat, B. I., Vajtai, R., Deb, P., Huang, Y., Qian, J., Yang, J., Tour, J. M., Lou, J., Chu, C.-W., Sun, D., & Ajayan, P. M. (2019). Doping nanoscale graphene domains improves magnetism in hexagonal boron nitride. *Advanced Materials*, 31, 1805778.

144. Liu, W., Yanase, T., Nagahama, T., & Shimada, T. (2019). Synthesis of carbon-doped boron nitride nanosheets and enhancement of their room-temperature ferromagnetic properties. *Journal of Alloys and Compounds*, 792, 1206.

145. Liu, N., Gao, G. Y., Zhu, S. C., Ni, Y., Wang, S. L., Liu, J. B., & Yao, K. L. (2014). Carbon doping induced peculiar transport properties of boron nitride nanoribbons p-n junctions. *Journal of Applied Physics*, 116, 023708.

146. Valiev, M., Bylaska, E. J., Govind, N., Kowalski, K., Straatsma, T. P., Van Dam, H. J. J., Wang, D., Nieplocha, J., Apra, E., Windus, T. L., & de Jong, W. A. (2010). NWChem: A comprehensive and scalable open-source solution for large scale molecular simulations. *Computer Physics Communications*, 181, 1477.

147. Monkhorst, H. J., & Pack, J. D. (1976). Special points for Brillouin-zone integrations. *Physical Review B*, 13, 5188.

148. Pettersen, E. F., Goddard, T. D., Huang, C. C., Couch, G. S., Greenblatt, D. M., Meng, E. C., & Ferrin, T. E. (2004). UCSF Chimera: A visualization system for exploratory research and analysis. *Journal of Computational Chemistry*, 25, 1605.

149. Momma, K., & Izumi, F. (2011). VESTA 3 for three-dimensional visualization of crystal, volumetric and morphology data. *Journal of Applied Crystallography*, 44, 1272.

150. Leykam, D., Andreanov, A., & Flach, S. (2018). Artificial flat band systems: From lattice models to experiments. *Advances in Physics: X*, 3, 1473052.

# APPENDIX A Supplementary Information of Chapter 4- SPIN-POLARIZED TOPOLOGICAL PHASES IN GRAPHENE NANORIBBONS WITH NON-BENZENOID DEFECTS

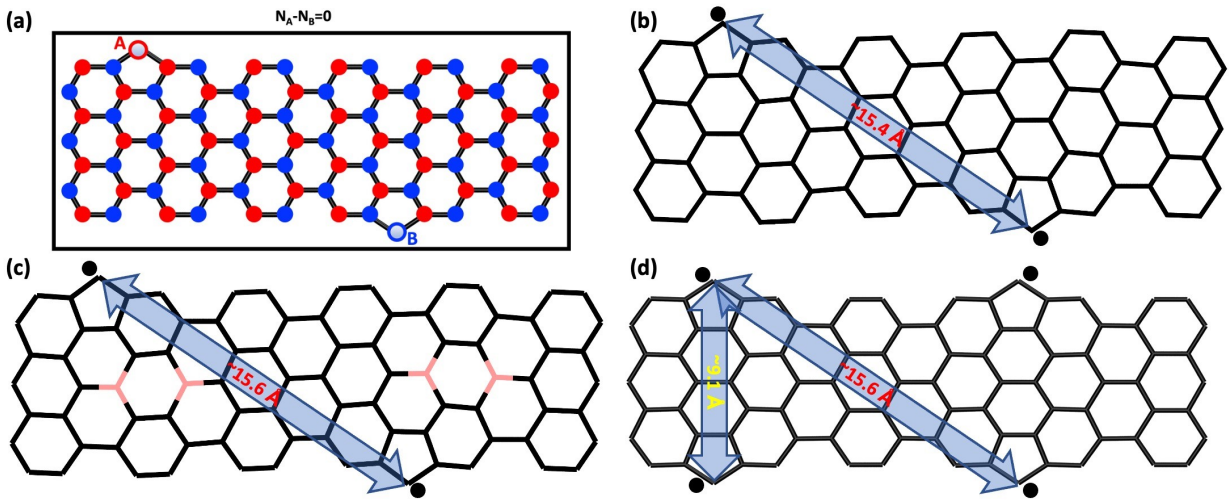


Figure S1: (a) Schematic representation of different sublattices of P-GNR. Distances between the pentagonal atomic site has been indicated for different species; (b) P-GNR, (c) P-BGNR and (d) s-P-GNR.

**Computational details:**

The unit cells of both freestanding P-GNR and P-BGNR comprise a total of 108 atoms. In these unit cells, 86 atoms are carbon, and 22 are hydrogen for all carbon-based P-GNR structures. However, in the case of P-BGNR, 4 boron atoms substitute for the carbon atoms. Furthermore, when examining scenarios involving adsorption on Au(111), we have taken into account a three-layer gold substrate composed of 192 Au atoms. Following our DFT+U approach, we were able to reproduce the DM state bands for sGNR and B-doped 7-AGNR (7-BGNR) from previous studies as shown in Figure S2(a) and S2(b).[1,2] In addition, to better justify our DFT+U approach against experimental and PBE0 method, we computed the bandgap of antiferromagnetic state of finite length 7-AGNR (of length 12) as tabulated in Table S2. We found almost similar bandgaps using our DFT+U method compared to PBE0[3] and experimental[4] findings.

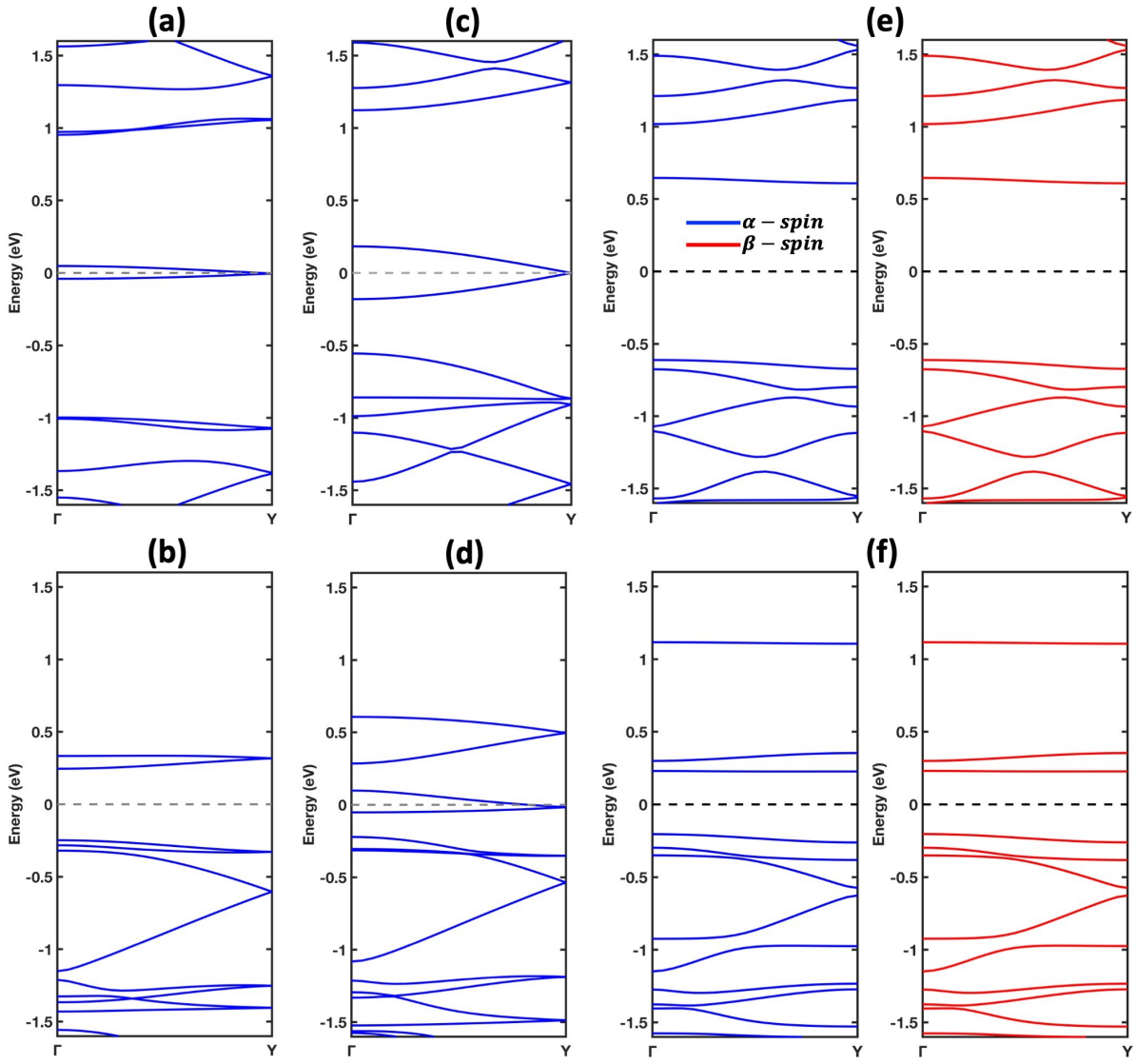


Figure S2: DM state band-structures for (a) sawtooth-GNR, (b) 7-BGNR, (c) P-GNR and (d) P-BGNR. In addition, spin degenerate bands of AFeM state has been plotted for (e) P-GNR and (f) P-BGNR.

Table S1: Electronic and magnetic properties of different freestanding and adsorbed sGNRs calculated at DFT+U level. The band gap value Eg is estimated from |$\varepsilon$HOMO − $\varepsilon$LUMO|.

| GNRType | $\Delta E$/unitcell(meV) [a] | | $E_g$ (eV)[b] | | $\lvert m \rvert$ ($\mu_B$)[c] |
|---|---|---|---|---|---|
| | FeM | DM | FeM | | |
| | | | $\alpha$ | $\beta$ | |
| sGNR | 0 | 565 | 1.53 | 1.51 | 12.13(2.00) |
| sGNR/Au | 0 | 327 | - | - | 10.22(1.84) |

[a] Relative energy of DM phase with respect to the total energy of the FeM ground state (0 eV). [b] Semiconducting band gap. ”-” sign is used for substrate adsorbed cases. [c] Total absolute magnetization per unit cell in their corresponding ground state. Values between parenthesis are the actual magnetic moments.

Table S2: Energy bandgaps of antiferromagnetic finite length 7-AGNR (of length 12) from different studies. The band gap value Eg is estimated from |$\varepsilon$HOMO − $\varepsilon$LUMO|.

| GNRType | $\Delta E$ (eV)[a] | | |
|---|---|---|---|
| | DFT+U | PBE0fromRef3 [3] | ExperimentalfromRef4 [4] |
| 7-AGNR | 1.82 | 1.9 | 1.9 |

[a] Band gap values for degenerate bands for both spins in AFeM phase.

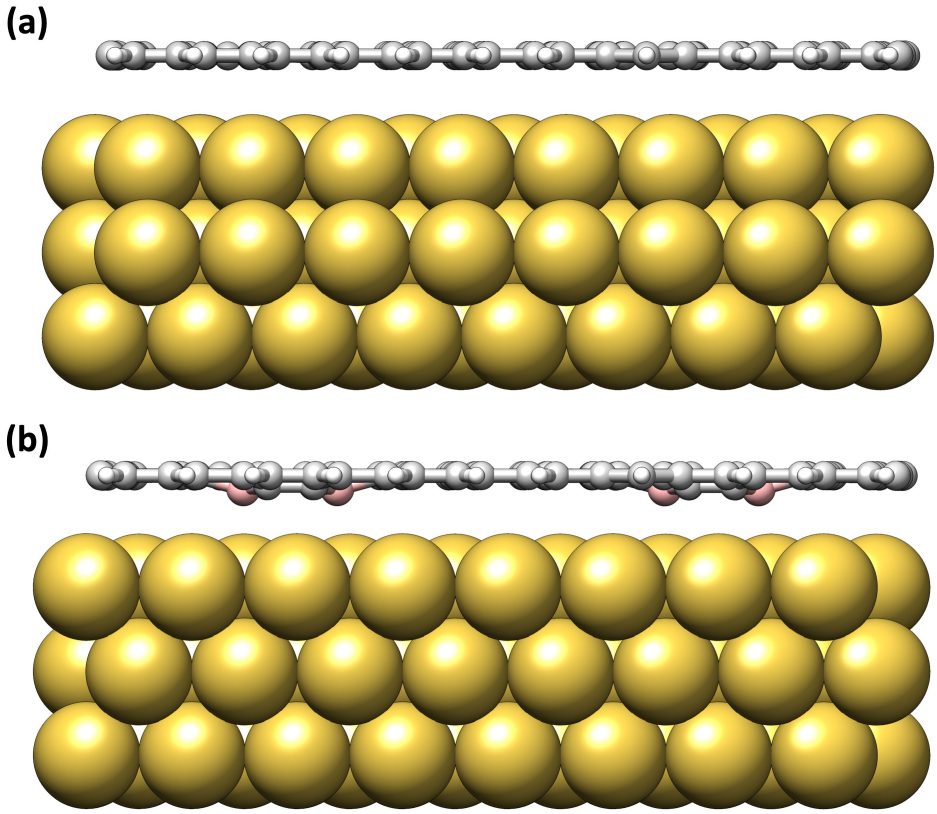


Figure S3: Schematic showing the side view of (a) P-GNR and (b) P-BGNR adsorbed on Au(111).

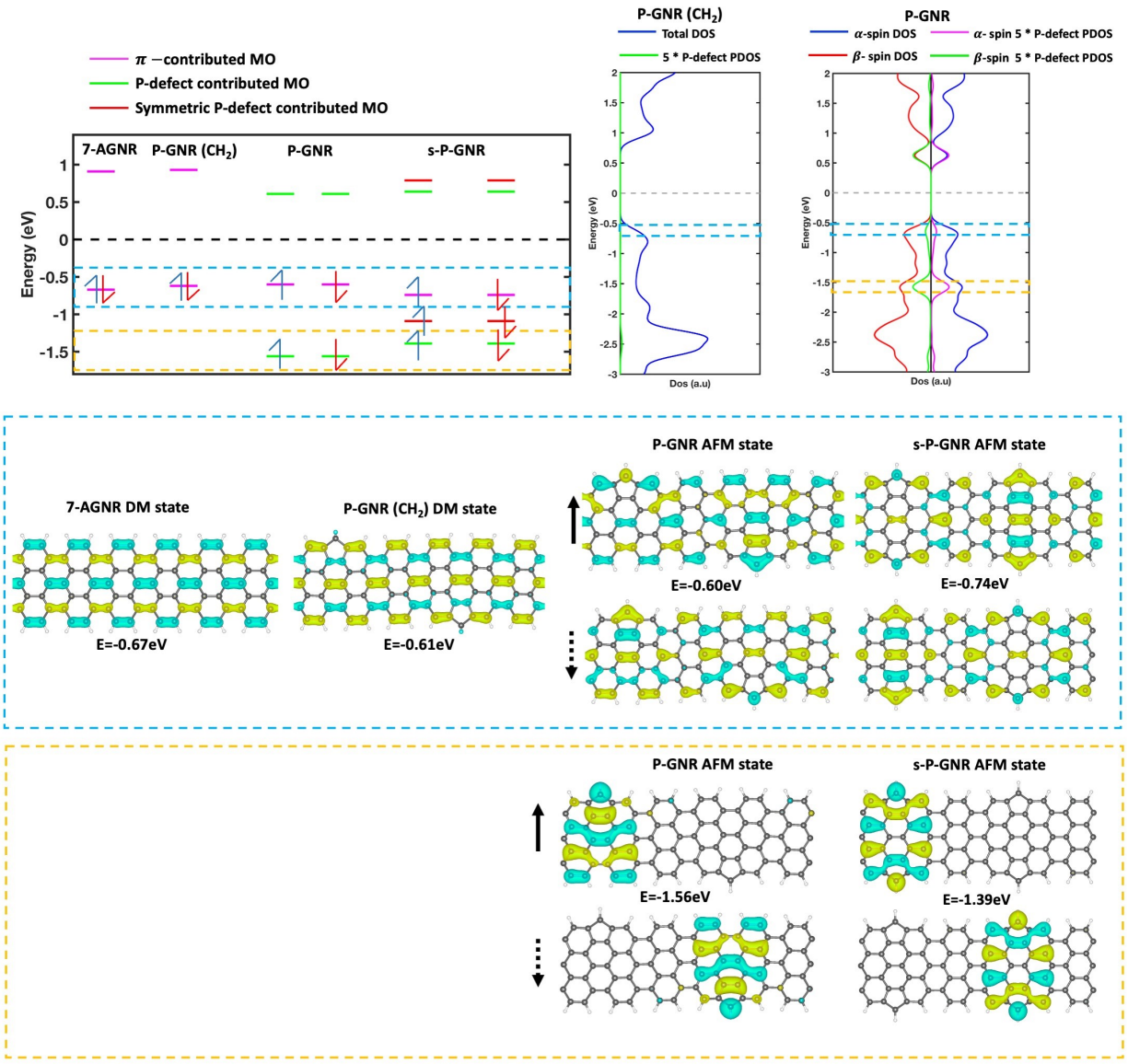


Figure S4: (a)Molecular orbital (MO) level diagram of all-carbon based different GNR species; showing the HOMO (marked by blue rectangle) and LUMO. In addition, low energy localized MO level has been shown for P-GNR and s-P-GNR as indicated by orange rectangle. (b) Different DOS plots for P-GNR($CH_2$) and P-GNR. (c) Spatial distribution of different wavefunctions at different energy levels for respective species as indicated on the figure; isosurfaces are of constant (0.005 $Bohr^{-3/2}$) amplitude. In both (b) and (c), blue and orange rectangle indicates the respective regions as mentioned in (a).

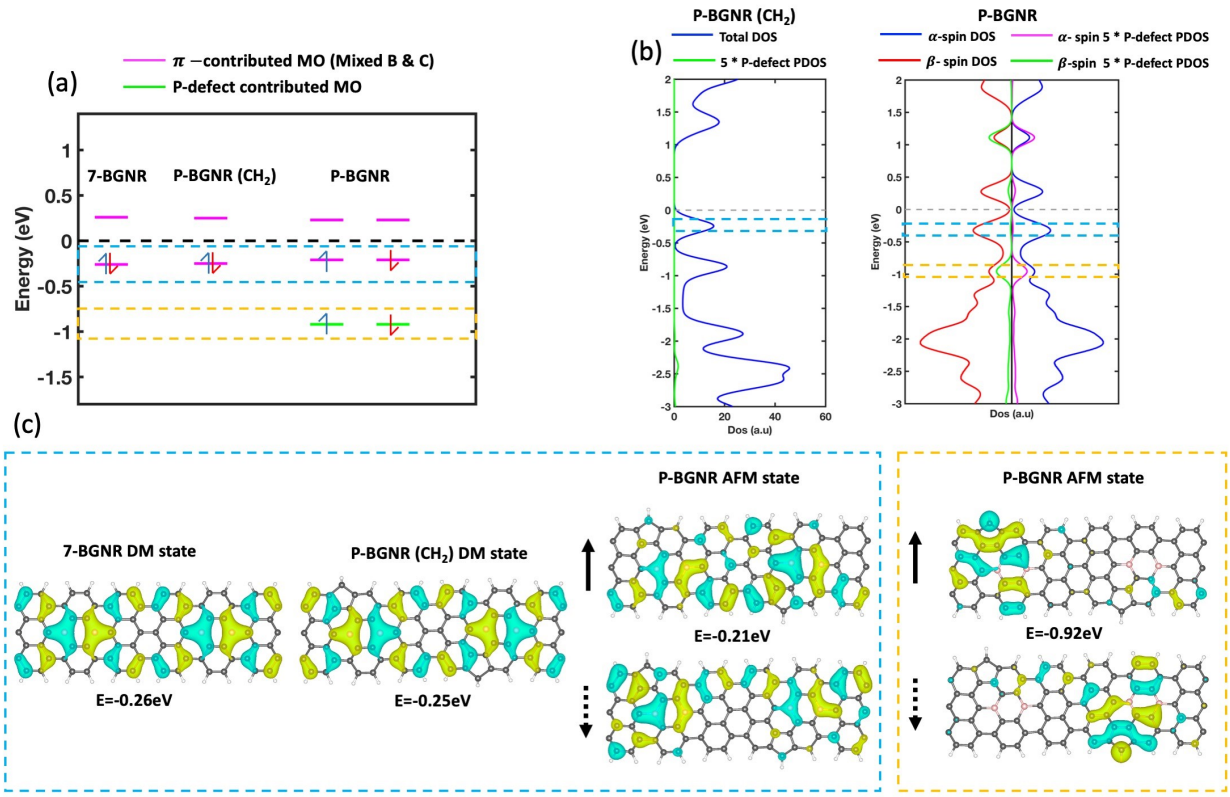


Figure S5: (a)Molecular orbital (MO) level diagram of B-doped different GNR species; showing the HOMO (marked by blue rectangle) and LUMO. In addition, low energy localized MO level has been shown for P-BGNR as indicated by orange rectangle. (b) Different DOS plots for P-BGNR($CH_2$) and P-BGNR. (c) Spatial distribution of different wavefunctions at different energy levels for respective species as indicated on the figure; isosurfaces are of constant (0.005 $Bohr^{-3/2}$) amplitude. In both (b) and (c), blue and orange rectangle indicates the respective regions as mentioned in (a).

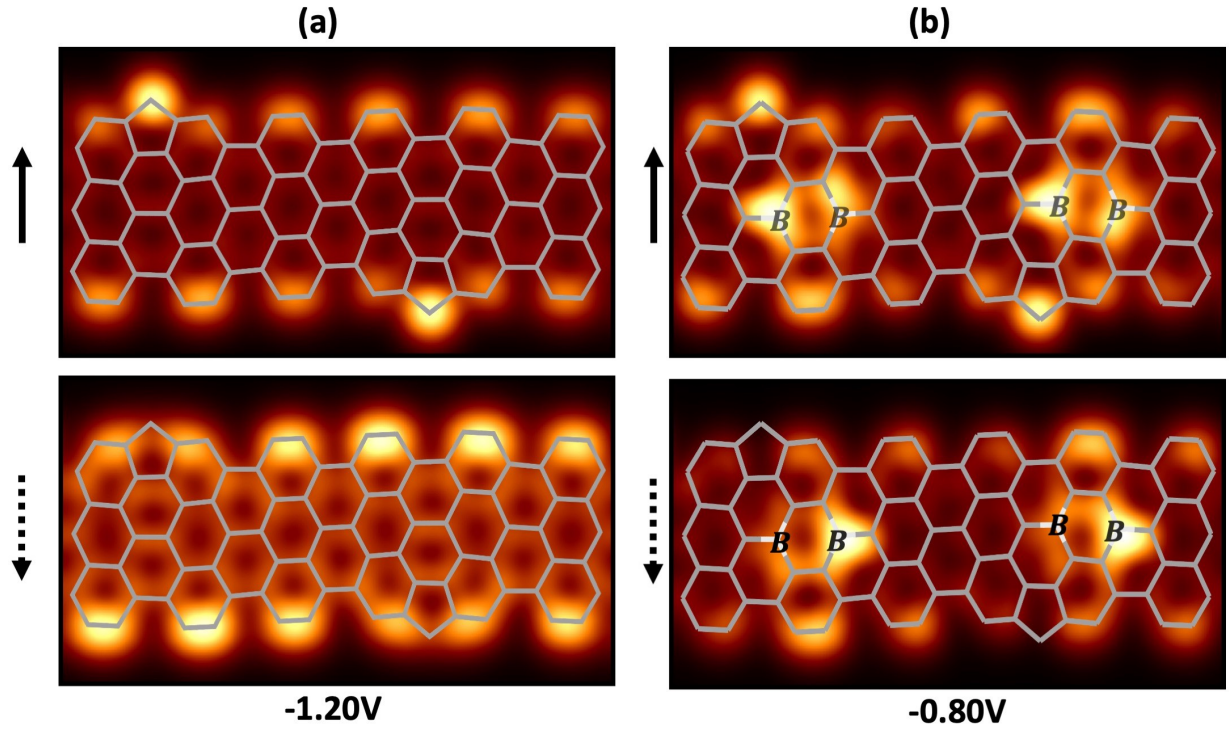


Figure S6: SP-LDOS maps of low energy localized eigenstates for (a) P-GNR and (b) PBGNR.

**Sub-Appendix :**

We have attached below the input file utilized for performing the self-consistent field (SCF) calculation in Quantum Espresso (QE) for AFeM ground state of the P-GNR species.

```
&CONTROL
   calculation = "scf"
   restart_mode='from_scratch'
   prefix='graphene2'
   max_seconds =  4.32000e+04
   pseudo_dir  = "."
   outdir= "."
/

&SYSTEM
   ibrav      = 0
   celldm(1)   =  48.3501868557791
   degauss     =  1.00000e-02
   ecutrho     =  5.000e+02
   ecutwfc     =  5.000e+01
   nat        = 108
   ntyp       = 4
```

```
   occupations = "smearing"
   smearing    = "gaussian"
   nspin       = 2
   starting_magnetization(1) = .2
   starting_magnetization(2) = -.2
   lda_plus_u = .true.,
   lda_plus_u_kind = 0,
   U_projection_type = 'ortho-atomic',
   Hubbard_U(1) = 4.0267
   Hubbard_U(2) = 4.0267
   Hubbard_U(3) = 2.4000
/

&ELECTRONS
   conv_thr        =  1.00000e-10
   electron_maxstep = 200
   mixing_mode      = 'plain'
   mixing_beta      =  3.00000e-01
/

K_POINTS {automatic}
 24 1 1  0 0 0

ATOMIC_SPECIES
C1      12.01070  C.UPF
C2      12.01070  C.UPF
C       12.01070  C.UPF
H        1.00794  H.UPF

CELL_PARAMETERS alat
  1.000000000000000   0.000000000000000   0.000000000000000
  0.000000000000000   1.250692912111611   0.000000000000000
  0.000000000000000   0.000000000000000   0.820767223573244

ATOMIC_POSITIONS (angstrom)
 C1    4.264305   11.289909    5.000000
 C2   17.057220    2.646464    5.000000
 C     4.971260    6.714259    5.000000
 C    17.764172    7.222149    5.000000
 C     0.859318    9.359470    5.000000
 C     1.679811   10.535680    5.000000
 C     3.087070   10.444125    5.000000
 C     3.576508    9.107229    5.000000
 C     2.848568    7.943062    5.000000
 C     1.441965    8.046088    5.000000
 C     3.557350    6.714259    5.000000
 C     2.825853    5.502647    5.000000
```

| | | | |
|---|---|---|---|
| C | 1.391194 | 5.570942 | 5.000000 |
| C | 0.700353 | 6.841341 | 5.000000 |
| C | 3.534815 | 4.268324 | 5.000000 |
| C | 2.746972 | 3.091694 | 5.000000 |
| C | 1.368206 | 3.144632 | 5.000000 |
| C | 0.646465 | 4.368778 | 5.000000 |
| C | 4.952102 | 9.107229 | 5.000000 |
| C | 5.680042 | 7.943062 | 5.000000 |
| C | 5.702757 | 5.502647 | 5.000000 |
| C | 4.993795 | 4.268324 | 5.000000 |
| C | 5.441540 | 10.444125 | 5.000000 |
| C | 6.848798 | 10.535680 | 5.000000 |
| C | 7.669292 | 9.359470 | 5.000000 |
| C | 7.086646 | 8.046088 | 5.000000 |
| C | 7.137416 | 5.570942 | 5.000000 |
| C | 7.882145 | 4.368778 | 5.000000 |
| C | 7.160405 | 3.144632 | 5.000000 |
| C | 5.781639 | 3.091694 | 5.000000 |
| C | 9.119873 | 9.402156 | 5.000000 |
| C | 9.884844 | 8.187937 | 5.000000 |
| C | 9.245680 | 6.904027 | 5.000000 |
| C | 10.003737 | 5.690555 | 5.000000 |
| C | 9.330145 | 4.431331 | 5.000000 |
| C | 9.827171 | 10.622756 | 5.000000 |
| C | 11.201760 | 10.673650 | 5.000000 |
| C | 11.991401 | 9.505117 | 5.000000 |
| C | 11.317788 | 8.245880 | 5.000000 |
| C | 12.075830 | 7.032409 | 5.000000 |
| C | 11.436681 | 5.748489 | 5.000000 |
| C | 12.201626 | 4.534277 | 5.000000 |
| C | 11.494356 | 3.313666 | 5.000000 |
| C | 10.119706 | 3.262784 | 5.000000 |
| C | 7.828256 | 6.841341 | 5.000000 |
| C | 13.439419 | 9.567657 | 5.000000 |
| C | 14.184099 | 8.365486 | 5.000000 |
| C | 13.493271 | 7.095068 | 5.000000 |
| C | 14.234886 | 5.890337 | 5.000000 |
| C | 13.652235 | 4.576938 | 5.000000 |
| C | 14.161176 | 10.791797 | 5.000000 |
| C | 15.539958 | 10.844722 | 5.000000 |
| C | 16.327741 | 9.668072 | 5.000000 |
| C | 15.618785 | 8.433754 | 5.000000 |
| C | 16.350269 | 7.222149 | 5.000000 |
| C | 15.641499 | 5.993333 | 5.000000 |
| C | 16.369413 | 4.829170 | 5.000000 |
| C | 15.879964 | 3.492263 | 5.000000 |
| C | 14.472710 | 3.400726 | 5.000000 |

| | | | |
|---|---|---|---|
| C | 17.786698 | 9.668072 | 5.000000 |
| C | 18.495654 | 8.433754 | 5.000000 |
| C | 18.472942 | 5.993333 | 5.000000 |
| C | 17.745028 | 4.829170 | 5.000000 |
| C | 18.574482 | 10.844722 | 5.000000 |
| C | 19.953263 | 10.791797 | 5.000000 |
| C | 20.675022 | 9.567657 | 5.000000 |
| C | 19.930342 | 8.365486 | 5.000000 |
| C | 19.879555 | 5.890337 | 5.000000 |
| C | 20.462205 | 4.576938 | 5.000000 |
| C | 19.641731 | 3.400726 | 5.000000 |
| C | 18.234477 | 3.492263 | 5.000000 |
| C | 22.123040 | 9.505117 | 5.000000 |
| C | 22.796651 | 8.245880 | 5.000000 |
| C | 22.038611 | 7.032409 | 5.000000 |
| C | 22.677760 | 5.748489 | 5.000000 |
| C | 21.912815 | 4.534277 | 5.000000 |
| C | 22.912681 | 10.673650 | 5.000000 |
| C | 24.287268 | 10.622756 | 5.000000 |
| C | 24.994568 | 9.402156 | 5.000000 |
| C | 24.229597 | 8.187937 | 5.000000 |
| C | 24.868760 | 6.904027 | 5.000000 |
| C | 24.110703 | 5.690555 | 5.000000 |
| C | 24.784296 | 4.431331 | 5.000000 |
| C | 23.994735 | 3.262784 | 5.000000 |
| C | 22.620085 | 3.313666 | 5.000000 |
| C | 20.621168 | 7.095068 | 5.000000 |
| H | 4.264305 | 12.377216 | 5.000000 |
| H | 1.196394 | 11.511736 | 5.000000 |
| H | 0.826383 | 2.201117 | 5.000000 |
| H | 3.226115 | 2.113553 | 5.000000 |
| H | 5.302495 | 2.113553 | 5.000000 |
| H | 7.702227 | 2.201117 | 5.000000 |
| H | 9.642074 | 2.285505 | 5.000000 |
| H | 12.043286 | 2.374380 | 5.000000 |
| H | 13.989284 | 2.424666 | 5.000000 |
| H | 17.057220 | 1.559167 | 5.000000 |
| H | 20.125156 | 2.424666 | 5.000000 |
| H | 22.071155 | 2.374380 | 5.000000 |
| H | 7.332216 | 11.511736 | 5.000000 |
| H | 9.278182 | 11.562046 | 5.000000 |
| H | 11.679410 | 11.650949 | 5.000000 |
| H | 13.619359 | 11.735310 | 5.000000 |
| H | 16.019100 | 11.822852 | 5.000000 |
| H | 18.095339 | 11.822852 | 5.000000 |
| H | 20.495080 | 11.735310 | 5.000000 |
| H | 22.435029 | 11.650949 | 5.000000 |

H 24.836259 11.562046 5.000000
H 24.472366 2.285505 5.000000

**References:**

(1) Rizzo, D. J.; Veber, G.; Jiang, J.; McCurdy, R.; Cao, T.; Bronner, C.; Chen, T.; Louie, S. G.; Fischer, F. R.; Crommie, M. F. Inducing metallicity in graphene nanoribbons via zero-mode superlattices. *Science* **2020**, *369*, 1597–1603, Publisher: American Association for the Advancement of Science.

(2) Carbonell-Sanrom`a, E.; Garcia-Lekue, A.; Corso, M.; Vasseur, G.; Brandimarte, P.; Lobo-Checa, J.; de Oteyza, D. G.; Li, J.; Kawai, S.; Saito, S. et al. Electronic Properties of Substitutionally Boron-Doped Graphene Nanoribbons on a Au(111) Surface.

*The Journal of Physical Chemistry C* **2018**, *122*, 16092–16099, Publisher: American Chemical Society.

(3) Zdetsis, A. D. Bandgaps of atomically precise graphene nanoribbons and Occam's razor.

*Physical Chemistry Chemical Physics* **2022**, *24*, 10334–10345, Publisher: The Royal Society of Chemistry.

(4) Wang, S.; Talirz, L.; Pignedoli, C. A.; Feng, X.; Mu¨llen, K.; Fasel, R.; Ruffieux, P. Giant edge state splitting at atomically precise graphene zigzag edges. *Nature Communications*

**2016**, *7*, 11507, Number: 1 Publisher: Nature Publishing Group.

# APPENDIX B Supplementary Information of Chapter 5- CONTROLLING THE MAGNETIC PROPERTIES OF TWO-DIMENSIONAL CARBON-BASED KAGOME POLYMERS

**Methodology:**

Projector-augmented plane wave (PAW) [1] method was implemented to consider the ion-electron interaction within the Quantum ESPRESSO package [2, 3]. The unit-cell of the polymers with direct C-C linkers contains 62 atoms in total (including the hydrogenated dangling bonds), while the diacetylenic linker based polymers contain 74 atoms per unit-cell. Geometrical optimization was carried out for all structures until energy and force convergence threshold reached $10^{-6}$ Ry and $10^{-4}$ Ry/˚A , respectively, with a $k$-point mesh of 4×4×1. A vacuum of 20Å was introduced along the $z$-direction to minimize interactions between periodic images along that direction. All spin-polarized calculations consider the spin-alignment along $z$-direction for simplicity. In addition, a $K$-point grid of 9×9×1 was used for band structure and properties calculations where energy cut-off value of 50 Ry was employed. For PBE0 calculations, we have taken default 25% Hartree–Fock exchange parameter ($\alpha$=0.25 in $\alpha$-PBE approach) for both Tr and Tr3B polymers. For DFT+U calculations, $U$ value was calculated for all symmetric carbon sites in the unit-cell using the default codes included with Quantum ESPRESSO package [4].

**Further justifications in choosing DFT+U approach:**

To check the accuracy of the methods, we at first calculated the spinexchange parameter, $J$, for both Tr and Tr3B polymers using all three methods tabulated in Table SI. We have observed a considerable amount of changes in $J$ value between simple PBE and other two approaches (PBE0 and DFT+U), although the PBE0 and DFT+U methods lead to a same ground state along with similar closest excited state. The notable changes are specially in the band gap values. In simple PBE calculations, we have observed that bands delocalization around Fermi level is generally overestimated due to a lack of contribution from exact (Hartree-Fock) exchange energy ($\alpha$-PBE functional). Due to the underestimation or the lack of self-interaction corrections among electrons in the occupied states with PBE functional, we have noticed that the diamagnetic (DM), AFeM and FeM phases are very close in energy to each other. Following a similar approach than Thomas *et al.* [5], we have used PBE0 hybrid-functional for pure and doped-polymers with a 25% Hartree–

Fock exchange parameter. This PBE0 approach gives a very stable AFeM ground state for Tr polymer, as observed previously on related systems [6, 7]. In addition, we found FeM ground state for doped-polymers along this PBE0 approach. However, $\alpha$-PBE approach may overestimate self-interaction energy in unoccupied states, and finally shifts the unoccupied bands upwards and leads to an overestimated band gap value [8]. Suitable Hartree–Fock exchange parameters along with optimized effective potentials [9] are required to compare different systems; however, this can modify the other properties and obstructs the comparison. Then, to minimize such trade-off between band gap underestimation with simple DFT and overestimation with hybrid-functional, we used DFT+U method. In brief, simple PBE underestimated the band gaps, while PBE0 and DFT+U approaches show almost similar band gaps. Although the small difference in band gaps between the PBE0 and DFT+U approach might originate from the overestimation of the band gaps in PBE0 approach. In addition, we observe a significant difference between the $J$ value when we concentrate on Tr3B polymer, where the total spin is 1 per unit-cell, unlike Tr polymer which possess a total spin of 2. Simple PBE predicts a AFeM ground state with very close DM phase as the excited state. On the other hand, PBE0 and DFT+U predicts a stable FeM ground state, with AFeM as the closest excited state. Moreover, we observed a metallic nature of dispersion in the $\beta$-spin of Tr3B in PBE approach, while a small band gap opens up in PBE0 and DFT+U approach. This is because of the over delocalized occupied states in simple PBE approach. Although the band gap values between the PBE0 and DFT+U are closer, we believe PBE0 overestimates the band gap by a bit due to the well-delocalization in unoccupied states at the presence of electron-electron interactions through the Hartree–Fock exchange parameter. Although this can be minimized using proper potential and exchange parameter value for different systems, these would lead to an over complicated comparison between these systems. Therefore, we have chosen DFT+U approach for its simplicity and consistency throughout all the studied polymers. For comparison with DFT+U approach, we have also calculated the total $U$ and $J$ value for triarylmethyl radical (TAM) based polymers with the diacetylenic linker as previously studied by Thomas *et al.* [5]. We found $U$=1.36 eV and $J$=-0.20 eV as compared to $U$=1.42 eV and $J$=-0.12 eV, respectively, obtained by Thomas *et al.* with a PBE0 approach. Such good agreement also support the accuracy of our DFT+U approach.

Table SI: Electronic properties of sveral polymers calculated using different DFT approaches. Due to the degenerate nature of the AFeM bands, both spin gives similar band gap values.

| Polymer | J(=$E_{AFeM}$-$E_{FeM}$) (eV) | | | Ground state | | | Ground state bandgap (eV) | | | | | | Closest excited state | | |
|---|---|---|---|---|---|---|---|---|---|---|---|---|---|---|---|
| | | | | | | | PBE | | PBE0 | | DFT+U | | | | |
| | PBE | PBE0 | DFT+U | PBE | PBE0 | DFT+U | $\alpha$ | $\beta$ | $\alpha$ | $\beta$ | $\alpha$ | $\beta$ | PBE | PBE0 | DFT+U |
| Tr | -0.14 | -0.39 | -0.41 | AFeM | AFeM | AFeM | 0.69 | 0.69 | 2.24 | 2.24 | 2.13 | 2.13 | FeM | FeM | FeM |
| Tr3B | -0.05 | 0.08 | 0.10 | AFeM | FeM | FeM | ≈0.00 | ≈0.00 | 0.96 | 0.23 | 0.61 | 0.14 | DM | AFeM | AFeM |

**Triangulene dimer:**

We have found AFeM ground state in triangulene dimer employing our DFT+U approach as illustrated in Fig. S1. In addition, the dimer shows quintet FeM state with spin $S = 2$. Thus, we computed spin-exchange parameter $J$ such that $J = \Delta E/3$ where $\Delta E = E_{AFeM} - E_{FeM\ (quintet)}$ [6].

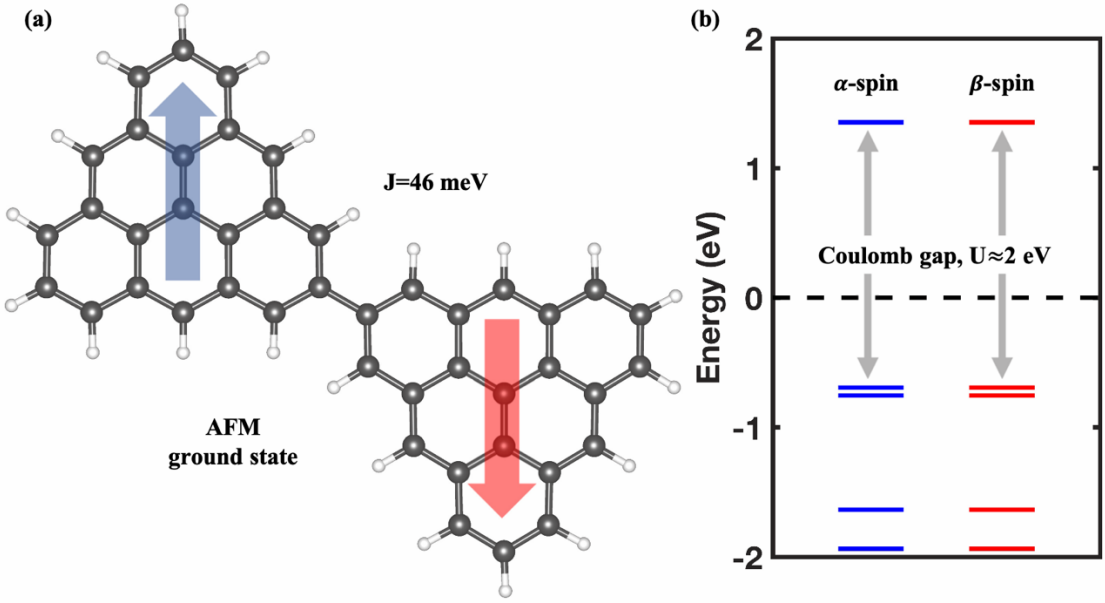


Figure S1: (a) Triangulene dimers with its AFeM ground state: the spin configuration is highlighted by the blue and red arrows. (b) Spin-polarized energy spectra of the AFeM ground states: spin degeneracy is observed between both $\alpha$ and $\beta$ spins. Coulomb gap or estimated $U$ value has been indicated on the figure along with the spin-exchange parameter $J$.

**Charge density plots:**

All charge density plots have been observed at the Γ-point of the Brillouin zone (BZ) where for most of the near Fermi bands have a two-fold degeneracy (see the main manuscript), although that might get lifted at the *M*- and *K*point of the BZ. As illustrated in Fig. S3(a), the semi-metallic Dirac bands of the DM phase of all-C Tr polymer are well-delocalized through the edges of the monomeric units, except the direct C-C linkers and central C atoms.

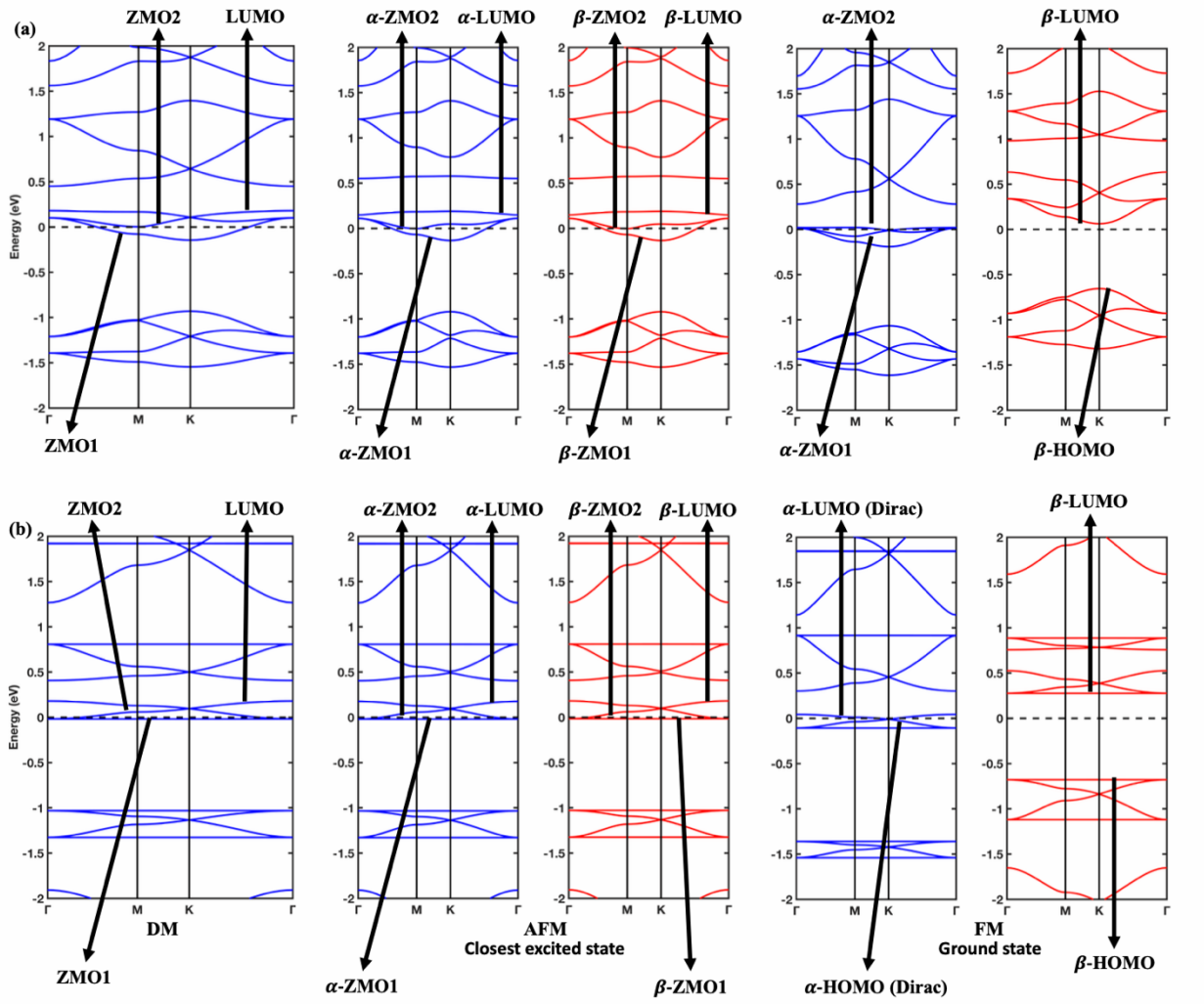


Figure S2: Corresponding definitions of orbitals for (a) Tr3N and (b) Tr3N-CC polymers shown in this figure for reference. Except HOMO-LUMO, we have also identified zero mode orbital (ZMO) corresponding to the bands that pass through the Fermi level. In addition, 'HOMO-LUMO (Dirac)' has been identified for the corresponding bands that show Dirac like feature at the *K*-point of Brillouin zone.

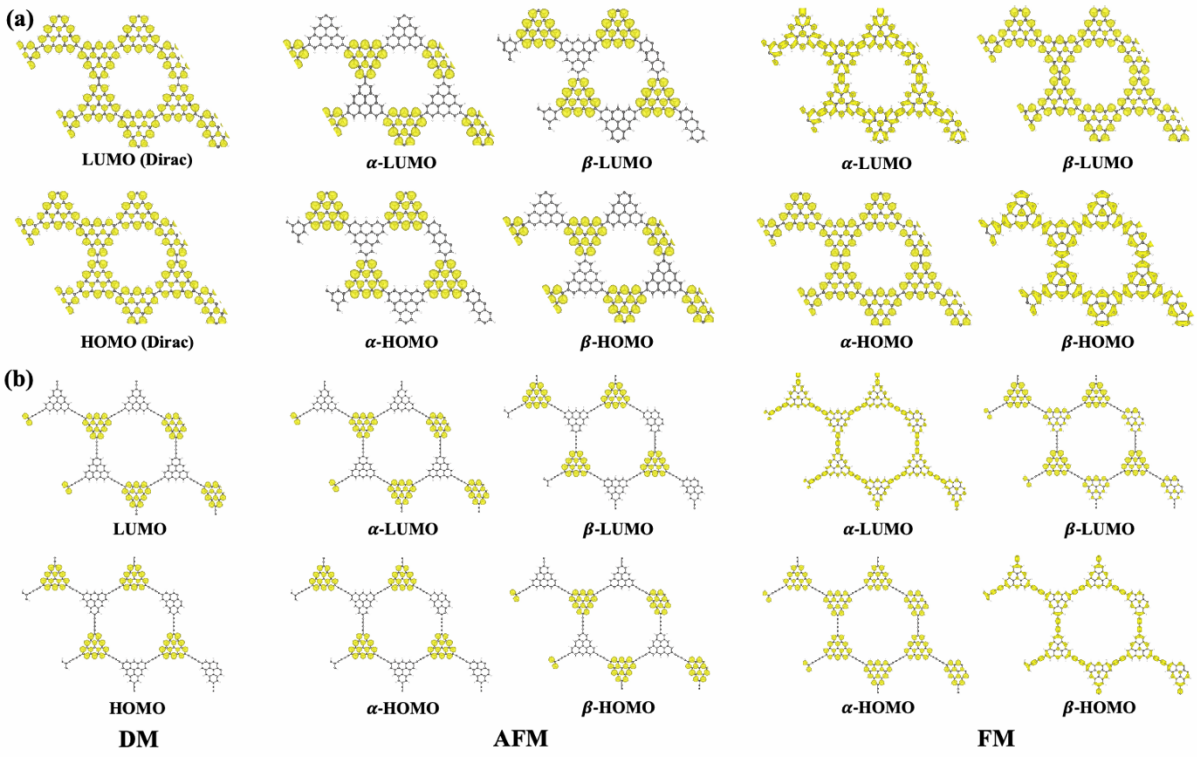


Figure S3: Charge density distribution of the orbitals around the Fermi level for all DM, AFeM and FeM phases of (a) Tr and (b) Tr-CC polymers.

In addition, the ground state Mott-insulating AFeM phase has very localized charge distribution in either nearest neighbor monomer for opposite spins, where the monomer acts as the superatom in this Kagome configuration with $D_{3h}$ symmetry. If we look closely, we can see that charges are localized in different monomers for the same orbital (either HOMO or LUMO) of different spins. We can also predict that the spin density is distributed around the edges of the monomer instead of the central part. On the other hand, we observe a well-delocalized charge distribution from the Dirac bands of FeM phase for LUMO and HOMO of $\alpha$ and $\beta$ spin, respectively. Additionally, for the opposite orbitals, charge is delocalized around the edges throughout the polymer, but not on the central carbon site. Therefore, topological edge states might be observed in the FeM phase for both spins, which are related to the flat bands near the Fermi level that have nondegenerate feature at the *M*- and *K*-point of the BZ, as observed before in one of our previous study [10]. After that, we plotted the charge density for Tr-CC polymer as illustrated in Fig. S3(b). As discussed previously, owing to the loss of exchange coupling between the unpaired electrons, they are strongly localized in nearest neighbor monomers where HOMO and LUMO are just separated by a tiny gap (2.8 meV). The ground state Mott-insulating AFeM phase retains the same charge

density distribution as Tr monomers. In contrast, the FeM phase has strongly localized charge distribution in nearest neighbor monomers for HOMO and LUMO of the $\alpha$ and $\beta$ spins, respectively. The topological edge states might be entirely lost due to the increased distance between the spin clusters, indicating the reduced super-exchange between the spins of nearest neighbors. However, delocalized charge distributions were observed throughout the polymer for the low dispersed Dirac bands of the LUMO and HOMO of the $\alpha$ and $\beta$ spins, respectively.

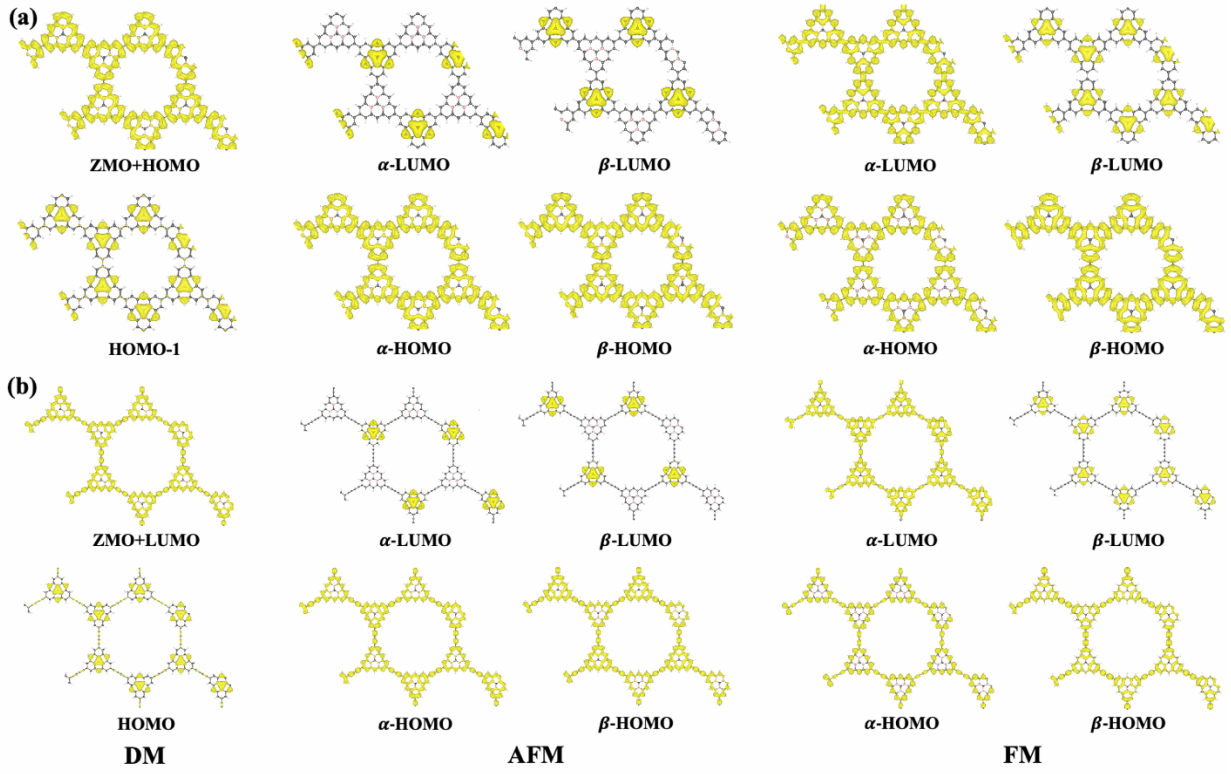


Figure S4: Charge density distribution of the orbitals around the Fermi level for all DM, AFeM and FeM phases of (a) Tr3B and (b) Tr3B-CC polymers.

Owing to the spin-polarized semiconducting nature of the ground state FeM phase of Tr3B and Tr3B-CC polymer, we found some interesting charge density distribution of HOMO, LUMO, and ZMO bands. As illustrated in Fig. S4(a), DM phase has degenerated ZMO and HOMO at the the Γ-point of the BZ and shows delocalized charge distribution throughout the polymer, pointing towards the metallic nature of this DM phase; while the nearly flat HOMO-1 shows localized charge distribution just around the central carbon site. On the other hand, in the AFeM phase, we observed a very localized charge density distribution in either nearest neighbor monomers for the opposite spins for the flat bands in $\alpha$ and $\beta$ LUMO. However, compared to the pure triangulene

based AFeM phase, the charge is well-localized around the central part of the monomer, which suggests the charge distribution between the dopant sites and the central carbon atoms. More specifically, it helps us understand the unpaired electron occupancy around the central carbon atoms of the monomers when doped with B. If we now concentrate on the dispersed bands of $\alpha$ and $\beta$ HOMO of the AFeM phase, a well-delocalized charge distribution can be observed. In addition, the ground state FeM phase has very well charge delocalization in its $\alpha$ spin HOMO and LUMO, which suggest its good transport properties, while the $\beta$ spin has some strange charge distribution. If we look closely at $\beta$ LUMO, we can find a localized charge distribution around the central carbon atoms in all monomers throughout the system, unlike the AFeM phase, where the charge was localized in just either of the nearest neighbor monomers. Nonetheless, $\beta$ HOMO retains a well-delocalized charge distribution throughout the system. Furthermore, for Tr3B-CC polymer (see Fig. S4(b)), the DM phase has a very flat LUMO band with a Dirac-like ZMO band that degenerates at the $\Gamma$ point of the BZ. Charge distribution has been observed around the edges for this degenerated ZMO and LUMO, which suggest the topological nature of those bands because of the lifted degeneracy at the $M$- and $K$-point of the BZ. For the AFeM phase, $\alpha$ and $\beta$ LUMO has similar charge distribution along the monomers as Tr3B polymer, while the HOMOs of different spins resembles the Tr3B like charge distribution along the monomers in addition to some well distributed charge through the diacetylenic linker. Contrarily, the ground state FeM phase shows similar charge distribution as Tr3B FeM phase for all spins except the charge distribution along the diacetylenic linker. Additionally, topological edge distribution for $\alpha$ HOMO and LUMO can be observed for the non-degenerate near Fermi flat bands at the $M$- and $K$-point of the BZ, which is also true for $\beta$ HOMO.

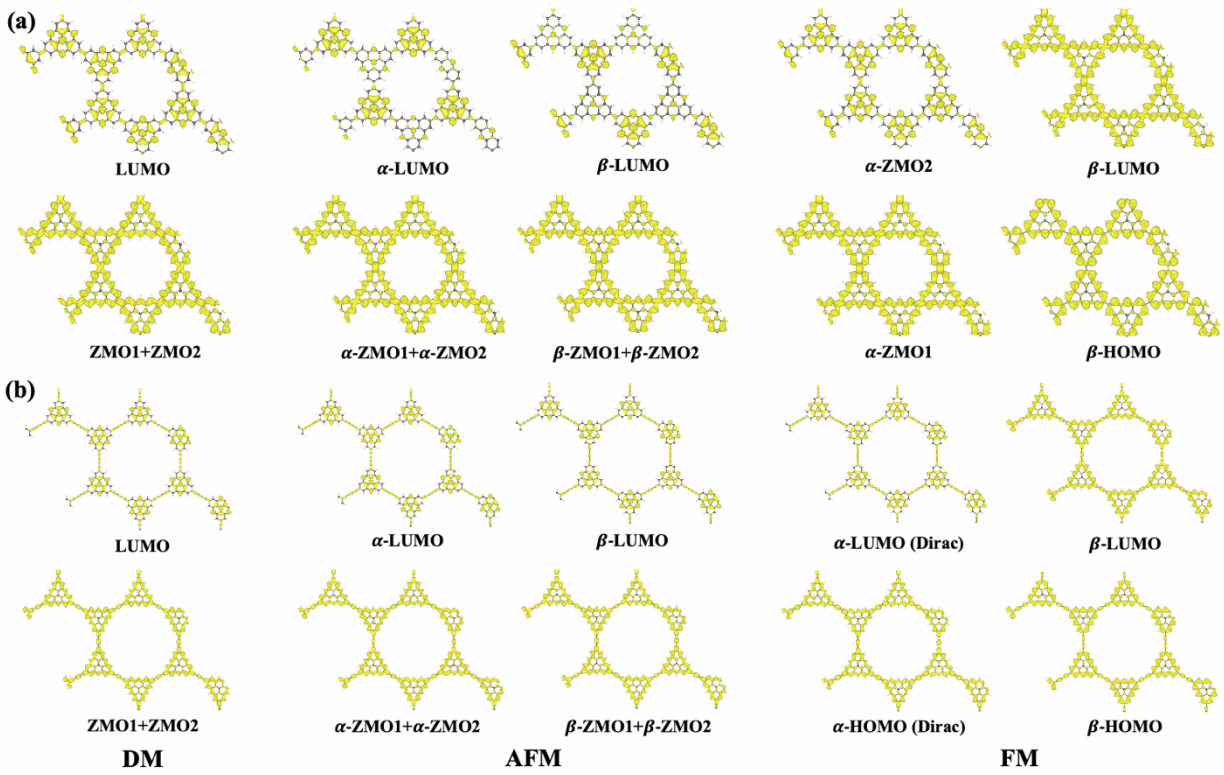


Figure S5: Charge density distribution of the orbitals around the Fermi level for all DM, AFeM and FeM phases of (a) Tr3N and (b) Tr3N-CC polymers.

Owing to the metallic nature of the DM phase and AFeM phase orbitals, the LUMOs and ZMOs are well delocalized throughout the Tr3N polymer (see Fig. S5(a)). This is also true for both spins of the ground state FeM phase owing to the n-type doping of the system, although $\alpha$ spin has the metallic feature, while $\beta$ spin has an n-type semiconducting band gap. However, if we look at the $\alpha$-ZMO2 charge distribution, which is located just above the Fermi level at the Γ-point of the BZ, we can observe a weakly localized charge distribution around the central atom instead of the edges as for other cases. This justifies the weak magnetization in this T3NH polymer that comes from the unpaired holes. For Tr3N-CC polymer, charge distribution follows the similar charge distribution along the monomers as Tr3N and same topological feature might be observed for the near Fermi flat bands as discussed previously for Tr3B. Although all the phases have topological edge distribution, depending on the spins and orbitals, the direction of the topological edge states can vary. The corresponding orbitals have been indicated on each plots of Fig. S3-S5. Isosurface has been set to 0.0005 e/Å$^3$ for the illustration.

**References:**


[1] P. E. Blöchl, Projector augmented-wave method, Physical Review B 50 (24) (1994) 17953–17979. doi:10.1103/PhysRevB.50.17953.

[2] P. Giannozzi, S. Baroni, N. Bonini, M. Calandra, R. Car, C. Cavazzoni, D. Ceresoli, G. L. Chiarotti, M. Cococcioni, I. Dabo, A. D. Corso, S. d. Gironcoli, S. Fabris, G. Fratesi, R. Gebauer, U. Gerstmann, C. Gougoussis, A. Kokalj, M. Lazzeri, L. Martin-Samos, N. Marzari, F. Mauri, R. Mazzarello, S. Paolini, A. Pasquarello, L. Paulatto, C. Sbraccia, S. Scandolo, G. Sclauzero, A. P. Seitsonen, A. Smogunov, P. Umari, R. M. Wentzcovitch, QUANTUM ESPRESSO: a modular and open-source software project for quantum simulations of materials, Journal of Physics: Condensed Matter 21 (39) (2009) 395502. doi:10.1088/0953-8984/21/39/395502.

[3] P. Giannozzi, O. Andreussi, T. Brumme, O. Bunau, M. B. Nardelli, M. Calandra, R. Car, C. Cavazzoni, D. Ceresoli, M. Cococcioni, N. Colonna, I. Carnimeo, A. D. Corso, S. d. Gironcoli, P. Delugas, R. A. DiStasio, A. Ferretti, A. Floris, G. Fratesi, G. Fugallo, R. Gebauer, U. Gerstmann, F. Giustino, T. Gorni, J. Jia, M. Kawamura, H.-Y. Ko, A. Kokalj, E. Kücükbenli, M. Lazzeri, M. Marsili, N. Marzari, F. Mauri, N. L. Nguyen, H.-V. Nguyen, A. Otero-de-la Roza, L. Paulatto, S. Poncé, D. Rocca, R. Sabatini, B. Santra, M. Schlipf, A. P. Seitsonen, A. Smogunov, I. Timrov, T. Thonhauser, P. Umari, N. Vast, X. Wu, S. Baroni, Advanced capabilities for materials modelling with Quantum ESPRESSO, Journal of Physics: Condensed Matter 29 (46) (2017) 465901. doi:10.1088/1361-648X/aa8f79.

[4] M. Cococcioni, S. de Gironcoli, Linear response approach to the calculation of the effective interaction parameters in the *LDA+U* method, Physical Review B 71 (3) (2005) 035105. doi:10.1103/PhysRevB.71.035105.

[5] S. Thomas, H. Li, J.-L. Bredas, Emergence of an Antiferromagnetic Mott Insulating Phase in Hexagonal $\pi$-Conjugated Covalent Organic Frameworks, Advanced Materials 31 (17) (2019) 1900355. doi:10.1002/adma.201900355.

[6] S. Mishra, D. Beyer, K. Eimre, R. Ortiz, J. Fernández-Rossier, R. Berger, O. Gröning, C. A. Pignedoli, R. Fasel, X. Feng, P. Ruffieux, Collective All-Carbon Magnetism in Triangulene Dimers, Angewandte Chemie International Edition 59 (n/a) (2020) 2–9. doi:10.1002/anie.202002687.

[7] J. Hieulle, S. Castro, N. Friedrich, A. Vegliante, F. R. Lara, S. Sanz, D. Rey, M. Corso, T. Frederiksen, J. I. Pascual, D. Peña, On-Surface Synthesis and Collective Spin Excitations of a Triangulene-Based Nanostar, Angewandte Chemie International Edition 60 (48) (2021) 25224–25229. doi:10.1002/anie.202108301.

[8] J. P. Perdew, Density functional theory and the band gap problem, International Journal of Quantum Chemistry 28 (S19) (1985) 497–523. doi:10.1002/qua.560280846.

[9] T. W. Hollins, S. J. Clark, K. Refson, N. I. Gidopoulos, Optimized effective potential using the Hylleraas variational method, Physical Review B 85 (23) (2012) 235126. doi:10.1103/PhysRevB.85.235126.

[10] K. N. Anindya, A. Rochefort, Collective Magnetism in 2D Polymer Made of C-Doped Triangular Boron Nitride Nanoflakes, Advanced Theory and Simulations 4 (5) (2021) 2100028. doi:10.1002/adts.202100028.

# APPENDIX C Supplementary Information of Chapter 6- COLLECTIVE MAGNETISM IN 2D POLYMER MADE OF C-DOPED TRIANGULAR BORON NITRIDE NANOFLAKES

**Computational details:**

For KL polymers, convergence threshold of $10^{-6}$ eV and $10^{-4}$ eV/Å were considered for energy and force respectively during the relaxation calculations, and a cutoff energy of 480 eV was considered for the plane wave basis set. Calculated lattice constants for the perfect KL polymers are found 18.20 Å (CtBN) and 17.75 Å (CtNB) after lattice optimization, while it is 17.68 Å for the copolymer configuration. The distance between central carbon atoms is approximately 10.3±0.2 Å in doped polymers and copolymers.

**DFT and TDDFT results on dimers:**

The wavefunction contours shown in Figure S1 were produced with the VESTA software[1] from the different dimers considered. The occupied (left) and unoccupied (right) orbitals are separated by the dashed red line, the individual DFT eigenvalues are indicated in red, the orbital numbers are shown in black.

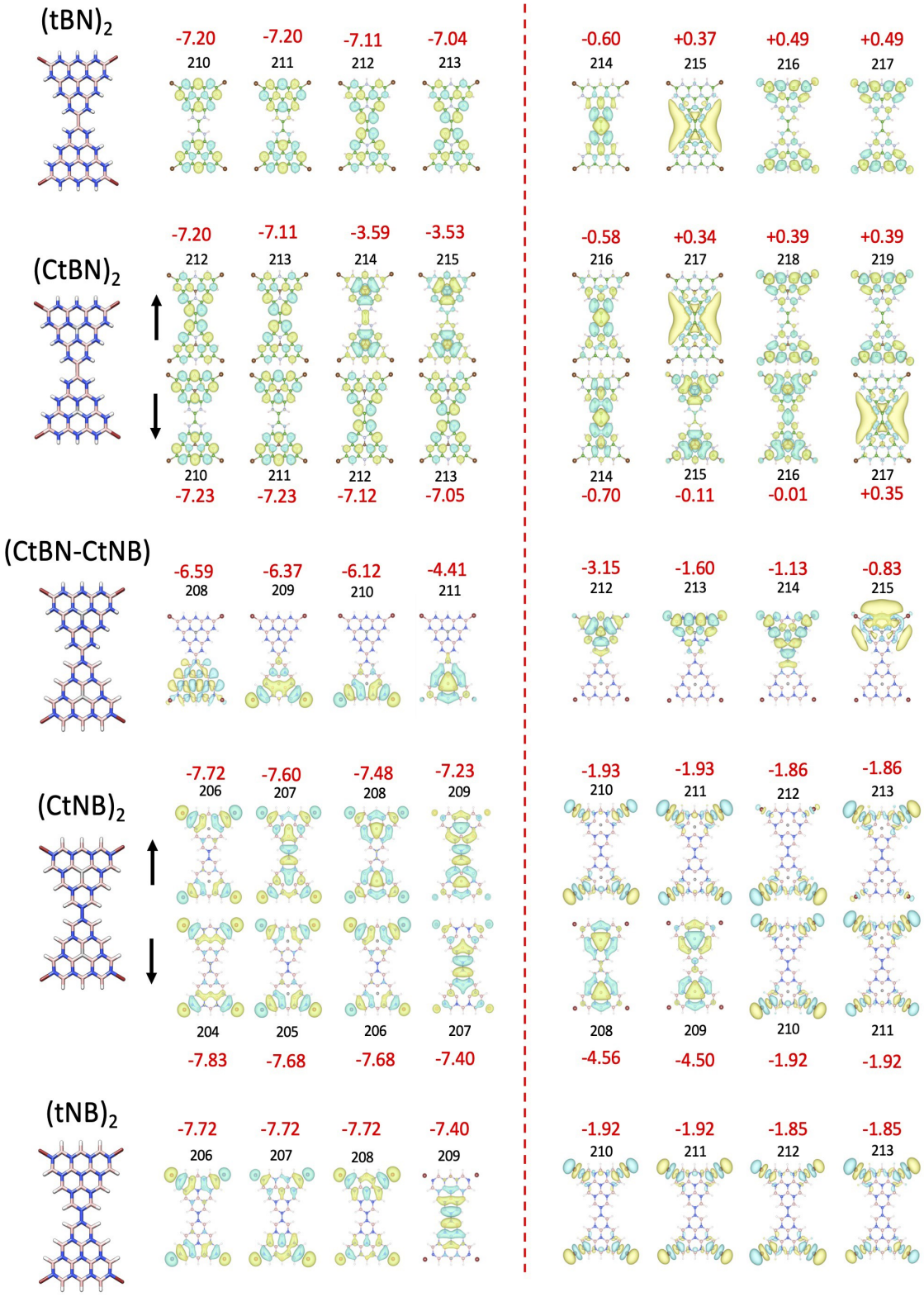


FIG. S1. Graphical representation of molecular orbitals of different dimer configurations in different states (spin directions in triplet state are indicated by black arrows). Isosurface values were set to 0.01 $Å^{-3/2}$.

Table S1 gives detailed results obtained from TDDFT calculations, more especially regarding to the few first vertical electron transitions in the ground state and first excited state. For the first three vertical transitions, we reported the calculated TDDFT energy ($E_{g*}$), their respective origin and intensity (oscillator strength), and the general characteristic of the molecular orbitals around Fermi level of the materials. We defined the copolymer as a flat-band insulator (FBI) because the calculated oscillator strengths for the few first vertical transitions are really small.

**DFT results on polymers and copolymers:**

As illustrated in Fig. S2, the excited states of the C-doped polymers are Dirac semi-metal while a narrow gap flat bands can be observed for both spins in the triplet excited state of the copolymer.

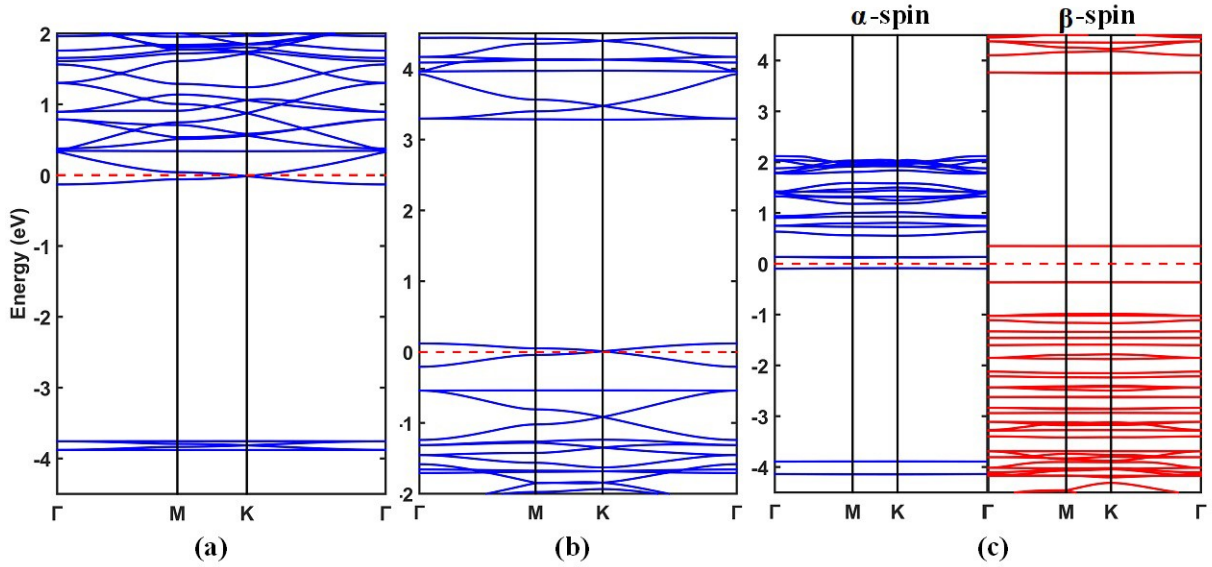


FIG. S2. Band structures of the first excited state of (a) CtBN, (b) CtNB polymer, and (c) (CtBN-CtNB) copolymer. The Fermi level has been shifted to zero and is marked by the red dashed line. Triplet state spins are given at the top of the figure.

Electronic density of states (DOS) is plotted to show the highly localized flat band states. Due to the presence of highly localized states, we had to use a very fine energy grid with an increment of 0.005 eV to reveal all states. In addition, as shown in the projected DOS (PDOS) at Fig. S3, the nature of the Dirac bands can be straightforwardly ascribed to carbon 2p (C2p) orbitals. For the copolymer configuration, P-(CtBN-CtNB), C2p orbital is found to be responsible for the two flat bands in the vicinity of Fermi level.

TABLE S1. Electronic structure properties of the more stable singlet (S) and triplet (T) states of tBN dimers and polymers. The band gap $E_g$ and $E_{gP}$ are obtained from $|\varepsilon_{HOMO}-\varepsilon_{LUMO}|$, while $E_g*$ is the energy of the few first electron transition calculated with TDDFT. The exponent values in the transitions correspond to the combination of states that equally contribute to the CI expansion.

| ***Dimer*** | ***ΔE*** (eV) | ***State*** | $E_g$ [a] (eV) | $E_{gP}$ [b] (eV) | $E_{g*}$ [c] (eV) | ***Transition*** [d] | ***Oscillator strength f*** | ***Material*** [e] ***behaviour*** |
|---|---|---|---|---|---|---|---|---|
| $(tBN)_2$ | 0.00 | S | 6.44 | 4.55 | 5.54 | $HOMO \rightarrow LUMO$ | 0.0000 | Insulator |
| | | | | | 5.63 | $HOMO^{-1} \rightarrow LUMO$ | 0.1206 | |
| | | | | | 5.95 | $HOMO^{-2} \rightarrow LUMO$ | 0.0819 | |
| | 4.45 | T | 3.94 | – | | | | |
| $(CtBN)_2$ | 0.00 | T | 2.95 | 0.25 | 2.16 | $HOMO \rightarrow LUMO$ | 0.1014 | DCS |
| | | | | | 2.22 | $HOMO^{-1} \rightarrow LUMO$ | 0.0001 | |
| | | | | | 2.83 | $HOMO^{-1,0} \rightarrow LUMO^{+2,+3}$ | 0.0288 | |
| | 1.18 | S | 0.64 | – | 0.93 | $HOMO \rightarrow LUMO$ | 0.5904 | DCM |
| | | | | | 1.24 | $HOMO \rightarrow LUMO^{+1}$ | 0.0000 | |
| | | | | | 1.58 | $HOMO \rightarrow LUMO^{+2,+3}$ | 0.0366 | |
| (CtBN-CtNB) | 0.00 | S | 1.26 | 1.48 | 0.90 | $HOMO \rightarrow LUMO$ | 0.0074 | (FBI) |
| | | | | | 2.51 | $HOMO \rightarrow LUMO^{+1}$ | 0.0000 | |
| | | | | | 2.69 | $HOMO \rightarrow LUMO$ | 0.0000 | |
| | 1.36 | T | 1.55 | 0.22 | 1.28 | $HOMO \rightarrow LUMO$ | 0.0000 | (FBI) |
| | | | | | 1.35 | $HOMO \rightarrow LUMO^{+1}$ | 0.0000 | |
| | | | | | 1.92 | $HOMO \rightarrow LUMO^{+3}$ | 0.0002 | |
| $(CtNB)_2$ | 0.00 | T | 2.84 | 0.72 | 2.06 | $HOMO \rightarrow LUMO$ | 0.1026 | DCS |
| | | | | | 2.12 | $HOMO \rightarrow LUMO^{+1}$ | 0.0000 | |
| | | | | | 2.33 | $HOMO \rightarrow LUMO^{0,+1}$ | 0.0396 | |
| | 1.21 | S | 0.54 | – | 0.85 | $HOMO \rightarrow LUMO$ | 0.4477 | DCM |
| | | | | | 0.85 | $HOMO \rightarrow LUMO^{+1}$ | 0.0001 | |
| | | | | | 1.36 | $HOMO \rightarrow LUMO^{+2,+3}$ | 0.0000 | |
| $(tNB)_2$ | 0.00 | S | 5.48 | 3.47 | 4.98 | $HOMO \rightarrow LUMO$ | 0.0000 | Insulator |
| | | | | | 5.16 | $HOMO^{-1} \rightarrow LUMO$ | 0.0000 | |
| | | | | | 5.22 | $HOMO \rightarrow LUMO^{+1}$ | 0.0000 | |
| | 2.41 | T | 4.83 | – | | | | |

[a]DFT gap for dimer ; [b]DFT gap for polymer; [c] TDDFT gap for dimer; [d] the exponent in $LUMO^{+n1,+n2}$ indicates an equal mixture of $LUMO^{+n1}$ and $LUMO^{+n3}$ orbitals; [e] : DCS: Dirac-cone semiconductor; DCM : Dirac-cone semi-metal; FBI : Flat-band insulator.

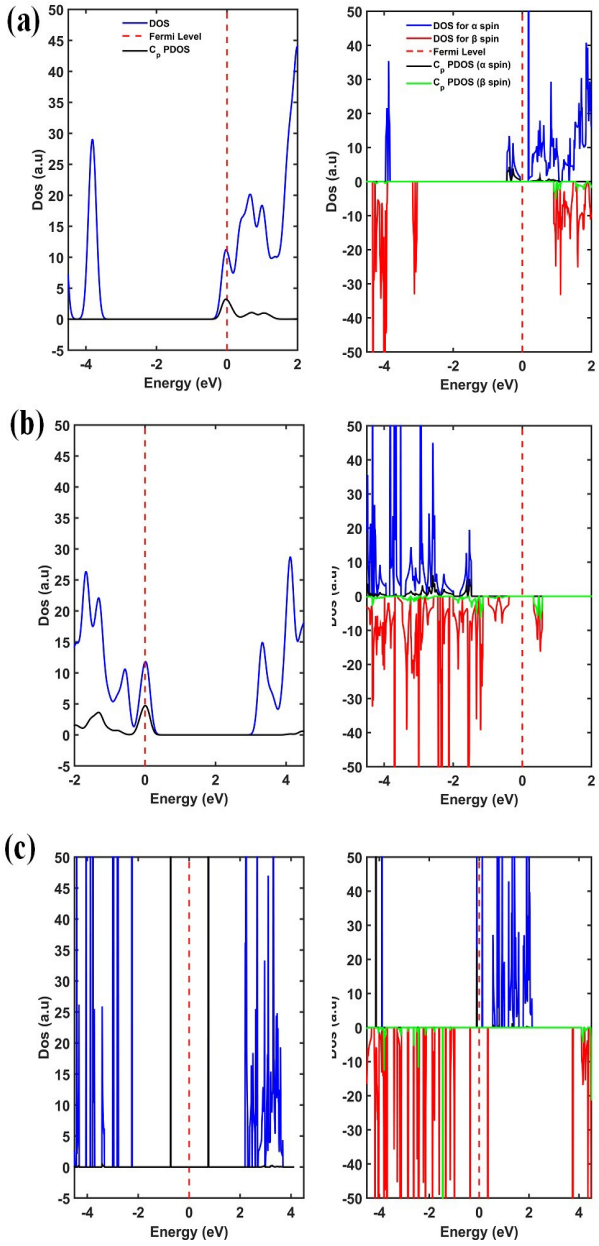


FIG. S3. Density of States (DOS) of singlet (left) and triplet (right) states of (a) CtBN, (b) CtNB polymer, and (c) (CtBN-CtNB) copolymer. The Fermi level has been shifted to zero and is identified by the red dashed line. The origin of the different DOS and PDOS curves is shown in the legend of the two topmost figures.

Magnetic moment for individual doped-site (here only corresponding C atom magnetic moment is reported) are given in Table SII. Although the magnetic moment for individual carbon site is found ~0.20 $\mu_B$ for the perfect doped polymers, the coupling between the two C atoms results in a much higher magnetization than the sum of the components within the unit cell. In contrast, the

magnetization for the copolymer is practically negligible, in agreement with the strong electron localization observed into the charge density plots.

Charge density profiles of the flat bands in $\alpha$-spin ($\beta$-spin) of triplet ground states of CtBN (CtNB) based polymers indicate that there is no coupling between the two central carbon atoms within the unit cell of the respected KLs. The electron charge is distributed independently along the edges of the cells throughout the lattice as observed from Fig. S4.

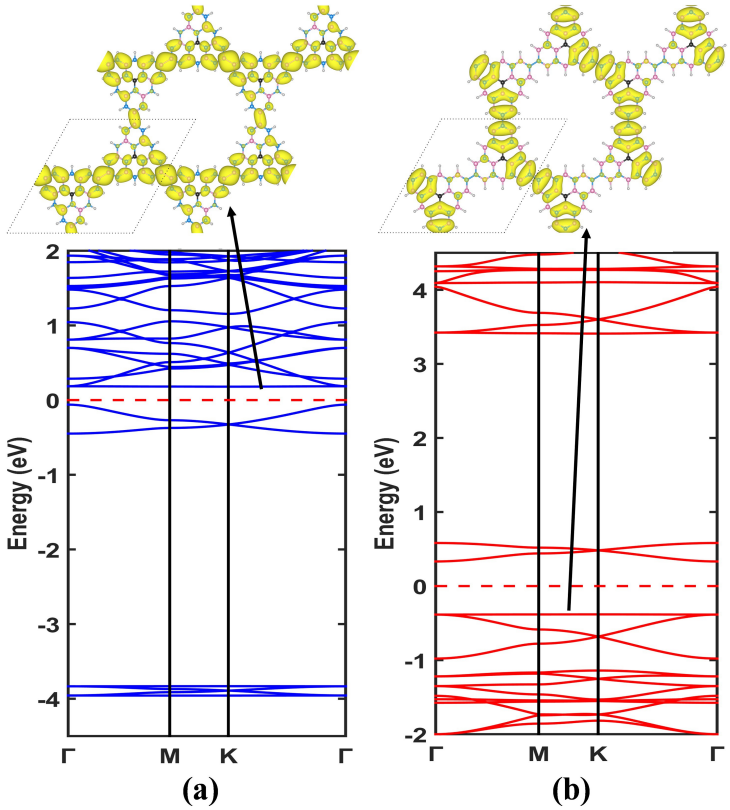


FIG. S4. Graphical representation of charge density distribution of the flat bands in triplet ground states of perfect polymers; (a) CtBN and (b) CtNB configurations. Isosurface has been set to 0.0009 e/Å$^3$ for both figures.

**Carrier mobility:**

Charge carriers in a non-polar crystal is mainly scattered by the acoustic mode phonons and the carrier mobility caused by this interaction can be estimated by deformation potential of the lattice.[2] This procedure has been demonstrated reliable to quantify carrier mobilities of different non-polar crystals.[3,4] The carrier mobilities are described as follow:

$$\mu = \frac{2e\hbar^3\chi}{3k_BT|m*|^2\varsigma^2} \quad (1)$$

where $m^*$ is the effective mass, $\chi$ is the elastic modulus and $\varsigma$ is the deformed potential. $\chi$ can be obtained from $\chi = (\partial E_0/\partial\psi^2)/A$, where $E_0$ is the total energy of the lattice, $\psi$ is the applied uni-axial strain on the lattice and A is the area of the lattice. Deformation potential $\varsigma$ is defined as $\Delta E_B = \varsigma \cdot \partial\psi$, where $\Delta E_B$ is the band edges shift position with respect to the change in applied strain $\psi$.

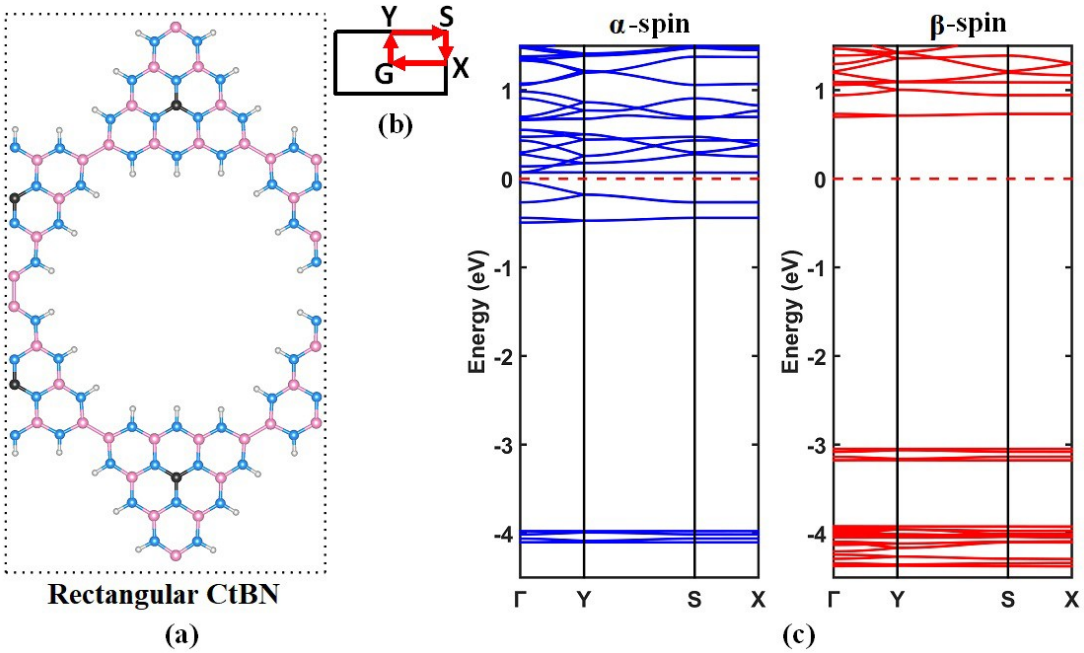


FIG. S5. (a) Rectangular 2D lattice of $P^2$-CtBN used to compute the carrier mobility and its (b) corresponding first Brillouin Zone (BZ) symmetry points. (c) Band structures of rectangular CtBN.

For this mobility calculation, we have considered the 2D rectangular shaped supercell illustrated in Fig. S5(a). In our computations, we considered both tensile and compressive strain on both zigzag and armchair direction of the lattice (uniaxial direction at a time). The band structures of CtBN based rectangular cell matches with its corresponding Kagome unit cell at the Γ-point for both spins in triplet state.

**References:**

[1] K. Momma, F. Izumi, *J. Appl. Crystallogr.* 2011, *44*, 6 1272.

[2] J. Bardeen, W. Shockley, *Phys. Rev.* 1950, *80*, 1 72.

[3] J. Qiao, X. Kong, Z.-X. Hu, F. Yang, W. Ji, *Nat. Commun.* 2014, *5*, 1 4475, number: 1.

[4] Y. Jing, T. Heine, *J. Am. Chem. Soc.* 2019, *141*, 2 743.